

Miniaturized discharges
—
prospects and limits for quantitative analysis

DISSERTATION

zur Erlangung des Doktorgrades der Naturwissenschaften
des Fachbereichs Physik der Universität Dortmund

vorgelegt von
Kerstin Kunze

Dortmund 2004

Referent: Prof. Dr. Kay Niemax

Korreferent: Prof. Dr. Manfred Bayer

Tag der mündlichen Prüfung: 25.06.2004

Abstract

Miniaturized discharges are investigated as a tool for quantitative analysis. In comparison with larger plasma devices commonly used in analytical spectroscopy, different advantages can be achieved: portable instruments allowing to bring the laboratory to the sample instead delivering the sample to the laboratory, lower sample and power consumption, as well as a higher power density. Basic aspects of miniaturization of discharges are discussed and all micro-discharges currently developed as laboratory devices for analytical spectroscopy are enlisted and commented. Two discharges are investigated in detail, namely the dielectric barrier discharge (DBD) and the micro hollow cathode discharge (MHCD). Atomic absorption spectroscopy with diode lasers is used for the determination of plasma parameters, such as spatial distribution of excited species, gas temperature and electron density. For the DBD, plasma diagnostics reveals that the hot region of the plasma is constricted close to the temporary cathode for a short time of each discharge cycle. In this thin layer, the electron density reaches 10^{15} cm^{-3} and the gas temperature is about 1000 K, while the rest of the discharge remains cold. In the case of the MHCD, it is shown that the gas temperature and electron density at atmospheric pressure in Ar are in the range of 1500 K and $5 \cdot 10^{15} \text{ cm}^{-3}$, respectively. Both discharges are applied for analytical measurements, introducing the sample either continuously with gas mixtures or after separation with a gas chromatograph. Emission, absorption and mass spectrometry are used as detection techniques. Limits of detection in the order of few pg/s are obtained for chlorine in halogenated molecules. The analytical figures of merit are comparable or even better than those of conventional discharges and commercial devices. The lifetime of these microplasmas are quiet long and they are characterized by robustness and reproducibility.

Zusammenfassung

Es werden miniaturisierte Entladungen charakterisiert, die in der quantitativen chemischen Analytik eingesetzt werden sollen. Im Vergleich zu bislang eingesetzten größeren Plasmaquellen bieten Mikroplasmen eine Reihe von Vorteilen: tragbare Instrumente erlauben es das Labor zur Probe zu bringen anstatt die Probe in das Labor zu holen, geringere Probenvolumina und Leistungen zu benutzen und höhere Leistungsdichte zu erreichen. Die physikalischen Grundlagen für die Verkleinerung von Plasmaquellen werden dargestellt und es wird ein kurzer Überblick über die bisher in der analytischen Spektroskopie eingesetzten Mikroplasmen gegeben. Zwei miniaturisierte Entladungen werden näher untersucht, die dielektrisch behinderte Entladung (DBD) und die Mikrohohlkathoden-Entladung (MHCD). Es wurden Absorptionsmessungen mit Diodenlaser durchgeführt, um Plasmaparameter, wie räumliche Verteilung angeregter Atome, Gastemperatur und Elektronendichte, zu bestimmen. Für die DBD wird gezeigt, dass die Plasmaentladung auf einen engen Bereich nahe der temporären Kathode beschränkt ist und in dieser Schicht eine Elektronendichte von 10^{15} cm^{-3} und eine Gastemperatur von 1000 K erreicht wird. In der MHCD beträgt die Gastemperatur ungefähr 1500 K und die Elektronendichte $5 \cdot 10^{15} \text{ cm}^{-3}$. Beide Entladungen werden für die Messung von halogenierten Kohlenwasserstoffen eingesetzt, wobei die Probe entweder kontinuierlich mit dem Plasmagas eingeleitet oder vorher mit dem Gaschromatographen getrennt wird. Emissions-, Absorptions- und Massenspektroskopie werden als Detektionsverfahren der angeregten und ionisierten Spezies im Plasma verwendet. Hierbei werden Nachweisgrenzen im Bereich von wenigen pg/s erzielt. Diese Werte sind vergleichbar oder sogar besser als jene, die mit makroskopischen Entladungen oder kommerziellen Detektoren erzielt werden. Die miniaturisierten Plasmen weisen eine hohe Lebensdauer und Robustheit auf.

Contents

1	Introduction	1
2	Miniaturization of discharges	5
2.1	Physical background of miniaturized discharges	5
2.2	Different approaches to micro-plasmas	14
2.3	Sample introduction in miniaturized discharges	25
3	Instrumental techniques	29
3.1	Absorption spectroscopy	30
3.2	Emission spectroscopy	35
3.3	Line profile measurements	36
3.4	Mass spectrometry	37
4	The dielectric barrier discharge	41
4.1	Generalities about dielectric barrier discharges	41
4.1.1	Principle of dielectric barrier discharge	41
4.1.2	Applications of dielectric barrier discharges	43
4.1.3	Diagnostics so far	45
4.2	Low-pressure dielectric barrier discharge	46
4.2.1	Characterization of the discharge	46
4.2.2	Analytical application	59
4.3	High-pressure dielectric barrier discharge	73
4.3.1	Emission spectroscopy	74
4.3.2	Ionization source	76
5	The micro hollow cathode discharge	77
5.1	Generalities about MHCD	77
5.1.1	Principle of the (micro) hollow cathode discharge	77
5.1.2	Applications of hollow cathode discharges	79
5.1.3	Diagnostics so far	80

5.2	High-pressure MHCD	81
5.2.1	Characterization of the discharge	81
5.2.2	Analytical applications	94
5.3	Micro hollow cathode plasma jet	96
5.3.1	Adiabatic expansion	97
5.3.2	Plasma diagnostics	99
5.3.3	The MHCD as ion source for analytical MS	104
6	Conclusions & Outlook	113
7	Appendix	117
7.1	Coefficients for particle and energy balance	117
7.2	Coefficients for pressure broadening	119
	Bibliography	130
	Author's publication list	131
	Acknowledgements	133

One never notices what has been done;
one can only see what remains to be done.

Marie Curie, letter to her brother, 1894

Introduction

Miniaturization of chemical analysis becomes increasingly important. The aim is to “bring the lab to the sample” rather than relying on the sample being delivered to the lab. A conventional analytical process is done by collection of the sample, sending it to the laboratory, processing & analyzing it, and finally providing a feedback to the customer. This procedure is not only time consuming, but also requires a lot of man power, in some cases even highly educated personnel, which is quite expensive. Some steps can be automated, others not. However, all of these steps can be simplified by miniaturization, because “in-process analytics” becomes doable. As a consequence the production process can be automatically sampled, analyzed and controlled by applying a feedback-loop that uses the analytical result. Computers can assist and fasten the process and, additionally, dispense the pricey personnel. Fast analysis and automation are important factors in industrial processes and quality control as well as in environmental protection, and they enable significant progress in the medical genomic research. The aim is to fabricate complete analytical instruments that would fit in ones palm while having similar capabilities as full size instruments. This follows the continuous trend to reduce the size of everything, such as electronics and computers. Therefore, analytical chemistry is not to be left out, as miniaturization leads to shorter analysis times, lower reagent and sample consumption, and cost reduction.

Especially in life science and environmental protection, many analytical detection methods are based on plasma spectroscopy. These methods use an electrical discharge or a flame as dissociation, excitation and ionization source for mass, emission or absorption spectroscopy. For instance, techniques like inductively coupled plasma-mass spectrometry (ICP-MS), -optical emission spectrometry (ICP-OES) or flame absorption spectrometry (flame AAS) [Mon], are well established. Some of them are based on atomic detection, which are coupled to separation methods, like gas chromatography (GC) or electrophoresis.

The downscaling of the latter devices was already demonstrated in the late 1980s by Terry et al. [Ter79] who designed a gas chromatograph on a chip. However, for the reason that the classical detectors were incompatible in size, the development stagnated until Manz announced the “lab-on-a-chip” or “micro-total analysis system” (μ TAS) concept [Man90].

Since then, the interest in such devices has grown and small-sized analytical systems have become marketable, as shown by Agilent presenting a bioanalyzer based on microfluidic devices [Agi] or by Caliper Inc., which registered the trademark LabChip™[Cal].

The easiest way of miniaturization is the downscaling of the classical techniques, e.g. the combination of an electrical discharge with emission or mass spectrometry. For this process it is important not only to downscale the plasma itself, but also the side components, like the high voltage generator, the vacuum pumps, and the detection system. Therefore, it becomes necessary to use low power plasmas in order to keep both the power supply and gas consumption small. Nonetheless, it is demanded that the small-sized discharges are still robust enough for all kinds of sample.

Some similarity laws exist for the miniaturization of electrical discharges, but one still has to prove the validity of these rules by plasma diagnostics. Such fundamental investigations will enlighten the basic processes leading to good analytical performance and might help further development of discharges. Nevertheless, due to the small size of the investigated discharges, new methods have to be developed and improved. For these small dimensions, high spatial resolution spectroscopy is essential.

The presented thesis deals with the prospects and limits of miniaturized discharges for quantitative analysis. First of all, some background information for the miniaturization of electrical discharges will be given. The so-called “similarity laws” can be used to characterize the downsizing. However, prediction of these laws has to be corrected as the laws were developed only for low-pressure discharges, whereas miniaturized systems mostly consist of atmospheric pressure plasmas. This will also be shown in a chapter reviewing all documented approaches to miniaturized discharges for analytical science. An appraisal of the analytical strength of miniaturized discharges can be done by basic assumptions on particle and energy balances.

Two small-scale plasma sources that might be implemented in μ -total analysis systems were investigated experimentally. One is the dielectric barrier discharge, which is already widely used in plasma display panels, and the other is similar to the common hollow cathode discharges, but at a small-scale. Both fundamental plasma parameters and analytical performance were determined. As already mentioned above, new spectroscopic techniques had to be developed to achieve this aim. First of all, an arrangement with high spatial and temporal resolution was developed, which enables the measuring of difficult accessible parameters. Furthermore, the non-invasive diagnostics in high-pressure discharges require new techniques. The line profile analysis, as it is commonly used, fails in case of high-pressure discharges due to the incapability of deconvolution. Therefore, a new

procedure is proposed and tested for the analysis of the micro hollow cathode discharge. For analytical purposes, different spectroscopic techniques (emission, absorption, mass spectrometry) were applied to each discharge revealing the most appropriate method. The samples were introduced either with the gas flow directly or after separation with a GC. The results concerning atomic detection of volatile and gaseous halogenated compounds as impurities are compared with other miniaturized devices as well as with the techniques commonly used in analytical science.

2.1 Physical background of miniaturized discharges

Discharges have been operated in laboratories for about 200 years. As a result of practical reasons, most of them are relatively large devices. Over the last decades, there was a growing desire to miniaturize all equipment including the discharges. Downscaling of plasmas is a challenging task due to the different kinds of plasma processes which have to be taken into account. However, even before the idea of miniaturization appeared, scientists investigated the main processes in discharges with the aim to obtain a basic understanding for scaling discharge dimensions. The results were the so-called “similarity laws”, on which the following chapter will give an overview. Furthermore, an estimation on the power and energy balance in discharges and the consequences for miniaturization will be presented.

Similarity laws for discharges

Laboratory discharges are generated in a variety of ways: dc and ac voltages ranging from a few Hz to microwave frequencies (several GHz) can be applied to the electrodes in contact with the plasma or coupled inductively and capacitively. Furthermore, the plasma can be sustained in rare gas, synthetic air, or a mixture etc. with dimensions varying from a few micrometers to meters. Nevertheless, all discharges can be described by the same equations and the similarity laws that have been found. By the use of the similarity laws some characteristics of miniaturized discharges can be predicted. In this way, one can pass complicated numerical models, which, furthermore, would have to be carefully adapted to initial and boundary conditions.

Assuming that the discharge is completely governed by linear laws, a set of reduced quantities can be defined. Linear equations and processes are, for example, Maxwell’s law, ionization by electron impact, secondary electron emission, drift of charged particles in an electric field, and diffusion. Two discharge devices of similar shape should behave identically, if all the reduced quantities are the same for both devices. The most significant reduced discharge parameters will be presented. Proper scaling of a discharge device should keep these constant.

The most important law was named after Paschen [Pas89] describing the breakdown of a discharge according to the Townsend-mechanism. Generally, even before the plasma is ignited, few electrons are present in the discharge gap. In addition to background ionization as a result of cosmic rays, asperities of the electrode surface lead to a strongly enhanced electrical field and thus to field emission. Those electrons are accelerated towards the anode by the applied electrical field and ionize other gas atoms by collisions. The positively charged ions on their part are accelerated towards the cathode and bombard the surface, which leads to secondary electron emission. In order to achieve a self-sustaining discharge, the loss and generation of electrons and ions have to be equal. The breakdown voltage, starting a self-sustaining discharge in a planar geometry, is given by

$$V_b = \frac{Bpd}{\ln(Apd) - \ln[\ln(1 + \gamma^{-1})]}. \quad (2.1)$$

A, B gas dependent parameters
 p pressure
 d electrode distance
 γ number of secondary emitted electrons

Note that the voltage depends only on the product of pressure and electrode gap pd , which is the first reduced quantity. As a consequence, the operating pressure needs to be increased when the size of the device is reduced to obtain a similar discharge.

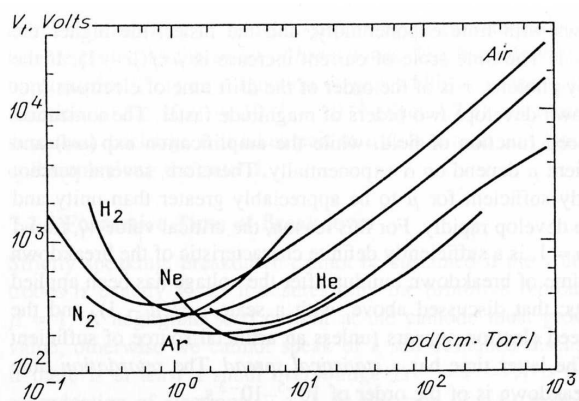


Figure 2.1: Paschen curve for various gases [Rai97].

A so-called vacuum and high-pressure insulation can be observed in the plot of the Paschen curve (see figure 2.1). In the case of small pd -values the gas density is too small to obtain efficient ionization, while in the case of high pd -values the mean free path for ionization is too small in order to accelerate the electrons. The minimum voltage is obtained for medium conditions, in which the mean free path approximates the electrode distance. As can be seen in the plot, the general correlation is the same

for all gases, but the absolute values vary.

For further considerations, a definition of similar discharges has to be made; in the common case, a discharge consists of two planar electrodes facing each other inside a cylindrical tube. By definition, all linear dimensions in such a discharge are reduced by a factor of a , this includes the distance between the electrodes d and the tube diameter R . Furthermore, the voltage V is kept constant. Using these basic assumptions, other relations for

plasma parameters can be derived. The scaling of all linear dimensions include the mean free path of the particles as well. It is for this reason that the gas density and pressure are scaled by $p_1 = p_2/a$. Knowing that the dimension between the electrodes was changed by $d_1 = d_2 \cdot a$, the product of pressure and electrode distance pd has to be constant. This is used in the Paschen law, in which the breakdown voltage is only dependent on pd and not on p or d reclusively.

The demand for identical potentials in both discharges at every point implies that the surface charge is scaled inversely with the proportional factor. Furthermore, the electrical field is converted in the same way ($E_1 = E_2/a$). If this relationship is combined with the pressure transformation, E/p has to be kept constant for similar discharges.

In addition to low frequency and dc discharges, these theorems can be extended to plasmas with extremely high frequency alternating fields, e.g. microwave induced discharges, as shown by Margenau [Mar48]. Since current and potential measurements are difficult, he defined two similar discharges in a different way. Thus, supplementary to the scaling of linear dimensions, the electron energy distribution function (EEDF) should be the same in both systems. In this case the reduced quantities fd , fR and f/p have to be kept constant, with f being the frequency of the discharge.

All transformations of plasma parameters for similar discharges are summarized in table 2.1. While the basic assumptions are enlisted in the upper third of the table, the middle one contains the relations which can be directly concluded. On the contrary, the lower third contains equations which are based on more assumptions than pointed out before. Some combinations of physical parameters can be obtained which remain constant by scaling the device. For historical reasons, these quantities are referred to pressure p , measured in Torr at 273 K, and not to the number density of gas molecules which would be more appropriate. The main reduced-quantities are given in the right column of the table 2.1.

If the scaling laws are used to describe downscaled discharges, one has to keep in mind that the laws were obtained in the late 1930s, when miniaturization of plasmas was not a major goal. Considering the reduced quantity pd , it is obvious that the pressure has to be increased by reducing the size. As a consequence that the similarity laws were developed for the low-pressure case, it is expectable that in high-pressure discharges non-linear effects and deviations from the simple linear model occur. One strong deviation from the similarity laws is due to the small volume and the increased loss of particles at the wall. Furthermore, as the pressure is increased (and d is decreased), the number of molecular collisions grows leading to unwanted side reactions, in which charged particles are increasingly lost.

parameters	relationship	invariant groups of parameters derived – similarity parameters
potential	$V_1 = V_2$	V, i, T
linear dimensions (electrode distance, tube radius)	$d_1 = ad_2,$ $R_1 = aR_2$	consequently all $V - i$ curves
current	$i_1 = i_2$	
gas temperature	$T_1 = T_2$	
mean free path of any particle	$\lambda_1 = a\lambda_2$	
gas density	$n_1 = n_2/a$	
gas pressure	$p_1 = p_2/a$	
electric field	$E_1 = E_2/a$	$E/p, pd, pR$
wall charge density	$\sigma_1 = \sigma_2/a$	
volume charge density	$\rho_1^{+, -} = \rho_2^{+, -}/a^2$	
total mass of gas	$m_1 = a^2m_2$	
total charge in vessel	$q_1 = aq_2$	
total and partial current density	$j_1^{o, +, e} = j_2^{o, +, e}/a^2$	
particle density ¹	$N_1 = N_2/a^2$	T_e, T_+
excited states, except resonance	$N_1^* = N_2^*/a^3$	H/p
velocity, energy of charged particles	$v_1 = v_2 \quad \epsilon_1 = \epsilon_2$	$j/p^2, N_e/p^2$
electron, ion temperature	$T_1^{e, +} = T_2^{e, +}$	
time interval	$dt_1 = adt_2$	
collision frequency	$\nu_1 = \nu_2/a$	and for all
applied frequency	$f_1 = f_2/a$	ac discharges
magnetic fields	$H_1 = H_2/a$	$fd, fR, f/p$
rates of current growth	$di_1/dt = 1/a \cdot di_2/dt$	

Table 2.1: Similarity transformations for discharge parameters [Fra60]. ¹ particle density: electrons, ions, metastable (assuming that they are produced only by direct excitation, and not by electrons falling from higher levels), fast neutrals (by charge transfer)

Two examples of such processes are (i) the formation of molecular ions by the reaction $\text{He}^+ + 2 \text{He} \rightarrow \text{He}_2^+ + \text{He}$ with subsequent dissociative recombination $\text{He}_2^+ + e^- \rightarrow 2 \text{He}$ and (ii) recombination $\text{He}^+ + 2 e^- \rightarrow \text{He} + e^-$ [Eij99]. The reaction rate of these processes is given by the scaling laws for charged particles. Due to the law of mass action, whereby the reaction rate is proportional to the density of the species, the first and second reaction scales with p^4 and p^6 , respectively. Diffusion only scales with p^3 . So the loss of charged particles might be substantially higher¹ than predicted by scaling of macroscopic discharge. This leads to a higher discharge voltage and electron temperature than predicted as the extra loss has to be made up by extra ionization. One way to

¹For a more detailed examination, the cross sections of the processes have to be taken into account.

overcome this problem is the use of an adequate material with high secondary electron emission.

Generally speaking, miniaturized discharges are non-equilibrium plasmas in which the gas temperature is lower than the electron temperature. The time to equalize both temperatures is given by Kono et al. [Kon01]

$$\tau_1 \simeq \frac{M}{m} \frac{1}{\sigma v_e n_e}, \quad (2.2)$$

m, M	electron, gas molecule mass
σ	momentum transfer cross section
v_e	average thermal velocity
n_e	electron density

while the average time for the loss of kinetic energy by collision with the cold wall is

$$\tau_2 \simeq \frac{l^2}{D_a}. \quad (2.3)$$

l	representative dimension
D_a	diffusion constant

Typical values for the parameters are given in table 2.2. For example, the thermalization time is larger than the cooling time if the dimension of a plasma is smaller than 500 μm and the electron density is in the order of $10^{14} - 10^{15} \text{ cm}^{-3}$. This means that the plasma does not reach equilibrium and keeps a high electron temperature. A higher electron temperature will be beneficial for the excitation and ionization of an analyte, while a lower gas temperature will be beneficial for the lifetime of the device.

D_a	0.3 cm^2/s
M/m	10^5
σ	10^{-15} cm^2
v	10^8 cm/s

Table 2.2: Typical parameters [Kon01].

Nevertheless, if the current and voltage are kept constant, the same power will be distributed into the discharge. Conclusively, the power density scales with p^3 . A strong temperature gradient (proportional to p) between the interior of the plasma and the wall is the consequence, which results in material stress. Therefore, due to technical reasons, one has to deviate from the scaling according to the similarity laws. In practice it is difficult to remove the thermal power from the plasma source in order not to destroy the device by overheating.

Energy and particle balance of small sized discharges

Many problems occur by downscaling the common plasma sources. In addition to the scaling laws, it has to take into account that the mean free path of the particles in the plasma is in the order of the discharge dimensions. Therefore, the loss by diffusion and collision of the particles with the discharge walls will be dominant and stronger than in the case of larger plasma sources. Hence, for a more detailed characterization of microplasmas, the particle and energy balance equations of free electrons have to be solved.

Both equations give information about the particle production and destruction as well as the energy input and losses. Based on the interesting work of Jonkers [Jon98], who investigated “Excitation and transport in small scale plasmas”, this section will illustrate aspects of the different loss and production rates of analytical microdischarges.

The particle balance

If a plasma is in steady state, the number of electrons should stay constant, which is summarized in the particle balance, whereas the ionization (production of electrons and ions) should equal the loss due to recombination, convection and diffusion:

$$n_e n_g S_{CR} = n_e n_+ \alpha_{CR} + \nabla(n_e \vec{u}) - \nabla \cdot (D_a \nabla n_e). \quad (2.4)$$

n_e , n_g and n_+ are the electron, gas, and ion density, respectively. The left term represents the electron production by ionization with the rate coefficient S_{CR} . The first term on the right side represents the electron – ion recombination loss proportional to the recombination coefficient α_{CR} . The last two terms are losses by outward transport, either determined by the gas flow u or by diffusion with the ambipolar diffusion constant D_a (1st Ficks law). The equation can be simplified by reducing the derivations to

$$n_e n_g S_{CR} = n_e n_+ \alpha_{CR} + \frac{n_e u}{l} + \frac{n_e D_a}{\Lambda^2}, \quad (2.5)$$

with l and Λ being the length of the chamber and the gradient length of n_e , respectively. In a first approximation, Λ is given by the size of the chamber. It can be noticed that the sign of the diffusion term changed: a reasonable density profile for an ionizing plasma and a zero wall electron density has a negative value for the second derivative. The parameters $S_{CR}(T_e)$, $\alpha_{CR}(T_e)$, $D_a(T_g, T_e, n_g)$ are complex functions of electron temperature (T_e) and gas temperature (T_g) as well as electron density (n_e), and were obtained by Jonkers et al. using a collisional radiative (CR) model. They are listed in the appendix.

As can be noticed in equation 2.5, the exact value of the electron density is not important, since all terms scale with n_e . Therefore, each term divided by the electron density can be regarded as a specific loss rate, which is plotted for different discharge operations in figure 2.2.

In (a), the rates are given for a classical dc discharge (two plane electrodes faced parallel) with a typical value of the gas temperature of 500 K at 10 mbar and a discharge dimension of 1 cm. At electron temperatures lower than 1 eV (typical for low-pressure dc discharges), the generation of free electrons and the destruction (by recombination and outward transport) are in balance. The loss rates due to recombination and diffusion are similar, while the convection is negligible. In figure 2.2 b the loss rates for a micro hollow

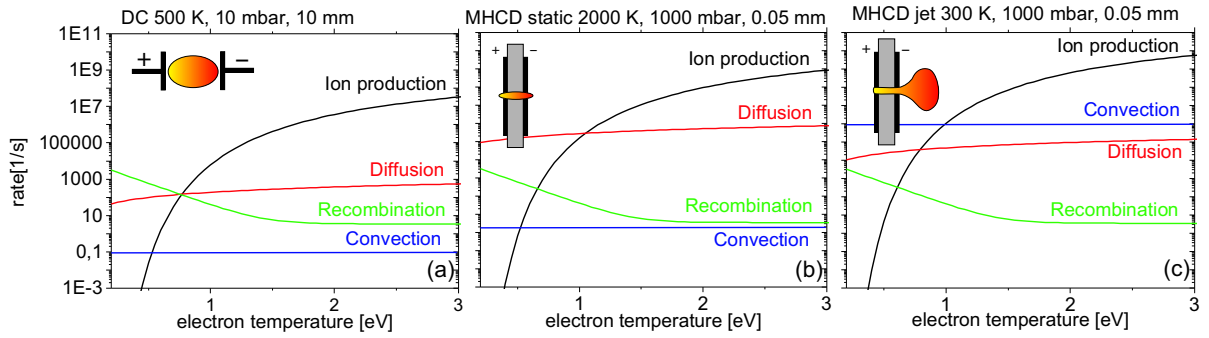


Figure 2.2: Typical particle generation and loss rates of different argon discharges (layout of each discharge sketched in the upper part); discharge type, pressure and size given.

cathode discharge (MHCD) in static mode (more details in section 5.2) are modelled. This discharge is generated in the bore of a structure made of an insulator (grey) and two attached electrodes (black). The discharge with a diameter of $100\ \mu\text{m}$ is operated at atmospheric pressure and gas temperatures up to $2000\ \text{K}$ are expected. It is obvious in this case that, since dimensions are small, the diffusional loss outweighs all other losses. Furthermore, the electron temperature has to be higher in order to compensate the losses. In figure 2.2 c, rate coefficients are given for a micro hollow cathode jet (more details in section 5.3). In this system, the gas expands through the discharge hole mentioned above with a high velocity which results in a reduced gas temperature. In this case, the convection loss outranges the others. In general, this loss depends on the specific discharge geometry, the flow and application used. For miniaturized discharges, the exchange rates, defined as the ratio of the gas flow to the plasma volume, of $1 - 10^6/\text{s}$ are observed (see table 2.13 in the next section). However, most of them are below $10^5/\text{s}$. Therefore, it can be concluded that the diffusional loss is the most dominant in miniaturized discharges and it is supplemented by convection loss in rare cases. Consequently, for a more detailed investigation of small-scaled plasmas, equation 2.5 can be simplified neglecting the contribution due to recombination and convection. Furthermore, the plots show that, for a continuous operation of the discharge, the electron temperature has to be high enough in order for the ion production to outrange the losses. This is explained in more detail in figure 2.3. Using only the data on ionization and diffusion, the particle balance equation can be solved, yielding the electron density as a function of the gradient length Λ with the gas density as free parameter. Thus, maybe surprisingly, T_e is independent on the applied electrical power, and is set only by the gas type, pressure and discharge dimension. The red and green curves represent a low and high-pressure discharge with $300\ \text{K}$ at $10\ \text{mbar}$ and $2000\ \text{K}$ at $1\ \text{bar}$, respectively².

²It has to be mentioned that gas temperatures of $2000\ \text{K}$ are observed rarely in helium discharges and are normally lower than in argon discharges. Nevertheless, for a facile estimation, the temperature was assumed to be equal in both gases.

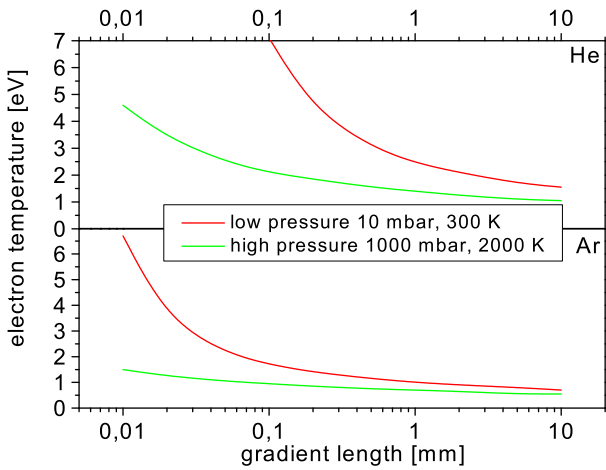


Figure 2.3: Electron temperature in helium and argon plasmas as estimated from the particle balance.

As can be seen, when decreasing the plasma size, the electron temperature has to increase for a particle balance, in a low-pressure discharge even more than in a high-pressure plasma. This is due to the fact that the diffusion is greater in small, low-density gases than in large, high-pressure gases. Additionally, electron temperatures in helium are approximately twice as high than in argon plasmas operated at the same conditions. This difference is mainly caused by the fact that the

first excited state of helium has a higher excitation potential than that of argon.

Energy balance

A simplified power balance equation of the free electrons is given, assuming that the input power density ϵ equals the power per unit of the volume that is lost by the free electrons in inelastic and elastic collisions:

$$\epsilon = n_e n_g S_{CR} E_I + n_e [n_+ \langle \sigma_{ei}^m \nu_e \rangle + n_g \langle \sigma_{ea}^m \nu_e \rangle] \frac{2m_e}{M} \frac{3}{2} k_B (T_e - T_g). \quad (2.6)$$

The first term represents the inelastic electron – atom collision which results in ionization. This process is determined by the ionization coefficient S_{CR} and the ionization potential E_I . The following two terms describe elastic electron – ion and electron – atom collision, leading to a momentum transfer. Here, $\langle \sigma_{ei}^m \nu_e \rangle$ and $\langle \sigma_{ea}^m \nu_e \rangle$ represent the adequate collision rate coefficients for momentum transfer averaged over the Maxwellian electron energy distribution function. Values for all coefficients in dependence on electron temperature and density can be found in [Jon98] and are enlisted in the appendix. It has to be mentioned that, in this simplified balance, the energy which is required to heat the cold electrons being produced in the ionization process ($5/2 k_B T_e$) is neglected.

Figure 2.4 displays the power density for the three discharge cases mentioned above. As it was already noted, the power density in the dc discharge (a) is much smaller than in miniaturized discharges because of the larger volume. The main energy loss is caused by electron – atom collisions, while ionization dominates in the high-pressure micro hollow cathode discharge (b,c). For this reason the gas temperature for conventional low-pressure discharges can easily be determined by the heat equation, assuming that the main power

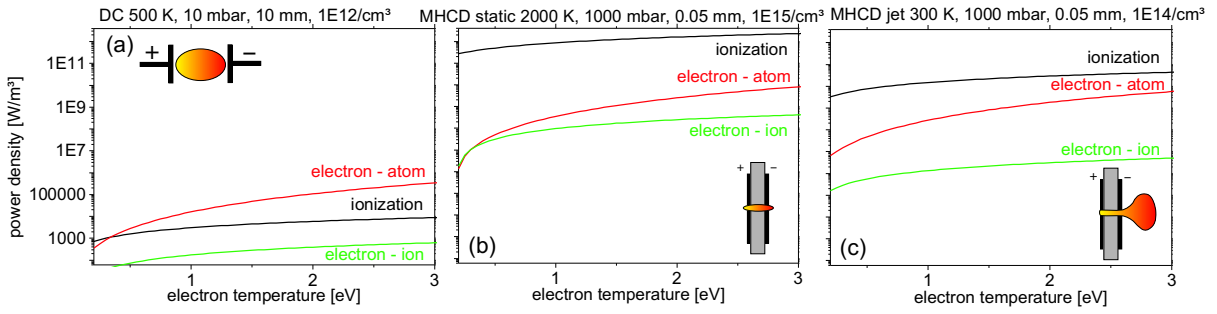


Figure 2.4: Typical power densities of different argon discharges (gas temperature, pressure, size and electron density given).

is used for gas heating, while no prediction can be made for miniaturized discharges.

Solving the equation 2.6 and neglecting radiation losses, the electron density as a function of the power density for a given electron and gas temperature can be obtained. This is plotted for atmospheric pressure discharges in argon and helium in figure 2.5. In this case, the electron temperature is determined by the solution of the particle balance equation, so the electron density is only expressed by the two macroscopic parameters ϵ and Λ .

For small gradient lengths, the loss of free electrons due to diffusion is relatively high and almost all the power is consumed in the production of charged particles as can be seen in the micro hollow cathode discharge. The elastic energy loss can be neglected which results in an electron density proportional to the power density. In this way, an electron density for the static mode of the MHCD at atmospheric pressure of more than 10^{15} cm^{-3} can be predicted (see also experimental results in section 5.2). Furthermore, it can be seen that the electron density in an argon discharge will always be higher than in

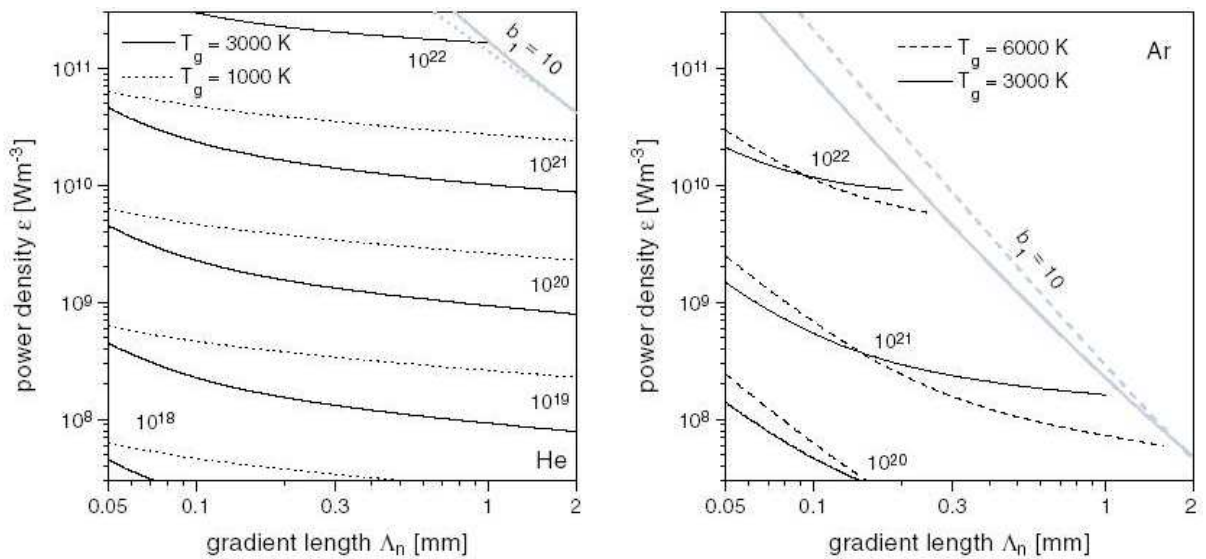


Figure 2.5: Electron densities (in m^3) in atmospheric helium and argon plasmas as obtained from the simplified energy balance for atmospheric pressure, taken from [Jon98].

a helium discharge. The region in which this model is applicable is indicated by the gray line ($b_1 = 10$). This parameter is given as the ratio of the ground state density observed and the ground state density expected, if the plasma is in equilibrium according to the Saha equation. For $b_1 < 10$ the plasma is not strongly ionizing anymore and some of the simplifications applied lose their validity.

In general, it can be concluded that miniaturized discharges are always far from equilibrium, having an electron temperature much higher than the gas temperature in the range of more than 1 eV, and an electron density larger than 10^{14} cm^{-3} . These values differ strongly from those for a conventional low-pressure discharge, which are formerly used in analytical spectrochemistry. However, these conditions favor the dissociation and excitation of analytes and make these plasmas a powerful tool for analytical science.

2.2 Different approaches to micro-plasmas [‡]

The development of micro-machining tools and techniques in the last fifty years was the basis of device shrinking. The plasma devices followed the same trend and, for about ten years, scientists have been focusing on the miniaturization of discharges. They are commonly used for a variety of applications, like excimer light sources, for bio-medical surgery, sterilization, ozone generation, etc. In the following section, a short review restricted to analytical micro-plasmas will be given [Fra03, Bro02].

Miniaturized direct current plasmas

A molecular emission detector on a glass chip employing a miniaturized direct current helium plasma for molecular fragmentation and excitation has been presented by Eijkel et al. [Eij99, Eij00, Bes02]. Figure 2.6 shows a typical schematic chip layout consisting of a top and bottom plate. The channels and the plasma chamber were produced by HF-etching. The electrodes were formed by deposition of 50 nm chromium and 250 nm of gold. Gas inlet and outlet holes of 400 μm diameter were drilled by ultrasonic abrasion. The plasma was generated in chambers of different geometrical dimensions, varying the chamber volume, the electrode distance, the inlet and outlet channel as well as the equivalent radius of the plasma chamber. In a first experiment, inlet and outlet channels were chosen to obtain a plasma chamber pressure of about 100 hPa and, in a following work, they were modified to reach atmospheric pressure.

[‡]Part of this chapter has been published in slightly different form in *Microplasmas for analytical spectrometry*, J. Anal. At. Spectrom. **18**(2003) 802 – 807 [Fra03].

The chambers with volumes of 50 – 200 nl and with flow rates of 5 – 500 nl/s, were used in order to determine the limit of detection of methane in a helium gas flow by measuring molecular spectral emission of CH bands. The limit of detection was in the range of pg/s (ppb – ppm). Furthermore, the plasma, generated in helium with an applied power of 9 mW (770 V, 12 μ A), was coupled with a conventional gas chromatograph. A number of carbon-compounds were detected in the column effluent recording the CO-emission at 519 nm. For hexane, the detector showed a linear dynamic range over two decades and a detection limit of 10^{-12} g/s (800 ppb). The device was operated for more than 24 h without a significant change in performance. Recently, atomic detection of bromine and chlorine for this dc plasma was reported [Bes02]. A similar micro-plasma chip with a chamber size of $2 \times 0.07 \times 0.07$ mm³ and 125 mW power was coupled to the gas chromatograph. Spectroscopic detection of elements and molecular fragments in the eluted peaks was demonstrated. Using the 479.5 nm emission line and taking into account the injected amount of chlorinated compounds, a detection limit of 800 pg/s for chlorine was found.

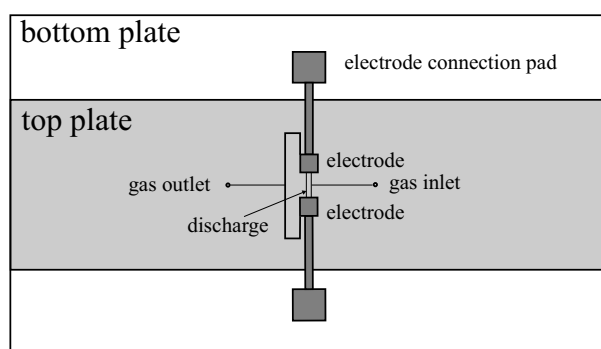


Figure 2.6: Schematic chip layout of the direct current discharge used by Eijkel et al. after [Eij99].

Longwitz et al. developed a micro-glow discharge as an ion source for ion mobility spectrometry [Lon03]. The device was microstructured on fused silica and pyrex wafers. The planar electrodes consisted of a 300 nm metal layer on a 10 nm Cr adhesion layer. Pt and Au were used as the electrode material. The fused silica substrate below the Pt electrode was dry etched to a depth of 5 to 10 μ m in order to obtain freestanding electrode edges. The substrate next to the Au electrodes was not etched. The devices were placed in a vacuum system in which gas type and pressure were adjusted. Breakdown was studied for electrode gaps of 1 to 50 μ m. Stable dc glows at atmospheric pressure were obtained in Ar and in N₂ using 1 μ m and 3 μ m gaps, respectively. Gas voltages of 500 V and discharge currents of a few μ A resulted in a power input of several μ W. Ion extraction was only demonstrated for a larger system of 100 μ m discharge gap, obtaining ion currents of 100 pA. Current and power were 3 orders of magnitude higher, mA and mW, respectively. Considering the sputtering of cathode material, the lifetime of the structure was limited to a few hours.

The use of solution as one of the electrodes

A method named “electrolyte as a cathode discharge” (ELCAD) has been developed by Cserfalvi et al. to perform continuous monitoring of trace metals dissolved in water via glow discharge-atomic emission spectrometry (GD-AES) [Cse93]. An open and continuously flowing fountain of the sample solution was used as the cathode in the discharge. More recently, a very small glow discharge for optical emission spectroscopy (GD-OES) has been described by Marcus et al. [Dav01, Mar01]. This device, which is called “liquid-sampling atmospheric-pressure glow discharge” (LS-APGD), has been developed for the analysis of metals in electrolyte solutions. An abnormal glow discharge was formed between the electrolyte solution in a capillary and a Cu counter electrode. The liquid in the capillary either acted as the cathode or the anode of the discharge. Stable discharges could be realized with flow rates of 0.5 – 1.5 ml/min using hydrogen, sodium or lithium as the electrolyte species. Discharge currents of 25 – 60 mA and voltages of 300 – 1000 V were applied. Analytical response curves were generated for the elements Na, Fe, and Pb, with an absolute limit of detection in the order of 60 ng obtained for 5 μ l sample injections.

Jenkins et al. presented the feasibility of performing AES with liquid samples on a glass microchip using the ELCAD technique, achieving a thousand fold smaller sample flow rate [Jen02]. Copper was detected by atomic emission spectroscopy, but an assignment of detection limits was not possible due to instabilities of the discharge and, consequently, fluctuating background and signals.

In the same year, Wilson et al. [Wil02] used the same principle with one electrode being the liquid analyte. The on-chip micro-glow discharge was coupled with a small optical spectrometer (Ocean Optics). Emission detection limits for sodium, lead, aluminum and chromium of 10, 5, 5 and 10 ppm, respectively, were obtained. Furthermore, by changing the polarity of the supplied voltage, they proved that the signals are obtained by positive gas ions from the discharge sputtering the cathode. It was shown that the dominant impurity delivery mechanism was sputtering from the cathode as opposed to fluid heating and vaporization. This is an important feature of the arrangement because it permits nonvolatile, inorganic impurities to be introduced into the plasma. It eliminates the need of spraying the water into the plasma, which is the approach used in conventional devices.

Miniaturized pulsed plasma detectors

A low power plasma detector for molecular emission spectrometry has been described by Jin et al. [Jin01]. This detector consisted of two platinum plate electrodes of 0.04 mm

thickness and 3 mm width, placed face to face in a 40 mm long Teflon tube (outer diameter 7 mm). The distance between the electrodes was 1.5 mm. The plasma was generated in He with a homebuilt high voltage pulsed power supply at atmospheric pressure. The average operational power of the detector was smaller than 0.2 W. Because of the low power requirement, the detector could be operated with two 1.5 V alkaline batteries for more than 10 h. The influence of plasma gases, flow rates, and discharge voltages on the performance of the detector as well as the reproducibility and sensitivity of the detector to organic vapors were studied using dimethyl sulfoxide. The device was improved by reducing the diameter of the capillary tube to 1.5 mm [Dua03]. In this case, flow rates and average power as low as 0.16 ml/min and tens of mW, respectively, were used to sustain the discharge. Methane, dichloromethane and toluene introduced by chemical vapor introduction could be detected by emission spectroscopy monitoring the CH-band (431 nm) down to 2.8, 16 and 2.6 ng/ml, respectively. A pre-separation of analytes was achieved by a capillary column sampling, using a 0.53 mm capillary. Even after several months, no deterioration of the device could be observed.

Capacitively coupled microplasmas at 13.56 MHz

A miniaturized, parallel plate capacitively coupled plasma (PP-CCP) at atmospheric pressure has been investigated for analytical atomic spectrometry applications. The PP-CCP was sustained by application of radio frequency power to a pair of electrodes that were separated by a quartz discharge tube, forming a capacitive, transverse discharge. The plasma was normally operated at 13.56 MHz using He as a plasma gas. However, other gases and frequencies could be used as well.

Bass et al. described the implementation of the PP-CCP on a $0.25 \times 0.25 \times 5 \text{ mm}^3$ micro-machined fused silica chip [Bas01]. The He plasma, schematically shown in figure 2.7, was operated at atmospheric pressure and was self-igniting. The power was 5 – 25 W and the gas flow was between 17 and 150 ml/min. The authors claimed that parallel plate capacitive power coupling is nearly ideal for generating and sustaining a

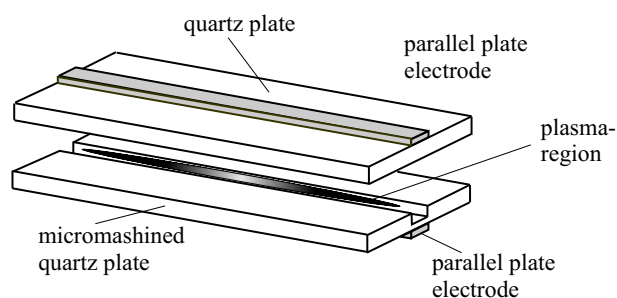


Figure 2.7: Exploded schematic view of the capacitively coupled micro-plasma discharge chamber used by Bass et al. after [Bas01].

plasma discharge on a chip since it can be implemented using a very simple electrode structure and does not require tuned or resonant structures. The quartz torch was mounted between two copper electrodes. The bottom electrode was contacted to a grounded cop-

per block, and also served as a cooling element for the plasma torch. The upper electrode was 1 mm wide. The electrodes could also be made by vapor deposition in order to build a more compact source and, if necessary, by electrode patterning in order to generate several plasma discharges on a single wafer. The emission lines of OH, NH, N₂, N₂⁺ and He were measured applying a 20 W He plasma and a gas flow of 70 ml/min. Although the PP-CCP has been investigated for application in analytical atomic spectrometry, no element selective measurements have been done by Bass et al. with the miniaturized version so far.

A similar capacitively coupled microplasma, named CCMP source, at atmospheric pressure was described by Yoshiki et al. [Yos01]. It was realized on a quartz chip of 20 x 20 mm² consisting of two glass plates with a thickness of 500 μm and a spacer between the plates of 65 – 500 μm. The thickness of the spacer determined the depth of the capillary. Parallel-plate electrodes of 5 x 5 mm² were externally attached to the quartz chip so that the capillary was sandwiched between the electrodes. The He plasma was generated in channels with cross sections of 65 – 500 x 500 – 5000 μm. The length of the plasma inside the capillary was the same as the length of the electrodes. The plasma was operated by a conventional operation frequency of 13.56 MHz and was ignited by an incident power between 1 and 3 W in the range of 80 hPa to atmospheric pressure. Various He emission lines and the lines of O and OH were obtained. The He atomic excitation temperature was estimated to be about 2000 K. The incident power and the gas flow rate were 5 W and 475 ml/min, respectively. The CCMP was supposed to be of potential use as an on-chip plasma device, but, so far, only material treatment and no analytical measurements have been performed. Recently, the same generator has been used to obtain microdischarges similar to CCP and ICP in tubes with an internal diameter of 1 mm [Tan03]. Even 3-d integrated plasmas were generated by multiple tubes, which were closely aligned and stacked in a sandwich structure.

Last year, Hauser et al. developed a third kind of miniaturized capacitively coupled plasma [Guc03] using a much lower frequency. They used a fused capillary and two cylindrically shaped electrodes around it. The capillary had an inner and outer diameter of 150 μm and 350 μm, respectively. The discharge was sustained with a voltage and frequency up to 20 kV and 20 kHz, respectively. The authors mentioned that a comparatively inexpensive power supply can be realized using a transformer with an input voltage of 12 V. An Ocean Optics spectrometer was applied for emission spectrometry, and Hg, As and Sb after hydride generation could be detected down to few hundred ppb. The helium excitation temperature was estimated to 12 000 K. The device consumed 8 W of electrical

power and worked with gas flows in the range of ml/min. Lately, this microplasma was coupled with a gas chromatograph in order to separate organic [Guc04b] and inorganic compounds [Guc04a], obtaining detection limits of pg to ng.

Miniaturized inductively coupled plasmas

A very interesting miniaturized plasma is the downscaled ICP. Whereas large-size ICP's are typically operated at a frequency of 13.56 MHz, Hopwood et al. showed that the optimum frequency for plasma generation increases up to 460 MHz if the coil diameter is reduced to 5 mm [Yin99]. It was found that the electron density is about one order of magnitude lower than in large scale ICP. However, it was also shown that the electron density increases with the frequency. The miniature ICP (mICP) was fabricated by etching planar spiral inductors in a copper clad epoxy board. Another paper reported on the microfabrication and testing of monolithic mICP fabricated on glass wafers using surface micromachining [Hop00].

A scheme of the discharge chamber is given in figure 2.8. The plasma was sustained coupling a 450 MHz voltage into a low-pressure gas. Ar as well as air plasmas have been generated in the range of 0.1 – 13 hPa. The operational power was 350 mW, although 1.5 W was required to initiate the discharge. A new single-loop mICP source, which was three times more efficient than the former one, has been fabricated [Iza02].

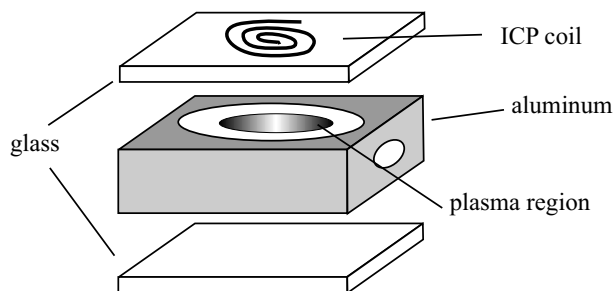


Figure 2.8: Exploded schematic view of the inductively coupled micro-plasma used by Hopwood et al. after [Min02].

In this case the coil was situated closer to the plasma and was operated with even higher frequencies up to 818 MHz. Ion densities of 10^{11} cm⁻³ in Ar at 0.5 hPa were obtained with only 1 W of power. Lately, first calibration curves for SO₂ were measured in an Ar mICP by optical emission spectrometry of the sulfur atomic line at 469.5 nm. The plasma chamber consisted of a cylindrical hole of 6 mm in diameter and 6 mm in length. The pressure was 7.4 hPa and the plasma power 3.5 W. The limit of detection of SO₂ was about 190 ppb_{v/v} [Min02].

Recently, an atmospheric pressure microplasma jet source was developed by Ichiki et al. [Ich03], which consisted of an inductively coupled plasma on a ceramic chip with a discharge tube engraved onto it and a planar metallic antenna with serpentine structures.

The size of the discharge channel was $1 \times 1 \times 30 \text{ mm}^3$ (h/w/l), and a VHF power of 50 W was used. The electron density and excitation temperature in argon were determined to be 10^{14} cm^{-3} and 4000 K, respectively. A liquid sample of sodium standard solution was introduced by electrospray injection, and a preliminary detection limit of 5 ppm Na in emission at 589 nm was obtained.

Microwave induced plasmas based on microstrip technology

Bilgic et al. at the University of Dortmund described a new low-power small-scale 2.45 GHz microwave plasma source based on microstrip technology which can be operated at atmospheric pressure, and can be used for atomic emission spectrometry [Bil00, Eng00, Sch03]. This MIP is named Micro Strip Plasma (MSP). The MSP was integrated in a quartz wafer and designed as an element-selective detector for miniaturized analytical applications. The quartz wafer was a sandwich of two quartz plates shown in figure 2.9. The dimension of each plate was $1 \times 33 \times 90 \text{ mm}^3$. Both plates were glued together by water-glass and had a gas channel of either 0.9 or 0.64 mm diameter.

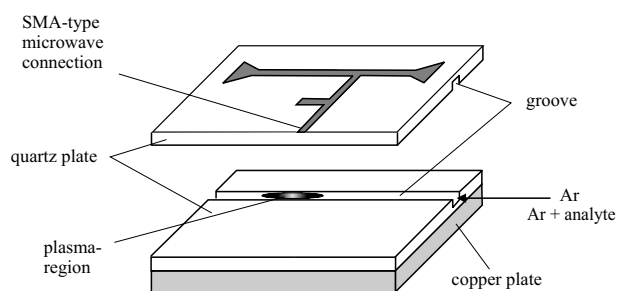


Figure 2.9: Exploded schematic view of the microstrip microwave induced plasma chamber used by Engel et al. after [Bil00].

The wafers were mounted on a copper plate that works as the ground electrode and as cooling block. On the upper plate, there was a copper electrode of $30 \mu\text{m}$ thickness. This electrode consisted of a small strip placed over the gas channel, a small matching device and an electrical contact to a microwave connector (not shown in figure 2.9). The MSP operated at a microwave input power of 1 – 40 W and Ar gas flows of 50 – 1000 ml/min. It was shown that no homogeneous plasma was formed if the plasma gas flow was very low. Therefore, all measurements were performed with a plasma gas flow of 300 ml/min and a forward power of 30 W. Rotational (OH) and excitation (Fe) temperatures were found to be 650 and 8000 K, respectively. Hg was determined by applying the flow injection cold vapor (FI-CV) technique with a detection limit of 10 pg/ml. Furthermore, diode laser atomic absorption spectroscopy (DLAAS) measurements of halogenated hydrocarbons introduced in a helium discharge revealed detection limits of 5 ppb [Kun01]. Recently, the plasma volume was reduced with an equivalent geometry and similar detection limits [Sch03].

The wafers were mounted on a copper plate that works as the ground electrode and as cooling block. On the upper plate, there was a copper electrode of $30 \mu\text{m}$ thickness. This electrode consisted of a small strip placed over the gas channel, a small matching device and an electrical contact to a microwave connector (not shown in figure 2.9). The MSP operated at a microwave input power of 1 – 40 W and Ar

Miniaturized radio frequency plasma at 350 kHz

A radio frequency plasma (RFP) working at 350 kHz was miniaturized by Pedersen-Bjergaard et al. [PB93, PB94]. A 5 cm long piece of polyimide coating and the stationary phase were carefully burned off at the end of a fused silica GC column. The last 2 cm of this uncoated GC capillary served as the plasma tube placed inside a piece of silica tube for protection. A steel wire placed at the column outlet served as the top electrode as shown in figure 2.10. The plasma was generated inside the end of the fused silica GC column between the top electrode and the grounded reducing union by a radio frequency power supply. Atomic emission was measured side on through the wall of the fused silica column and the protecting silica tube. The detection limits for bromine and chlorine were 0.9 and 1.1 pg/s, respectively.

A different paper reported on the application of this plasma device for mass spectrometric detection in capillary gas chromatography [Bre98]. The plasma was sustained at low-pressure in the last 35 mm of a capillary GC column (0.32 mm i.d.), which was put inside of the ion source housing of a quadrupole mass spectrometer. This allowed direct introduction of ions from the plasma into the mass analyzer using only a repeller and electrostatic lenses to focus the ions. The plasma was sustained with a flow of only 25 ml/min helium, which was accepted by the mass spectrometer vacuum system. This low gas flow also served to enhance the energy density of the discharge and to produce a narrow spray of ions toward the mass analyzer.

Due to the miniaturized nature of the plasma, it was operated at a low power level (2 W), and traces of oxygen were added to avoid deposition of carbon on the capillary wall. Chlorine was successfully monitored down to the 2.2 pg/s level without interference from elements such as C, S, P, O, F, or N.

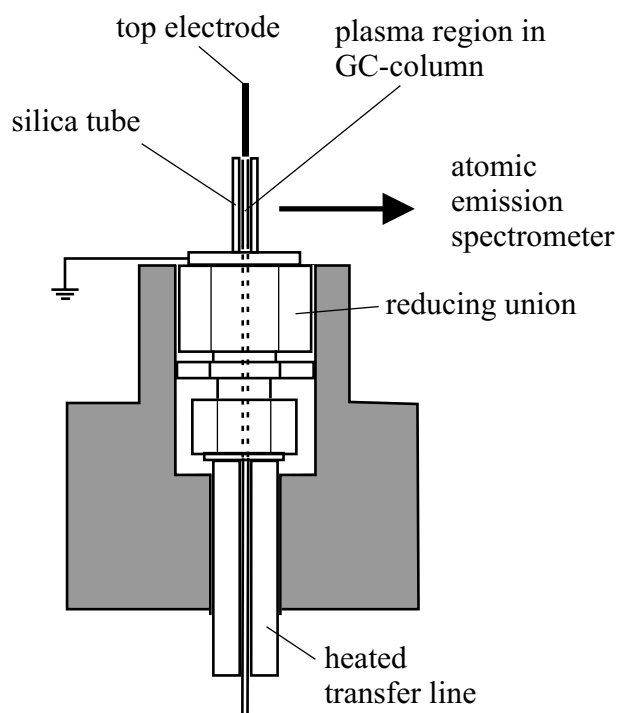


Figure 2.10: Schematic layout of the radio frequency plasma used by Pedersen-Bjergaard et al. after [PB94].

Dielectric barrier discharge

The dielectric barrier discharge (DBD) is one topic of the thesis and will be discussed in detail in chapter 4. The discharge chamber (schematically shown in figure 2.11) consisted of two glass plates covered with aluminium electrodes (length 50 mm, width 1 mm). The electrodes were covered with a 20 μm thick glass type dielectric layer. The glass spacers between the glass plates defined the distance of 1 mm between the electrodes and formed the plasma channel of $1 \times 1 \times 50 \text{ mm}^3$.

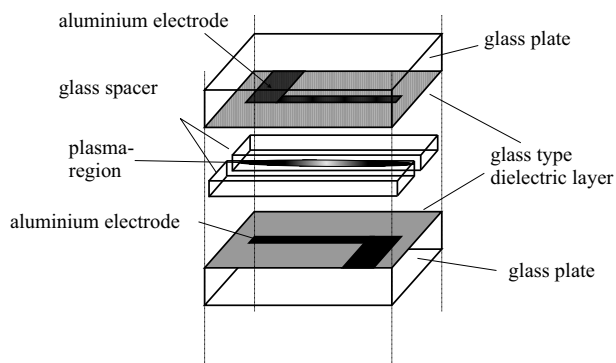


Figure 2.11: Exploded schematic view of the dielectric barrier discharge chamber.

atomic absorption spectrometry revealed detection limits for CCl_2F_2 in the He DBD of about 400 ppt_{v/v} and 2 ppb_{v/v} using the Cl 837.824 nm and the F 685.792 nm line, respectively.

Micro hollow cathode discharge

The micro hollow cathode discharge (MHCD), which is the second topic of this thesis, is a multilayer system consisting of two metallic foils separated by an insulator. It will be presented in detail in chapter 5 and is schematically shown in figure 2.12.

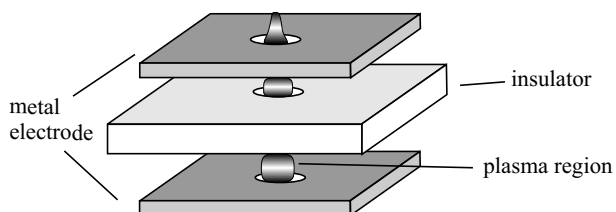


Figure 2.12: Exploded schematic view of the micro hollow cathode discharge

detection of chlorine and fluorine resulting from the decomposition of the halogenated

The discharge worked at reduced pressures of 10 – 100 hPa in argon as well as in helium with a gas flow of 10 – 1000 ml/min. A voltage of 750 V_{pp} was applied; its time curve had a rectangular shape and a frequency of 5 – 20 kHz. The mean power consumption of the discharge was much smaller than 1 W, but – as will be shown later – the plasma was restricted for a short time to a small volume. Measurements of halogenated hydrocarbons by diode laser

atomic absorption spectrometry revealed detection limits for CCl_2F_2 in the He DBD of about 400 ppt_{v/v} and 2 ppb_{v/v} using the Cl 837.824 nm and the F 685.792 nm line, respectively. The thickness of the layers was typically 30 – 150 μm . A bore with a diameter of 10 – 500 μm was drilled through the structure. A plasma was produced inside the hole between the electrodes in noble gases, gas mixtures or air using ac or dc current voltage. Atomic emission spectroscopy of the MHCD discharge was applied for the

molecules (CCl_2F_2 CHClF_2) that were introduced into the He plasma gas. The intensities were linear over 3 orders of magnitude. The detection limits for CCl_2F_2 are 20 ppb v/v using either Cl 912.114 nm or F 739.868 nm. Mass spectrometric measurements of the same analyte resulted in similar detection limits.

Concluding remarks

The experimental parameters like the dimensions of the discharge, the resulting volume, the pressure, the input power, the flow rate, the detected analyte, and the limit of detection are presented in figure 2.13 for the different plasmas discussed above. The mean power density and the exchange rate (ratio of the flow rate to the plasma volume) are calculated from the experimental data. An important parameter for the development of miniaturized plasma is the mean power density, which is calculated from the input power and the volume of each discharge. On the one hand, the mean power density must be high enough in order to dissociate and to excite molecules, while, on the other hand, it must not be too high in order to avoid damages by thermal stress. A comparison of the mean power densities of the two dc discharges shows that for molecular detection (dark shaded rows), a mean power density of 0.05 kW/cm^3 is sufficient to get a low limit of detection for hexane, whereas a mean power density of 12.5 kW/cm^3 is needed for atomic detection. The application of the RFP and the DBD shows excellent results according to the limit of detection, although the mean power density is less than 1 kW/cm^3 . In the case of the DBD, the excellent dissociation capability is explained by the relatively high peak power of about 1 kW/cm^3 , which will be discussed later. Therefore, a mean power density of 1 kW/cm^3 should be sufficient for atomic spectrometry, while using a much lower power density ([Jin01], [Eij99]) results in molecular detection. Some discharges (light shaded rows) are even suitable for liquid detection, if the sample is introduced by electrospray or if the water sample is used as cathode. In case of the latter, the power consumption can be sufficiently small, because the main process of sample evaporation is done by sputtering [Wil02], while, in the other case, an appropriate miniaturized sample introduction system and high power are obligatory.

In order to prevent damage to the plasma devices, they should be cooled as mentioned, for example, by Bass et al. (PP-CC μ P) [Bas01], who used a grounded copper block as the bottom electrode, or Bilgic et al. (MS-MIP) [Bil00], who connected the ground electrode to a copper socket with an active cooler. An alternative or additional possibility to prevent damage to the plasma device is to operate the plasma with a high flow rate. A measure for the quality of cooling by the gas flow is the exchange rate. The dependence of both parameters for the presented plasmas is plotted in figure 2.14.

plasma	reference	dimensions	volume [cm ³]	pressure	input power [W]	flow rate [ml/min]	mean power density [kW/cm ³]	exchange rate [s ⁻¹]	analyte/ methode of detection	limit of detection
DC	[Ei99]	2 0.45 0.2 mm ²	180 10 ⁻⁶	atmospheric	0.009	0.0192	0.05	2	Hexane (519 nm) emission	1 pg/s 800 ppb v/v
	[Bes02]	2 0.07 0.07 mm ³	10 10 ⁻⁶	atmospheric	0.125	0.9/R _{split} *= 0.018	12.5	30	Cl (479.5 nm) emission	800 pg/s
DC IMS	[Lon03]	0.01 0.01 0.02 mm ³	2 10 ⁻⁹	atmospheric	10 ⁻³ (500 V, μ A)		500			no analytical measurements
ELCAD	[Jen02]	0.15 0.3 1(?) mm ³	45 10 ⁻⁶	1.5 bar	5 (1 kV, 5 mA)	5 μ l/min (liquid)	111		Cu	no assignment
ELCAD	[Mar01]				80 (1 kV, 80 mA)	1 ml/min (liquid)			Hg	1 g/ml
ELCAD	[Wil02]	0.5 0.7 2.5 mm ³	0.88 10 ⁻³	atmospheric	1.25 (2.5 mA, 500 ? V)		1.1		Pb, Cr	5 ppm
CCP 20 kHz	[Guc04]	id: 0.15 mm length: 10 mm	0.7 10 ⁻³	atmospheric	8	100	11	2380	Hg, As, ..	200 ppb
PP	[Jin01]	1.5 1 1 mm ³	1.5 10 ⁻³	atmospheric	< 0.001	0.16	< 0.001	2	Methane	2.8 ng/ml
PP-CCuP 13.56 MHz	[Bas01]	0.25 0.25 5 mm ³	0.3 10 ⁻³	atmospheric	20	70	67	3888	OH, NH ⁺ , N ₂ , N ₂ ⁺ , He I emission	no analytical measurements
CCMP 13.56 MHz	[Yos01]	0.15 0.5 5 mm ³	0.375 10 ⁻³	73 hPa - atmospheric	5	475	13	2111	OH, various He I lines, emission	no analytical measurements
ICPjet	[Ich03]	1 1 30 mm ³	30 10 ⁻³	atmospheric	50	700	1.7	23333	Na (589 nm), emission	5 ppm
mICP 818 MHz	[Min02]	id: 3 mm length: 6 mm	42 10 ⁻³	7.4 hPa	3.5		20		SO ₂ , (S 463.5 nm) emission	190 ppb
MS-MIP 2.45 GHz	[Bro02]	0.9 1 20 mm ²	1.8 10 ⁻³	atmospheric	30	300	17	2777	Hg (253 nm) emission	50 pg/ml
RFP 350 kHz	[PB96]	id: 0.32 mm length: 35 mm	2.8 10 ⁻³	low pressure	2	25	0.7	149	Cl mass spectrometry	2.2 pg/s
DBD 5-20 kHz	this thesis	1 1 50 mm ³	50 10 ⁻³	10 – 100 hPa	< 1	50	0.01 1	16	CCl ₂ F ₂ Cl (637.8 nm), F (685.8 nm) absorption	400 ppt v/v for Cl and 2 ppb v/v for F
MSE	this thesis	id: 0.1 mm length: 0.2 mm	1.57 10 ⁻⁶	atmospheric	1.5	100	1000	1 10 ⁶	CCl ₂ F ₂ Cl (912.1 nm), F (739.9 nm) emission	20 ppb v/v for Cl and F

peak power density * suspected split ratio between FID and plasma chip of 50:1

Figure 2.13: Experimental data for different plasmas; dark shaded row: molecular detection, light shaded row: liquid samples.

It is obvious that plasmas operated with a high mean power density also have a high exchange rate; the values of nearly all plasmas are aligned along the bisecting line of the plot. In the lower part, molecular detection is obtained, while, in the higher power density range, atomic detection is achieved. (The DBD is marked twice in the plot because of the difference in mean and peak power density.) However, to reduce the sample and gas consumption, it is desirable to develop plasmas, which can be operated with low flow rates.

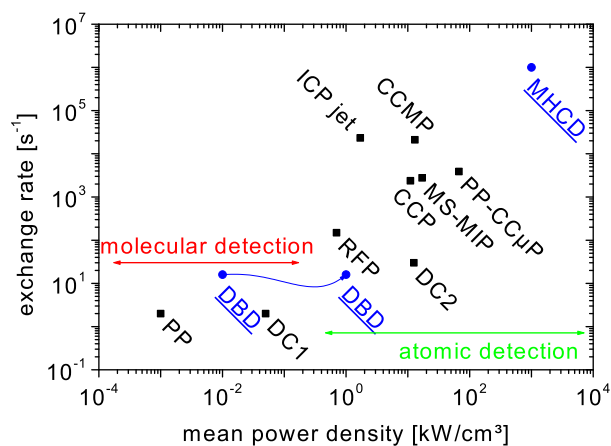


Figure 2.14: Exchange rate and mean power density for different plasmas; the blue discharges were investigated during this thesis.

2.3 Sample introduction in miniaturized discharges

One important property of analytical systems is the flexibility in analyzing gaseous, liquid and solid samples. All these samples have somehow to be introduced into the discharge. This is the main problem apart from the dissociation, excitation or ionization of the analyte. As discussed in the previous section, most miniaturized plasmas show good analytical results for gases. No reports are given about solid samples, and many difficulties are encountered when introducing liquid samples into the discharges. The impact of sample introduction into miniaturized discharges will be enlightened in this section.

Power balance in the presence of analyte samples

When introducing a sample into the plasma, some of the input power will be used to heat and dissociate the analyte. This energy is not available for sustaining the discharge anymore and, therefore, the injected volume should be low. For dissociation, the bonding energy of the elements has to be delivered by the plasma. For covalent bondings, this value is in the range of 300 – 1000 kJ/mol, depending on the atoms concerned and the valency of the bond. Assuming a molecule with a maximum of 10 bonds, up to 10 MJ/mol have to be raised. The amount of the highest sample concentration with analytical relevance is commonly in the range of $\mu\text{g/s}$, equivalent to a maximum of nmol/s. Therefore, the complete dissociation of a high sample amount would consume 10 mW. This power can easily be delivered in classical ICPs or MIPs, but as was shown, miniaturized discharges

are sustained with powers in this range. The introduction of large sample volumes will lead to non-linear calibration curves, because the energy for dissociation cannot be delivered by the discharge. Furthermore, no complete dissociation will be achieved in small-scaled discharges, but equivalent dissociation for different molecules should be aimed at.

By introducing a liquid or damp sample, commonly an aerosol, some of the input power has to be used, additionally, to vaporize and dissociate the liquid. The loss of this energy might even lead to a localized quenching of the plasma, because the concentration of the solvent will be higher by several orders of magnitude than the analyte itself. In the ICP, local cooling occurs in a 1 – 2 mm sphere around incompletely desolvated droplets, which deteriorates vaporization and ionization efficiency, thereby causing signal suppression [Ole89].

For example, the energy consumed by water is composed by the heating from room temperature to the boiling point, the evaporation enthalpy, the heating of the vapors to the gas temperature of the discharge and the dissociation enthalpy:

$$E = m(c_p^{liquid} \Delta T_1 + c_p^{gas} \Delta T_2 + q_v + q_{diss})(2.7)$$

$c_p^{liquid, gas}$	heat capacity
$\Delta T_{1,2}$	difference between water and gas temperature
$q_{v, diss}$	enthalpy of evaporation, dissociation

The specific values for the capacities and enthalpies mentioned above are enlisted in table 2.3.

c_p^{liquid}	c_p^{gas}	q_v	q_{diss}
4.2 J/gK	2 J/gK	2.2 kJ/g	45 kJ/g

Table 2.3: Important data for water.

For example, assuming a water temperature of 300 K and a gas temperature of the plasma of 500 K, a power of 5 and 14 mW, respectively, is used to heat 1 μ l/min water. Additionally, 40 mW are required for complete evaporation and 750 mW for complete dissociation.

This sums up to almost 0.8 W which would be the whole power coupled into microplasmas, or even more. However, taking into account that complete dissociation is never achieved, a power of 100 mW is sufficient for 10 % dissociation. Therefore, in order to introduce liquid samples into miniaturized discharges, only low sample flows can be used. Furthermore, the introduction most probably has to be assisted as will be shown. However, introducing small liquid flows results in small analyte amounts. Assuming concentrations as high as several hundred ppm analyte in the solvent with a flow of 1 μ l/min, the sample amount entering the plasma would be some ng/s. This value is close to the

general detection limit, which means that introducing even smaller amounts to prevent the plasma from being purged, results in non-detectable concentrations. Furthermore, this assumes that the whole sample amount enters the discharge, which is problematic, as illustrated below.

Injection methods for liquid samples

Suitable methods for liquid sample injection into microplasmas will have to be developed in order to establish a portable liquid sample analysis system and it is investigated by several research groups. For example, in the case of conventional ICP-OES systems, pneumatic or ultrasonic nebulizers are usually adopted for atomizing sample solutions. The introduction of aerosols derived from aqueous solutions was found to be impossible with the small-sized plasma sources [Guc03]. The reason for this might be the quenching due to the energy that is consumed for the evaporation of the water droplets, or the evaporating water leads to a drastic expansion of the plasma volume, which is constrained by the discharge walls. Furthermore, the hot plasma has a high viscosity and resists the introduction of a cold sample. In conventional ICP systems, this effect is worked out by the application of an outer formed shielding gas around the sample introduction flow. Nevertheless, this method is not appropriate for small-sized discharges because the gas consumption is increased unintentionally.

Other possible injection methods are the thermospray and electrospray. In a thermospray, the sample is pumped through a heated capillary. When the solution reaches the hot zone, it is vaporized almost instantaneously and leaves the tube as a spray of very small droplets. In contrary to pneumatic nebulizers, this system already couples some power for the evaporation of the analyte into the system. Nevertheless, since the viscosity of high temperature plasmas is high, sample injection just by the gas flow of a pneumatic nebulizer seems to be quite difficult. In contrast, an injection assisted by a strong electrostatic force is effective. Therefore, an electrospray can be used in which the flowing liquid sample is electrosprayed from a sharp pointed tip biased at 1 – 5 kV with respect to the sampling orifice of the mass spectrometer. Nonetheless, each advantage has a drawback; applying a voltage of several kV for the electrospray to small size discharges operating at voltages of several hundreds of Volt will result in further plasmas between the ground and the electro-tip of the spray. Thus, this method is probably only successful in combination with high frequency discharges, like it was presented by Ichiki et al. [Ich03].

Another possibility for the detection of metallic species in a liquid sample is hydride generation. In this method, the sample is mixed with HCl and sodium borohydride, and

a volatile hydride is formed, which can be separated from the liquid phase. This helps to avoid contamination of the discharge with water and is commonly used in atomic absorption spectroscopy. The successful use of this method for miniaturized discharges was recently presented by [Guc03].

Consequences of analytical detection for miniaturized discharge

According to the considerations mentioned above, miniaturized discharges will always suffer from a smaller dynamic range than found for conventional sources. The reason is that high sample amounts cannot be introduced into the plasmas because the low power is not sufficient, while the detection limit will not be lower than for conventional discharges. Furthermore, microplasmas are less robust against the load of damp samples, due to the high power consumed for evaporation and dissociation. Additionally, the plasma resists the introduction of samples, so the injection is difficult. Other problems might occur if organic compounds will be analyzed with small-scaled devices. In this case, the carbon resulting from the decomposition of the analytes will deposit on the discharge wall, reducing the already small diameter of the chamber. This problem will also appear, if solid samples are analyzed by laser ablation, for example. The ablated material, which does not only consist of ions and atoms, but also of clusters, will clog the whole device. Nevertheless, miniaturized discharges, as they will be presented in the following chapters, are encouraging devices for the analysis of gaseous samples, but should not be regarded as all-rounders. They have to be adapted to one special problem and can replace larger devices in few cases, due to their advantage of low power and sample consumption as well as the small dimensions.

Instrumental techniques

The detection of molecular species in miniaturized discharges by atomic spectrometry demands the use of specific methods and instrumentations adapted to small size devices. The general scheme of element selective detection is presented in figure 3.1. As can be seen, different steps are required in the experiment. The first step is the preparation and introduction of the sample into the analytical apparatus. It is followed by the separation of the different species by an appropriate chromatographic or electrophoretic technique. Subsequently, the separated molecules have to be atomized before they can be measured by absorption, emission, or mass spectrometry. In the following elaboration, the atomizer will be one of the presented miniaturized discharges. It has to be noted that such schemes are well established in analytical chemistry, especially with atomic emission detectors (atomic emission spectrometry applying plasmas – AES) and inductively coupled plasma-mass spectrometry (ICP-MS).

Furthermore, the properties of the miniaturized discharges have to be determined in order to obtain information about the capability of excitation, ionization, and dissociation of the molecular species. It would be advantageous to be able to measure the plasma parameters like gas temperature, electron density, electron temperature, and the density of excited species.

In this way, a comparison to the classical plasma sources can be made, and the new sources can be classified. The most appropriate method, covering both analytical and parametrical tasks is optical spectrometry because it is non-invasive and very sensitive. In this work, diode laser atomic absorption, emission and mass spectrometry were used for the evaluation of the plasma parameters as well as for the detection of molecular species. They also fit very well into the diagnostics of small-sized discharges. It has to be mentioned that fluorescence spectroscopy

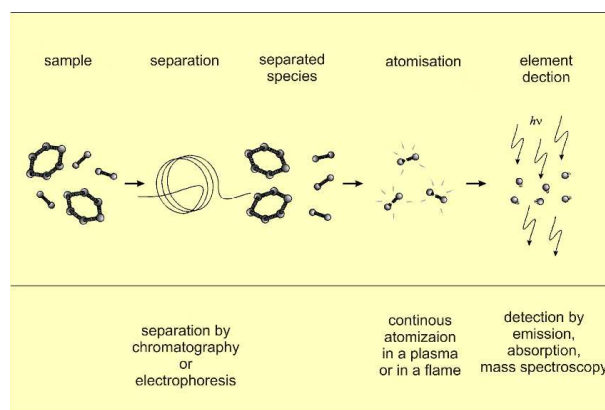


Figure 3.1: Principal detection scheme of molecular species by atomic spectrometry [Koc98].

would also be very sensitive, and sampling a small volume, but several problems occur. First, a high background emission of the plasma sources reduces the possibility to reach a good detection limit. Second, the light scattering is a major difficulty which can only be compensated by complex arrangements.

Each of the methods used in this thesis will be described shortly in the following sections together with some sensitive detection schemes that are capable of increasing the sensitivity of the method and, thus, the detection of the species.

3.1 Absorption spectroscopy

A classical atomic absorption spectroscopy (AAS) assembly for quantitative analysis consists of a hollow cathode lamp, whose radiation is directed through the absorption volume and further detected by a photo-detector. Here, laser diodes are used as radiation sources. They deliver very narrow lines and can be tuned in comparison with hollow cathode lamps. The tuning capability is e.g. necessary for line profile analysis.

Light sources, Laser diodes

The laser spectroscopy, in particular with laser diodes, offers a lot of advantages compared to classical AAS. The radiation of the laser beam is monochromatic and can be tuned over a specific wavelength range avoiding the use of dispersive elements. The spectral resolution is only limited by the width of the absorption line itself, because the linewidth of the laser diode is much smaller than that of atomic transitions. Furthermore, the absorption path can be increased by multi-reflection, because the laser diode radiation owns a marginal divergence.

The laser diodes used in diode laser atomic absorption spectroscopy (DLAAS) are commercial, etalon type devices of different producers. The heart of the laser diode is the p and n doped semiconductor that acts as an active medium. Photons are generated by the recombination of holes of the p -zone and electrons of the n -zone of the chip, whereas the surfaces of the crystal serve as mirrors for the laser resonator. Due to the high electron density in the conduction band, a reflectivity of 30 % is sufficient for the lasing threshold. The inset of a laser diode is presented in figure 3.2. The crystal itself is situated on a metallic block and is less than one millimeter large. The connection is made by tiny wires of less than 50 μm in diameter. As can be seen, the size of the semiconductor is small which makes DLAAS preferable for miniaturized systems.

Laser diodes can be operated in a free running mode without external optical stabilization emitting light in the region of 625 – 1600 nm. Recently, also laser diodes in the blue region (375 – 445 nm) became available. Individual laser diodes can be typically tuned over 10 – 20 nm by temperature ($-20\text{ }^{\circ}\text{C} - 50\text{ }^{\circ}\text{C}$) and current, depending on the type. The mode-hop free range is restricted to several hundred picometers. Wavelength tuning by tempera-

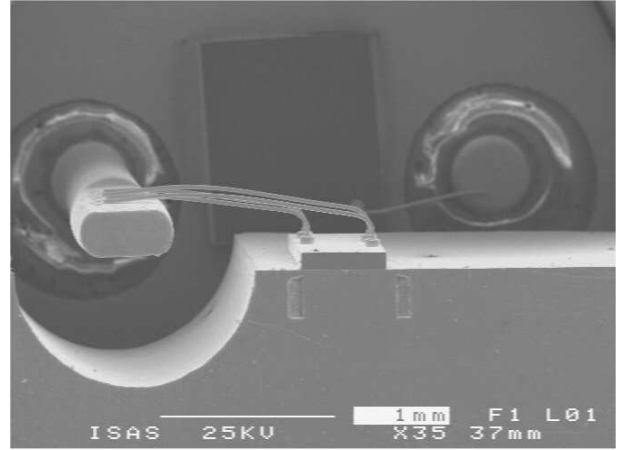


Figure 3.2: Picture of laser diode taken with SEM.

ture is a slow process, while current tuning can be very fast. Wavelength modulation frequencies up to 500 kHz can be achieved easily [Fra93]. All etalon type laser diodes show mode hops and, therefore, mostly wavelength gaps which cannot be covered in a free running mode. This problem can be overcome by the use of external cavities in which a grating reflects the first diffraction order of the laser light back into the diode. In this case, an external resonator is built. Therefore, the mode hop free tuning range is limited to about 50 GHz, but all wavelengths in the gain profile can be obtained.

Furthermore, a very simple but effective feedback method is the mounting of a glass plate in front of the diode laser chip [Zyb97]. The wavelength range of laser diodes can be extended by second harmonic generation (SHG) using non-linear phase-matched or periodically poled crystals, whereby powers up to about 1 mW can be achieved in the 335 – 430 nm region, depending on the initial laser power and the crystal material applied.

Due to the fact that the wavelength range of laser diodes is still very limited, the number of elements that can be measured in absorption is restricted. Only a few strong optical transitions from the ground state of (mainly metallic) elements are in the specific wavelength windows delivered by laser diodes. Therefore, transitions from excited levels have to be used for the detection of atoms. In particular, transitions from metastable levels which are well populated, e.g. in low-pressure discharges, can be used successfully. All elements measured during the practical work are enlisted in table 3.1 in addition to the laser diodes used. The absorption line always starts from excited states; metastable and resonance levels are marked.

Absorption technique

In an absorption measurement, monochromatic light with the wavelength λ is directed through an absorbing layer. The absorption coefficient of the line is α . The transmitted

element	wavelength	laser diode	mode
Cl (met)	837.824 nm	<i>Hitachi</i> HL8325G	fr
F (met)	685.792 nm	<i>Mitsubishi</i> ML1012R-01	fr
S (met)	921.539 nm	<i>Toptica company</i>	ec
I (met)	906.081 nm	<i>Toptica company</i>	ec
Br (met)	827.472 nm	<i>Hitachi</i> HL8325G	fr
He (res)	667.999 nm	<i>Hitachi</i> HL6714G	ec
He (met)	388.975 nm	<i>Hitachi</i> HL7851G	ec, fd
Ar (met)	772.633 nm	<i>Sharp</i> LT027MDO	fr
(res)	800.838 nm	<i>Sharp</i> LT016MDO	fr
		<i>RLT</i> 80010MG	ec
(met)	801.699 nm	<i>Sharp</i> LTO16MDO	fr
		<i>RLT</i> 80010MG	ec
(met)	811.755 nm	<i>Toptica company</i>	ec
(res)	826.680 nm	<i>Hitachi</i> HL8325G	fr

Table 3.1: Laser diodes used in the present work. (met: metastable initial level, res: resonance initial level; fr: free running, ec: external cavity, fd: frequency doubled)

intensity I_T is given by the Beer-Lambert law

$$I_T(\lambda) = I_o(\lambda) \cdot e^{-\alpha(\lambda) \cdot L}, \quad (3.1)$$

with I_o as the intensity of the incident light and L as the absorption length. The absorption coefficient $\alpha(\lambda)$ is given by the difference of absorption and induced emission rate of the transition:

$$\alpha(\lambda) = (N_k - \frac{g_k}{g_i} N_i) \sigma(\lambda). \quad (3.2)$$

$N_{k,i}$	density in lower and upper level
σ	absorption cross section
g_k, g_i	statistical weights of the levels

As low power laser radiation is used, the term of induced emission can be neglected. The absorption cross section itself can be linked to the Einstein coefficient of absorption B_{ki}

$$B_{ki} = \frac{c}{h\lambda} \int \sigma(\lambda) d\lambda. \quad (3.3)$$

c	speed of light
h	Planck's constant

Principally, the integral has to be calculated for all wavelengths from 0 to ∞ , but only the dominant term within the line profile $I(\lambda)$ contributes, so the calculation can be restricted to several tens of pm. The Einstein coefficient of absorption B_{ki} is connected to the Einstein coefficient of spontaneous emission A_{ik} by

$$B_{ki} = A_{ik} \frac{\lambda^3}{8\pi h} \cdot \frac{g_i}{g_k}. \quad (3.4)$$

The Einstein coefficients A_{ik} are tabulated in [Kur96], for example.

Knowing the line profile of an absorption line, the density N_k of atoms in the lower level can be determined. It is given by

$$N = \frac{8\pi g_k c}{\lambda^4 g_i A_{ik}} \frac{1}{L} \int \alpha(\lambda) d\lambda. \quad (3.5)$$

c	speed of light
$g_{k,i}$	statistical weights
A_{ik}	Einstein coefficient
L	absorption length

Improvement of signal to noise ratio in absorption by use of modulation

Commonly, the absorption technique does not offer a good detection limit. In principle, absorption of less than 0.1 % cannot be detected. In order to suppress various noise sources and to discriminate non-specific background signals, different detection techniques applying modulation of the light intensity, the absorption, and of the diode laser wavelength, as well as a double beam method, have been developed. One effective technique for baseline reduction in diode laser spectroscopy is wavelength modulation with detection at the second harmonic of the modulation frequency [Rei78, Zyb95]. Unfortunately, wavelength modulation of a laser diode is, as a rule, accompanied by residual amplitude modulation (RAM). This leads to a background signal at the registration frequency $2f$, which is much smaller than the background signal in the case of $1f$ detection, but retains the multiplicative noise structure. Because this background signal is proportional to the laser power and the optical transmittance, the low-frequency noise of the laser radiation at the detector is mixed with the modulation frequency and included in the detection bandwidth. The background signal can be eliminated if, additionally, the absorption is modulated and detection is performed at the difference or sum of the wavelength and absorption modulation frequencies [Zyb95]. If this is the case, it is possible to achieve detection limits only determined by the laser excess noise, because the background signal is absent. The most successful detection technique is the so-called double-beam double-modulation procedure [Lig97, Koc02], which can eliminate the laser excess noise by applying a double-beam arrangement. In this case, the beam of a laser diode is split into two parts, where one beam is detected by a photodetector directly, while the other one is absorbed in any medium (e.g. low-pressure discharge, flame) before detection. Both the absorption and the wavelength of the laser diode are modulated with different frequencies. The signals of both photodetectors which are logarithmically subtracted are preamplified, and detected on a mixed frequency with a lock-in amplifier. The signal S in the double-beam double-modulation technique is given by

$$S(L, t) \propto \ln \frac{I_S}{I_R} \quad (3.6)$$

$$= \ln \frac{a_S}{a_R} + \ln \frac{T_S}{T_R} - \alpha(\nu, t)L. \quad (3.7)$$

a_S/a_R	absorption and reference beam splitting ratio
$T_{S,R}$	transmittances
$\alpha(\nu, t)$	absorption coefficient
L	absorption length

The registered signal is proportional to the absorption coefficient αL , implying that the signal is independent of the applied laser power unless the considered transition is saturated. According to the intentionally accepted 3σ criterion,¹ the theoretical detection limit (DL) is three times the shot noise given by

$$DL = 3 \cdot \sqrt{(2e^2\eta\Delta\omega Ph\nu)}. \quad (3.8)$$

e	elementary charge
η	quantum efficiency of the photodetector
h	Planck's constant
$\Delta\omega$	detection bandwidth
P	laser power
ν	laser frequency

In this way, using a laser diode with 100 nW power (typical for single pass SHG in non-linear crystals), an experimental absorption of 10^{-4} AU (absorption units) can be reached, while the theoretical shot noise limit is 10^{-5} AU. This result is already one order of magnitude better than the typical 10^{-3} AU which is achieved with the well-known hollow cathode lamp AAS. Increasing the laser power even higher to 2 mW, absorptions down to $2 \cdot 10^{-7}$ AU have been measured [Lig97].

Throughout this work, the use of wavelength modulation was avoided and only absorption modulation (by plasma modulation) was used. The experiments show that, investigating small-sized discharges, interferences at windows and walls are becoming dominant which would be forced, additionally, by wavelength modulation. These interferences imply a higher background and noise which diminishes the performance. The use of plasma modulation for the determination of the absolute density of excited states entails one problem, because the lock-in amplifier delivers at the output the signal of the first or second component of a Fourier transform. However, the absorption signal is never a well-defined periodical sine. This makes the lock-in detection for plasma diagnostics difficult, and correlations have to be made between the direct and the modulated signal. Therefore, as far as it was possible, only direct signals were used for the determination of excited atom density as a Fourier transform could be avoided.

¹The detection limit according to the definition of IUPAC (International Union of Pure and Applied Chemistry) is given when the net signal equals 3 times the standard deviation of the limiting noise.

3.2 Emission spectroscopy

The analytical method of DLAAS mentioned above offers a very good detection limit, but it has the disadvantage to be restricted to one element as long as it is not used with a module of several laser diodes [Gro93].

Emission spectrometry has the benefit of covering several elements in case of using a spectrometer with a large wavelength range. A classical spectrometer consists of an inlet slit, a dispersive element (prism, grating) and an array formed detector (diode arrays, CCD row). In this case the wavelength is separated just in one dimension. However, due to the limited size of the detector and the number of pixels of the CCD, either a small wavelength range can be observed with high resolution or a large one with small resolution.

The idea of an echelle spectrometer is the separation of the wavelength in two dimensions in order to cover a large wavelength range with a high spectral resolution at the same time [BR97]. The spectrum is first dispersed into one row of small wavelength ranges and then separated perpendicularly in order to obtain a quadratic matrix. This can be achieved by the combination of a grating with a low number of grooves/mm and a second dispersive element like another grating or prism.

An echelle grating is presented on the left hand side of figure 3.3, where N is the grating normal, d the grating constant, α the incident angle, β the diffracted angle and θ_B the blaze angle. The relation between the incident and diffracted light is given by

$$k\lambda = d(\sin \alpha + \sin \beta).$$

(3.9)

	k	number of diffraction order
	λ	wavelength

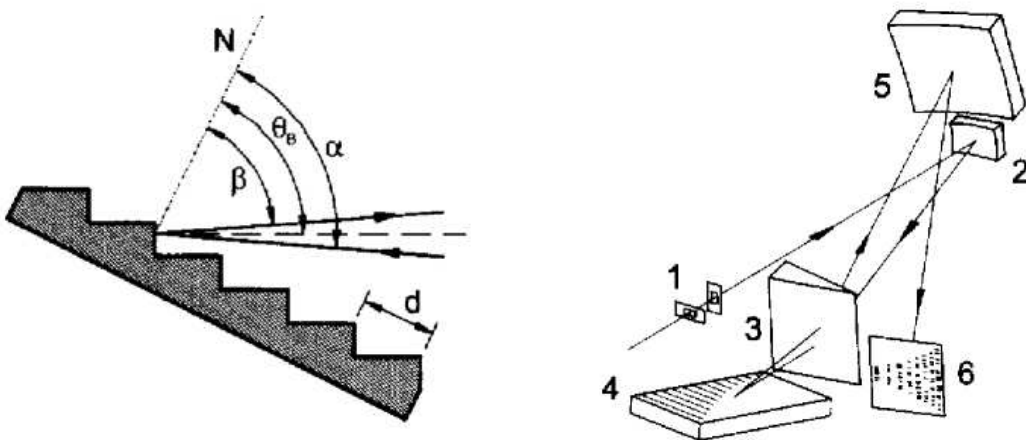


Figure 3.3: Echelle grating and configuration of an echelle spectrometer taken from [BR97].

Several combinations for k and λ are possible for a given diffracted angle. The characteristic of the grating of an echelle spectrograph is the large blaze angle; the incident beam is almost reflected and diffracted perpendicularly. The echelle grating creates a small stripe in which several orders of different wavelengths are superposed. A second dispersive element, in this case a prism, separates the light in a second dimension.

The principle arrangement of an echelle spectrometer is presented in the right hand side of figure 3.3. Here, (1) refers to the entrance slit, (2) to the spherical collimator mirror, (3) to the prism, (4) to the echelle grating, (5) to the spherical camera mirror, and (6) to the plane of the echelle spectrum in which the CCD camera is mounted. By using the diffraction of the prism twice, the resolution can be increased further. The device used in this thesis was developed and built at ISAS Berlin for the near IR spectral range and covers the wavelength range of 650 – 950 nm. This spectrometer is already small-scaled in comparison with classical spectrometers due to the complex arrangement shown in figure 3.3.

3.3 Line profile measurements

The knowledge of different plasma parameters, like gas temperature and electron density, can be improved by line profile measurements, either in absorption or emission, because there is a correlation between these parameters and the widths or shifts of the line profiles. In this context, linewidth and lineshift are defined as full-width at half-height and the displacement of the maximum signal with the wavelength, respectively. All transitions have a natural linewidth determined by the limited lifetime of the level involved, but this one is much smaller compared to other broadening mechanisms. The three fundamental broadening processes in a discharge are Doppler-, pressure- and Stark-broadening.

In this regard, homogeneous and inhomogeneous broadening can be distinguished. While the first one is equal for all atoms, the latter one is only generated by an ensemble of atoms. Natural broadening as well as pressure and Stark-broadening generate homogenous line profiles that can be expressed as a so-called Lorentzian profile:

$$y_{Lorentz}(\lambda) = \frac{2A}{\pi} \frac{2}{4(\lambda - \lambda_o - \beta)^2 + w^2}. \quad (3.10)$$

A	Area below the curve
λ_o	line centre
β	shift of line maximum
w	full width at half height

The Doppler-broadening is inhomogeneous and can be described by the Gaussian profile:

$$y_{Gauss}(\lambda) = \frac{A}{w\sqrt{\pi/2}} \cdot e^{-2\frac{\lambda-\lambda_o}{w^2}}. \quad (3.11)$$

If both kinds of broadening mechanisms occur, the two profiles are folded and a so-called Voigt profile is obtained:

$$y_{Voigt}(\lambda) = A \frac{2 \ln 2}{\pi^{3/2}} \frac{w_l}{w_g} \int_{-\infty}^{\infty} \frac{e^{-t^2}}{\ln 2 \cdot \left(\frac{w_l}{w_g}\right)^2 + \left(\sqrt{4 \ln \frac{\lambda - \lambda_0}{w_g}} - t\right)^2} dt \quad (3.12)$$

The new full-width at half-height w_v can be calculated knowing the Lorentzian width w_l and Gaussian width w_g [Dra66]

$$w_v = \sqrt{w_g^2 + w_l^2/4} + w_l/2, \quad (3.13)$$

whereas the Lorentzian width is composed additive by the other two Lorentzian widths $\Delta\lambda_{Stark}$ and $\Delta\lambda_{pressure}$.

Along with line broadening, a shift of the absorption or emission line is present. This shift has a similar origin as the broadening: pressure and Stark shift due to the interaction of the particles and Doppler shift owing to a directed velocity of the atoms investigated. Nevertheless, the detailed physical processes for the shifts mentioned differ. Details on the evaluation of line shifts and widths will be given in the corresponding chapters.

3.4 Mass spectrometry

Mass spectrometry is a highly sensitive technique for the detection of atomic and molecular species, but it is difficult to apply it for fundamental investigations of plasma parameters. It can monitor several masses simultaneously and even separate the different isotopes. The quadrupole mass spectrometer used in this work consists of a Balzers QMA 400 and a homebuilt ion lens system. The micro hollow cathode discharge was coupled with the setup in order to measure positive ions (see section 5.3).

The function of the ion lenses is to focus the charged particles of the ion source in order to reach the detector, but also to filter neutral particles and photons which are forced to collide with the wall. Therefore, they do not reach the detector. The system of the ion lenses is shown in figure 3.4. It is composed of 5 circular shaped steel discs with bores in the middle. The discs are electrically isolated from each other and a specific potential is applied to each lens. A combination of an accelerating, focusing force (negative potential), and a slowing down, defocusing force



Figure 3.4: Picture of ion lens system.

(positive potential) has to be chosen carefully. The separation of charged and neutral particles is obtained by the first ion lens (uppermost one) which is built by a holey cup and a small plate in the axis. Neutral particles will bounce onto the plate, while charged ones pass it, following the electrical field around it. The optimal parameters for the five ion lens voltages can either be found by numerical simulation of the potential or by trial and error. Due to the fact that initial conditions have to be chosen carefully for the simulation, which implies a good knowledge of the ion energy distributions, the experimental determination of the voltages was done.

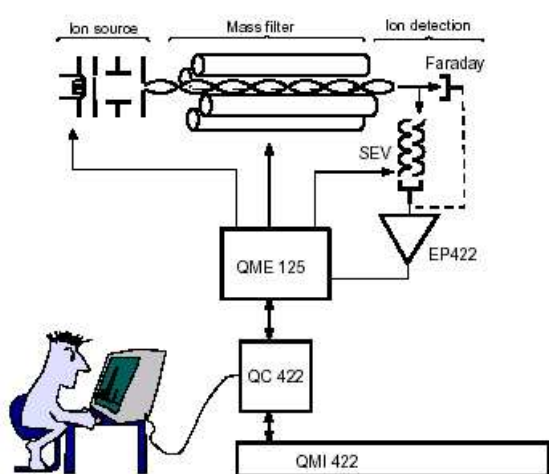


Figure 3.5: Principle of Balzers Quadrupole [Bal].

In this way, the 2-dimensional electrostatic quadrupole field forms a saddle-shaped potential. A charged atom or molecule entering the field is confined in one direction, but unconstrained in the transverse direction. In order to stabilize the particles in both directions one simply has to rotate the saddle as the particle starts to leave the saddle point. This is obtained by a rf potential that rotates the effective field. A special mass/charge ratio can be selected by the frequency of rotation and the curvature of the saddle (given by the geometry) which then oscillates around the center. Therefore, the rods are applied with a potential of $U + V \cos(\omega t)$, where U is a dc voltage and $V \cos(\omega t)$ is an ac voltage. The ac voltage determines the mass/charge ratio which can pass the filter and the resolution results from the dc voltage. This means that the resolution of the mass filter can be adapted to a specific need quite fast, by changing the amplitude of the voltages only.

The quadrupole analyzer does not actually separate ions like the time-of-flight (TOF) or a sector field mass analyzer, but filters out the ions required from all ions injected. Other ions collide with the analyzer rods and are lost, only the selected ions can pass through the

The arrangement of the Balzers quadrupole is given in figure 3.5. Ions are focussed and directed to enter the mass filter, they follow some trajectories in the low-pressure chamber and are detected either by a secondary electron multiplier or a Faraday cup. The mass filter consists of four rods made of molybdenum, each 200 mm long and 8 mm in diameter. Seen end-on, the rods are placed at the corners of a square, and are electrically connected kitty-corner. Taking a time cut, two rods are applied with a positive voltage, while the others are negative.

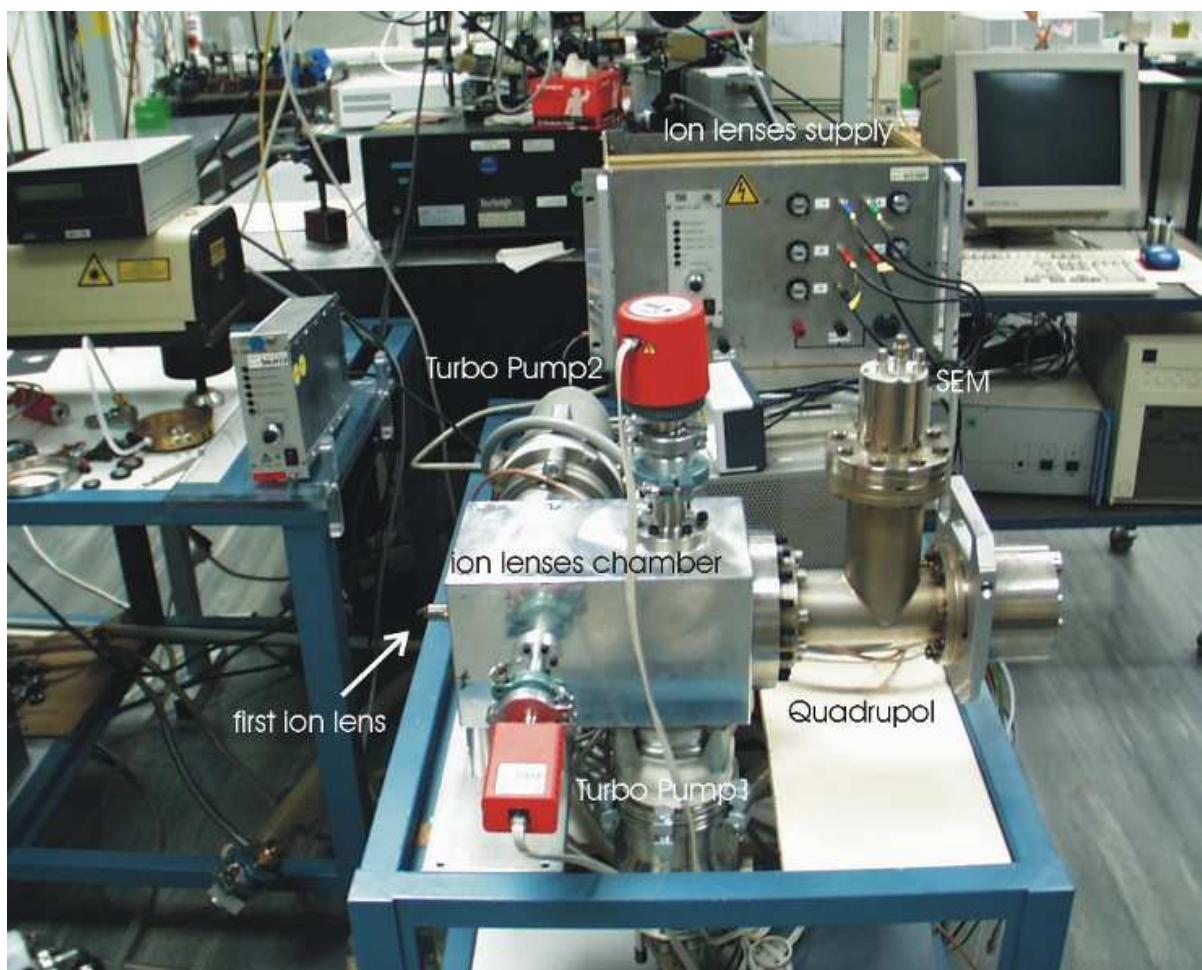


Figure 3.6: Photo of the Quadrupole setup.

filter successfully. A mass spectrum is obtained by monitoring the ions passing through the quadrupole filter as the voltages on the rods are varied. There are two methods: varying ω , and holding U and V constant, or varying U and V (U/V fixed) for a constant ω . The Balzers quadrupole uses the variation of the amplitude due to technical reasons, as do most analyzers. The rf-generator generates a voltage with a fixed frequency of 2.25 MHz. The measurable mass range is up to $m/q = 511$ with a resolution of $m/\Delta m = 1000$.

The ion current is detected with a secondary electron multiplier which is orientated transversally to the quadrupole. Therefore, the ions have to be deflected by an additional voltage which is another filter for neutrals and photons. The secondary electron multiplier consists of a series of biased dynodes that emit secondary electrons, when they are struck by an ion. In this way, the ion current is multiplied manifold by $10^4 - 10^8$. Furthermore, the signal is preamplified and different detection ranges, changing in orders of magnitude, can be obtained. Unfortunately, the dynamic range is strongly limited, so

only highly different signals can only be measured sequentially with varying pre-amplifiers. The complete arrangement of the mass spectrometer is illustrated in the right hand side of figure 3.6. The first ion lens is protruding out on the left hand side, while the others are situated in the aluminum housing. The quadrupole analyzer is adapted on the right hand. The secondary electron multiplier is situated on the upper part. The pressure in the system has to be $10^{-5} - 10^{-7}$ mbar in order to obtain a good mass filter and detection with the SEM. This low-pressure is reached by two pressure stages, one behind the skimmer and one in the middle of the ion lens chamber, with two turbo molecular pumps (Leybold TW150, 150 l/s).

The quadrupole could be controlled either by the Balzers control unit or with a self-written Q-BASIC program on a personal computer. The potentials of the five ion lenses were applied by a high voltage generator using five variable resistances connected parallel.

Perspective of miniaturization

Commonly, mass spectrometers like the sector field mass spectrometer are supposed to be huge devices,. However, the ion traps, which are well known already, show that the research in miniaturization of these devices is growing. A recent review of Badman and Cooks [Bad00] deals with miniaturized mass analyzers. Downscaling in this case means developing analyzers that are significantly smaller, like hand-portable devices or even real micro-mass spectrometers that could be implemented on a chip. The principles of these micro mass-filters are as different as for the current laboratory-size devices: time-of-flight, linear quadrupole, quadrupole ion trap etc.

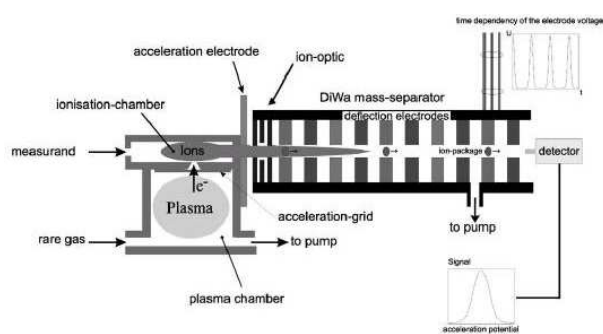


Figure 3.7: Principle of the miniaturized mass spectrometer of Siebert et al. [Sie98].

The ion optics consist of an extraction electrode and one focusing lens. The detector has a resolution at 40 u of $m/\Delta m = 20$.

A complete miniaturized mass spectrometer has been developed by Siebert et al. [Sie98]. The principle is shown in figure 3.7. The whole size of the separation length is a few millimeters, while the ionization chamber and ion lenses are hundreds of micrometers. A microwave discharge generates the electrons which are extracted from the chamber by some grids, and, consequently, ionize the gas in the so-

4.1 Generalities about dielectric barrier discharges

The idea to use miniaturized plasmas in analytical spectrometry implies finding discharges that fulfill conditions like high electron density, high gas temperatures, less interaction between analytes and electrodes, robustness, and reproducibility. The dielectric barrier discharge is one of the discharges which are already miniaturized in some other applications presented below, and fulfills some of the requirements. Many studies are already reported about this type of plasma, but there are still open questions. To some of them, answers will be given in this work performing plasma diagnostics. Furthermore, the application in analytical spectrometry will be characterized. This chapter shortly describes the principle of the dielectric barrier discharge and the applications that are realized up to now. Interestingly, even though the discharge is 150 years old, new projects can still be developed.

4.1.1 Principle of dielectric barrier discharge

The dielectric barrier discharge, which is also called silent discharge, was invented 1857 by Werner von Siemens (figure 4.1) for the generation of ozone and, for a long time, this was the main application. The special feature of this discharge was that the electrodes were placed outside the gas volume and were not in contact with the plasma. Siemens' initial arrangement is shown in figure 4.1. The discharge is operated in a cylindrical gas chamber. The gas in- and outlet are on the left and lower side, respectively. The electrodes are attached as silver paper in the inside and outside of the cylinder.

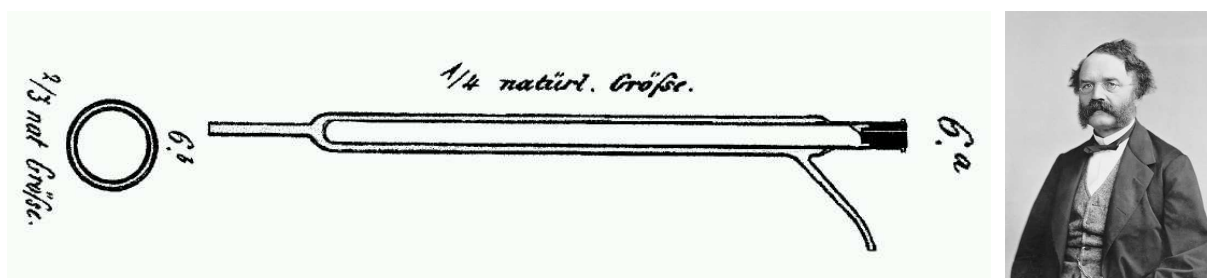


Figure 4.1: Historic ozone discharge tube, 1857 [Sie57] (natürl. Größe means natural size) and Werner von Siemens 1872 [Sie03].

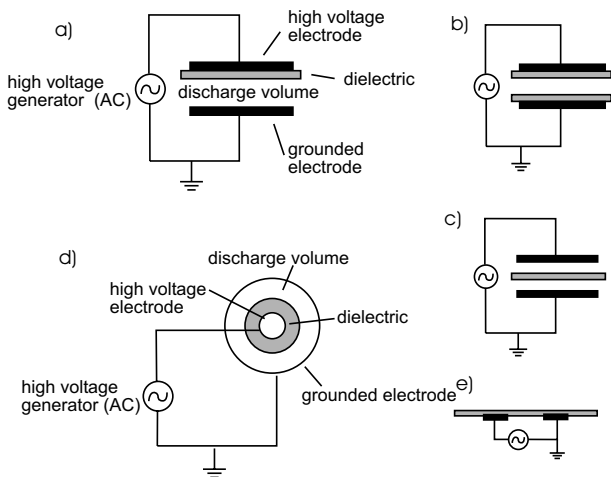


Figure 4.2: Different configurations of DBDs.

During the last 150 years, the discharge was developed and used mainly for the generation of ozone, but also for surface treatment, generation of excimer radiation, in plasma display panels, and waste gas treatment. All configurations of these applications have at least one dielectric placed in between two high voltage electrodes. Different configurations are presented in figure 4.2. Three planar arrangements are conceivable in which the two electrodes are parallel to each other, the dielectric being on one (a) or on both (b) electrode surfaces or in the middle between the electrodes (c). Furthermore, the electrodes can be formed like a cylinder having one electrode inside the other, with a dielectric film on the inner side (d). Another possibility is the design with both electrodes on the same plane (coplanar geometry), while the plasma is burning like an arc above (e).

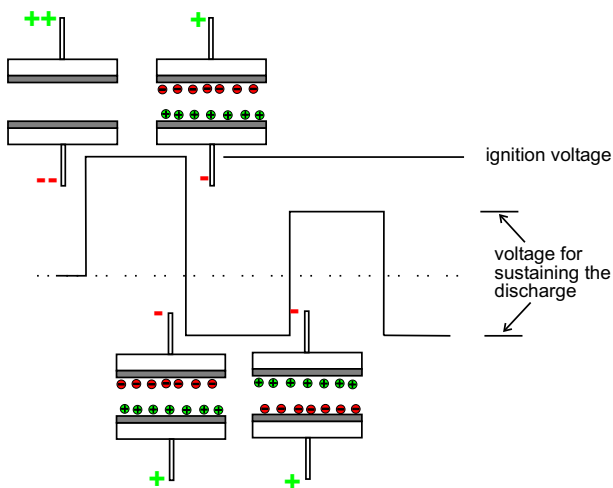


Figure 4.3: Principle function of DBD.

An alternating voltage in the range from a few Hz up to hundreds of kHz and an amplitude of several hundreds of volts to few kVs is applied to sustain the plasma. The breakdown mechanism is presented in figure 4.3. First, a high ignition voltage for the ionization of the gas is needed, then the dielectrics are charged positively and negatively, decreasing the gas voltage to such an extent that the plasma extinguishes. When the polarity of the voltage is reversed, the applied voltage and the memory voltage due to the polarization of the dielectric are added, and the discharge ignites again. Therefore, the sustaining voltage for the plasma is obviously lower than the ignition voltage. Furthermore, the plasma is purged again automatically as a result of the charged dielectric. In comparison with other electrodeless discharges operating at high frequencies, the dielectric barrier discharge presents the advantage of memory voltage formation by charge accumulation on the dielectric layer. The

memory voltage decreases the breakdown voltage and increases the gas voltage, respectively. At much higher frequencies, specific for MIP, ICP and CCP plasmas, this effect vanishes and, usually, these discharges require voltages of a significantly higher amplitude. Glasses, quartz and ceramics are used as dielectrics, having dielectric constants ϵ_r of typically 1.5 to 3000. The distance between the electrodes varies between several hundreds of micrometers and a few centimeters. The plasma gas consists of either pure noble gases, mixtures of noble gases with halogens or air (N_2 , O_2 , N_2/O_2).

4.1.2 Applications of dielectric barrier discharges

A recent review deals with the main applications of the dielectric barrier discharges which are either already industrialized or still under development by several research groups [Kog03]. A short overview of the main purposes is given in the following passage.

Ozone generation The earliest and still the most common application is ozone generation. In this case, oxygen or air are passed through the discharge reactor and the conditions in the hot filaments form O_3 . This is used for bleaching processes, water treatment or in medicine. Industrial ozone generators (see figure 4.4) consist of a set of discharge tubes with a length and diameter of 1 – 3 m and 20 – 50 mm, respectively. Each of them is composed of a glass tube inside a metal pipe. The high voltage is applied by a metal coating inside the glass and the outer steel tube, while the discharge is ignited in the small gap between both ducts. The whole setup is cooled in order to achieve a constant temperature necessary for the ozone production. The ozone generation capacity of such modern devices is around 100 kg per hour.

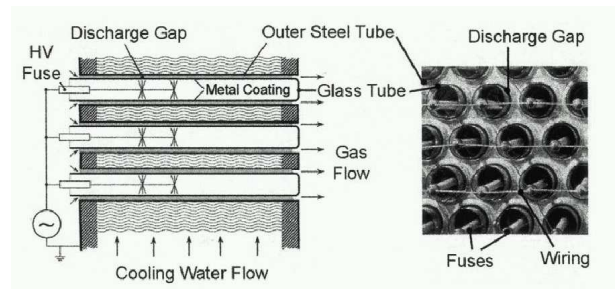


Figure 4.4: Configuration of discharge tubes in a technical ozone generator (not to scale) [Kog03].

Lamps, Displays Plasma conditions in the filaments of the dielectric barrier discharge (high-pressure operation) are ideally suited to induce excimer formation. Choosing an appropriate gas mixture, consisting of rare gas and halogens, ultraviolet (UV) and vacuum ultraviolet (VUV) radiation can be obtained.

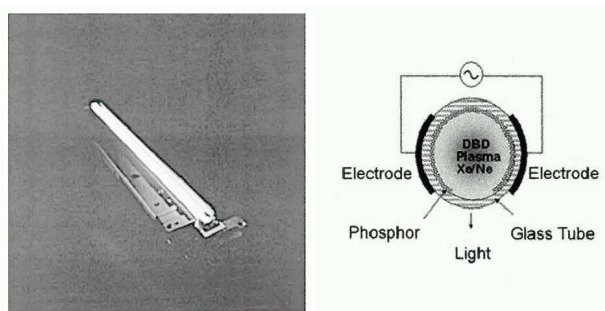


Figure 4.5: Fluorescent lamp based on Xe excimers (USH10) [Kog03].

These lamps (figure 4.5) can be used instead of the mercury lamps e.g. in UV curing processes on printing machines. Furthermore, the generated high energetic excimer radiation can be transformed into visible light via fluorescent layers. Conventionally, large scale lamps consist of a phosphorus layer which is excited by light of a mercury discharge ($\lambda = 254 \text{ nm}$), and

with the right composition generates white light. The use of the new excimer lamps can avoid the presence of the hazardous, toxic mercury. This principle of excimer radiation is also used for the plasma display panels (PDP) which became very popular during the last decades. Here, the electrodes are arranged comb-like in a matrix, whereas the discharge is only burning at the crossing of the electrodes. One pixel of the display is made by three dots, each of them realized by one discharge with different fluorescent layers (red, green, blue). Such a display is flat, emits no x-ray radiation, and enables a high contrast.

Surface treatment Surface treatment came into the focus of research in the 1960s, when affordable plastic foils and other polymer materials became available. It is desired to change the wettability, the receptivity for printing inks or coatings. The use of the dielectric barrier discharge offers the advantage, due to the dielectric in the discharge, to treat metallic foils and other electrically conductive webs as well. Commonly, the surface is treated by the use of air at atmospheric-pressure, but, depending on the application, other gas environments, like N, F, Si, etc. are possible as well. Since the discovery of the atmospheric pressure glow discharge (APGD), the research is focused on that subject due to the fact that a more homogeneous treatment can be obtained. Large devices can treat 10 m wide foils with a speed of 10 m/s.

Depollution of gas streams First investigations on the destruction of H_2S by dielectric barrier discharges were already carried out in 1876 by Berthelot [Ber76], followed by other research groups world wide. Later, it was extended to other hazardous gases like volatile organic compounds (VOCs), chlorofluorocarbons (CFCs) or diesel exhaust gases. The molecules are generally attacked in the discharge by free radicals, electrons or UV photons resulting in the decomposition followed by the formation of less hazardous compounds. Usually, air mixtures are used, because they excite reactive species like $\text{N}_2^*(A^3\Sigma_u^+)$ or $\text{O}_2^*(a^1\Delta_g)$.

Analytical Chemistry Apart from the application of the dielectric barrier discharge as sensor for analytical chemistry in this thesis, the use of an atmospheric pressure barrier discharge in helium as optical emission source used for the detection of halogens was demonstrated by Watanabe et al. [Wat01]. They measured F, Cl, Br and I after the decomposition of volatile halogenated compounds with detection limits of 0.1 μg .

4.1.3 Diagnostics so far

Depending on the gas pressure, the applied voltage and the used plasma gas, the discharge can operate in two modes, a filamentary type and a homogenous one. Figure 4.6 shows the two modes generated between two coplanar electrodes on the upper and lower side with a distance of 4 mm. A homogeneous discharge is shown in the left hand part; here, the discharge is burning over the whole electrode area and only one current pulse per cycle appears. In contrary, several short currents pulses can be observed in the event of a filamentary discharge (see figure 4.6 (b)). The filaments are only few micrometers in diameter and randomly distributed on the electrode surface. The micro filaments start as long as the local field is sufficient for ionization and ends if it is reduced which happens during a time of 1 – 10 ns, in which space charges are summed up at the dielectric. As long as the applied voltage is increasing, filaments can be generated at other places, each of them having a diameter of around 100 μm . Because of the low spatial and temporal expanse of the filaments, the gas is not heated strongly and the micro-discharges are distributed randomly on the electrode surface. Once the polarity of the voltage is changed, new filaments can be formed. Using high frequency, they benefit by the remaining space charges and appear on the same sites, as they will distribute widely using lower frequency. Each single filament is like a weakly ionized plasma channel with a high current density. The space charges in front of the cathode cause a high electrical field, so that field emission of electrons leads to a second avalanche following the first. Important parameters of such filaments for a DBD with 1 mm electrode gap and atmospheric pressure is summarized in table 4.1.

Even though such discharges were used for several decades, plasma diagnostics is not very well developed. Most investigations were limited to electrical characteristics and

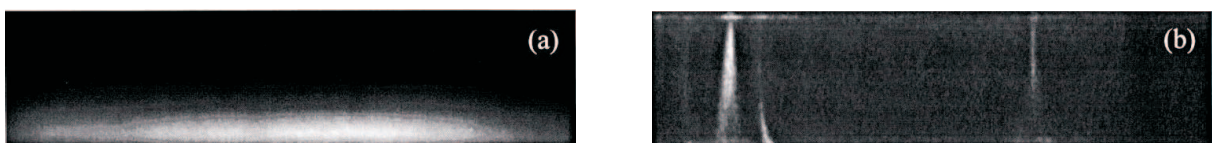


Figure 4.6: Typical 10 ns exposure time photographs of a 4 mm gas gap during: (a) an atmospheric pressure glow discharge (APGD) ($V_{max}=11$ kV) (b) a filamentary discharge ($V_{max} = 14$ kV) [Ghe00]

discharge time	1 – 10 ns	charge	0.1 – 1 nC
radius of filament	0.1 mm	electron density	$10^{14} - 10^{15} \text{ cm}^{-3}$
current density	100 – 1000 A/cm ²	electron energy	1 – 10 eV

Table 4.1: Characteristic values of microfilaments in DBDs.

their evaluation, but are not focused on the measurements of the discharge particles itself which is quite arduous due to the small dimensions. To my personal knowledge, no detailed examination was done to determine densities of electron and excited atoms experimentally with respect to the size up to the beginning of this project. Only simulations of plasma display panels were accomplished, but even the process for generating homogeneous atmospheric pressure discharges is not fully understood yet. A recent review of Kogelschatz [Kog03] reveals that, during the last years, no new knowledge on diagnostic techniques for DBDs was obtained.

4.2 Low-pressure dielectric barrier discharge

4.2.1 Characterization of the discharge

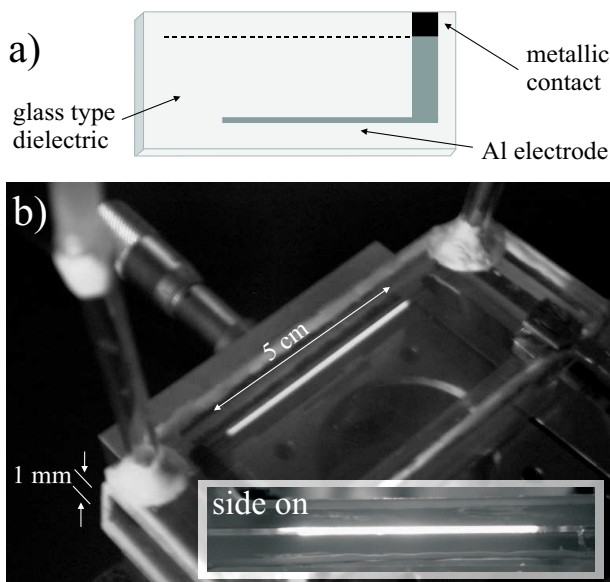


Figure 4.7: The dielectric barrier discharge: (a) electrode arrangement on the glass plate, (b) photos of the discharge.

The discharge chamber is made of glass plates (shown in figure 4.7 a) separated by a distance of 1 mm. Aluminum electrodes (50 mm length, 1 mm width) are deposited on each of the glass plates and covered by a glass type dielectric ($\epsilon_r = 6$) layer with a thickness of 20 μm . Gas connections allowing the gas to circulate, are fixed on the upper plate, and the structure is surrounded by glass windows. Figure 4.7 b shows a photo of the plasma in operation. The discharge works at reduced pressures (10 – 100 mbar) in argon as well as in helium. A rotary pump was used to set the pressure and pass the gas through the discharge with flow rates between 10 –

1000 ml/min controlled by a mass flow controller. The applied voltage had a rectangular shape with a frequency of 5 – 20 kHz and a peak to peak amplitude of 0.5 – 1 kV.

Electrical characteristics

The electrical characteristic of the discharge is presented in figure 4.8. As already described, three different voltages have to be distinguished. The applied voltage V_{appl} (blue) and the plasma current I_{pl} (black) can be measured directly. The gas (V_{gas} , green) and the memory voltage (V_{mem} , red) on the dielectric can only be calculated according to

$$V_{gas}(t) = V_{appl}(t) - V_{mem}(t) \quad (4.1)$$

$$V_{mem}(t) = \frac{1}{C_d} \int_{t_o}^t I_{pl}(t) dt + V_{mem}(t_o). \quad (4.2)$$

C_d	capacity of dielectric
I_{pl}	plasma current
V_{appl}	applied voltage
V_{mem}	memory voltage
V_{gas}	gas voltage

The memory voltage $V_{mem}(t_o)$ on the dielectric of the previous cycle was chosen in such a way that the medium value of V_{gas} was zero. The capacity of the dielectric was determined by the geometrical dimensions to 100 pF (see also [Kun01]). As can be seen, a small phase difference in applied and memory voltage is obtained due to the time constant of the charging process of the dielectric layer. The calculated gas voltage has the same trend as the measured plasma current which approves the simple model.

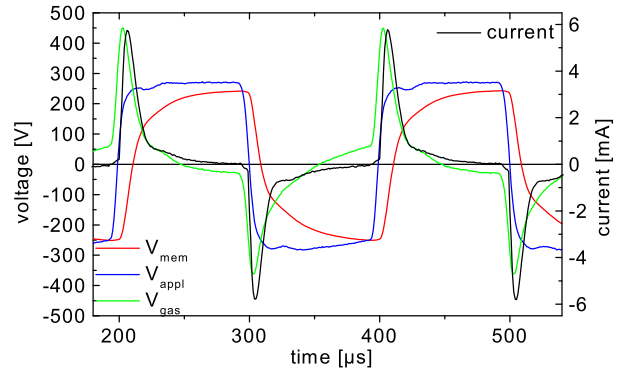


Figure 4.8: Current and different voltages in the dielectric barrier discharge.

The medium electrical power input of the discharge operated at 5 kHz can be estimated by the integral of the current/voltage product, normalized to one discharge period, which is in the range of 0.05 W. This value increases linearly with the frequency. The mean power density in the discharge is, therefore, given to 0.01 kW/cm³ for a volume of 1 x 1 x 50 mm³.

Absorption spectroscopy ‡

The present part is devoted to plasma diagnostics of the low-pressure DBD. This is a challenging task, since the electrode distance of the discharge is very small (1 mm) and the processes in the ac plasma are highly transient. Although DBDs operated close to

‡This chapter has been published in slightly different form in *Diode laser-aided diagnostics of a low-pressure dielectric barrier discharge applied in element-selective detection of molecular species Spectrochim. Acta Part B* 57 (2002) 137 – 146 [Kun02].

atmospheric pressure are widely used, the plasma processes are not yet fully understood. There are only a few papers on the plasma diagnostics of atmospheric DBDs, but there are no detailed investigations on low- and medium-pressure DBDs, such as the one used. Diode laser absorption spectroscopy was used for plasma diagnostics of an argon DBD¹. The measurements were performed with high spatial and temporal resolution (40 μm and 10 ns, respectively). They provided not only the excited-state distribution of short- and long-lived Ar atoms and the diffusion of the metastable atoms, but also the gas temperature and electron density by the analysis of the absorption line profiles.

Experimental arrangement The DBD device was operated in an argon atmosphere at pressures between 10 and 50 mbar with gas flow-rates between 50 and 500 ml/min. The discharge was sustained by rectangular ac-voltage of 750 V_{pp} with a frequency of 5 kHz and rise times of approximately 2 μs .

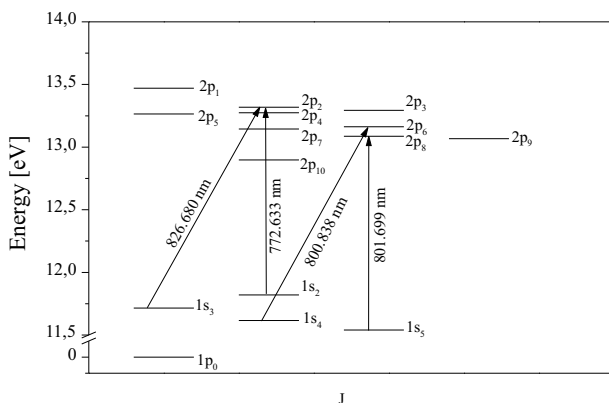


Figure 4.9: Partial energy level diagram of Ar and the transitions studied.

The half-width of the current pulses was approximately 10 μs . During the pulses, the plasma filled apparently the whole volume between the electrodes. Absorption measurements were performed with single-mode laser diodes (line width approx. 45 fm) tuned to one of the Ar lines marked in figure 4.9, which shows the energy diagram of Ar. The investigated lines start from the first four excited states of Ar, two of which are metastable and the remaining two resonance levels. The metastable levels are $1s_5$ and $1s_3$ (Paschen notation²) at 11.55 eV and 11.72 eV above the $1p_0$ ground state, respectively. The lifetime of the metastable levels is 55.9 s for the $1s_5$ and 44.9 s for $1s_3$ [SW75]. The resonance levels are lying close to the metastable levels, i.e. the $1s_4$ level at 11.62 eV and the $1s_2$ level at 11.83 eV. The natural lifetime of the resonance levels is 7.9 ns and 1.9 ns for $1s_4$ and $1s_2$, respectively [Kur96]. The metastable levels have forbidden dipole transition to the ground state which determines their long lifetime. The resonance levels can decay to the ground state by radiation emission at 106.666 nm ($1s_4 - 1p_0$) and 104.822 nm ($1s_2 - 1p_0$). In practice, these resonance states are

¹Investigations on a helium discharge will be presented in the next section (4.2.2).

²Paschen notation was an attempt to fit the neon spectra to a hydrogen-like theory before the advent of quantum mechanics. It is still used in spectroscopy for rare gas atoms.

also long-lived due to resonance radiation trapping and collision transfer processes with the near-lying metastable states.

Transitions from all four lowest levels from $1s_2$ to $1s_5$ were investigated, but most measurements were restricted for simplicity to the two levels $1s_4$ and $1s_5$, one resonance and one metastable. The detected absorption signal provides the time-dependent optical depths $K(t) = \ln(I_o/I(t))$, where I_o is the incident and $I(t)$ the transmitted laser intensity. A typical transient signal $I(t)$ and the current pulse of the discharge are shown in figure 4.10. The optical depths are proportional to the concentrations of the argon atoms, either in the resonance or the metastable states.

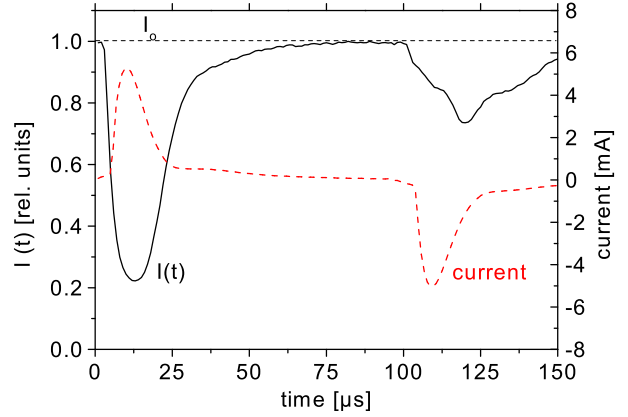


Figure 4.10: Discharge current and absorption signals obtained for Ar atoms in the resonance state near to one electrode.

Investigations of the spatial atomic distribution in the small plasma layer between the electrodes require a spatial resolution of better than $100 \mu\text{m}$. For this purpose, an optical arrangement as shown in figure 4.11 was used. The widened beam of the laser diode³, directed through the discharge zone parallel to the DBD glass plates and expanded by a lens ($f = 16 \text{ cm}$), fell on a screen with a pinhole (diameter 0.2 mm). The intensity of the laser light passing through the pinhole was detected by a photo-multiplier (Hamamatsu). The distance between the lens and screen was 1 m . With this arrangement, it was possible to measure the absorption of a plasma volume with a diameter of approximately $40 \mu\text{m}$

³The experiment was performed 3 times, using the different laser diodes enlisted in table 3.1 for the different transitions.

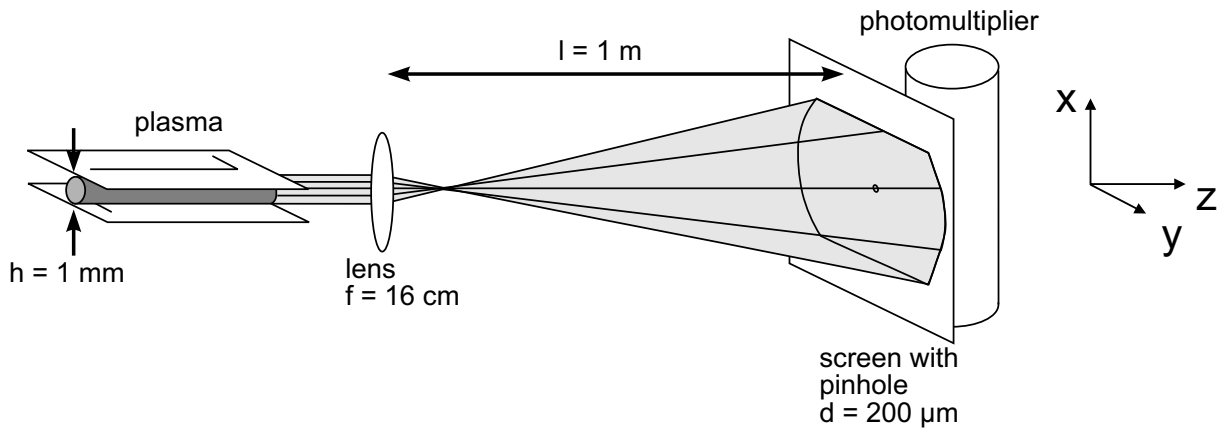


Figure 4.11: Experimental arrangement for diode laser absorption measurements of high spatial resolution.

parallel to the DBD glass plates. A similar optical arrangement, using a hollow cathode as a light source, was already presented in [Vad00]. The absorption signals were measured stepwise by moving the screen with the pinhole in the direction perpendicular (x direction) and parallel (y direction) to the DBD glass plates. In this way, the time-dependent spatial absorption distributions $K(x, y, t)$ with a spatial resolution of $40 \times 40 \mu\text{m}$ in the x - y plane were obtained. The measurements were performed for two orientations of the DBD with respect to the observation axis (z -axis). In the first case, the plasma column was orientated perpendicular to the observation axis (side-on measurements), whereas in the second case, the plasma column was orientated parallel to the observation axis (end-on measurements).

Time-dependent and spatial distributions of excited plasma atoms In the case of side-on measurements, the length of the absorbing layer was approximately 1 mm long and the absorption lines were optically thin with maximum optical depths of approximately 0.06, and 0.28 for the 800.836 and 801.699 nm lines, respectively. The optical depths K_r and K_m , related to the argon atoms excited to the resonance and metastable state, respectively, were strongly dependent on the position x between the electrodes, while they were constant along the plasma column. The optical depths $K_r(x, y = 0, t)$ and $K_m(x, y = 0, t)$ measured for one full discharge cycle at an argon pressure of 20 mbar are shown in figure 4.12 for all four lowest levels of argon.

In each half-period of the applied voltage, the absorption shows a maximum located at approximately 200 – 300 μm from one of the electrodes that is identified as the temporary cathode⁴. At this position, the highest concentrations of Ar atoms in their resonance and metastable states appear at approximately 12 and 17 μs , respectively, after the polarity changes. The different delays are obviously due to different excitation mechanisms for the $1s_i$ states. The resonance states are populated by electron impact, recombination and relaxation processes, while in particular recombination and relaxation are dominating for the metastable states. Furthermore, it can be noticed in figure 4.12 that the concentration of metastable atoms decreases much more slowly than the concentration of atoms in the resonance states. This is the consequence of the different lifetimes. The natural lifetime of the Ar resonance states is in the range of ns, while it is seconds for the metastable states. However, the effective lifetimes greatly vary from the natural lifetimes under the experimental conditions chosen. Radiation trapping of the argon resonance lines increases the effective lifetime of the resonance states, while the lifetime of the metastable states is mainly reduced by collisional quenching processes on the near walls of the discharge. The

⁴The maximum for 826 and 772 nm is shifted a little compared to 800 and 801 nm, because the measurements were performed afterwards with slightly different chamber and pressure conditions.

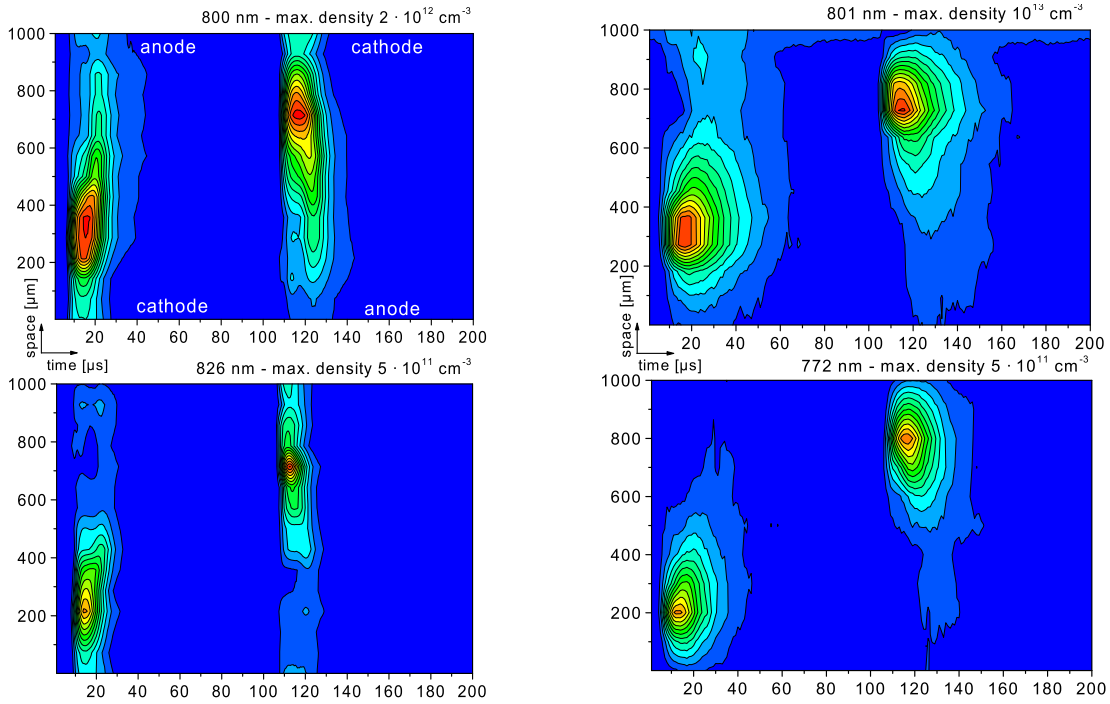


Figure 4.12: Time dependence of the relative peak absorption of Ar measured side-on (pressure 20 mbar, gas flow 200 ml/min); left, resonance states; right, metastable states.

lifetime τ of the resonance states can be estimated using the Holstein formula [Hol51]

$$\tau_o/\tau = 1.15 \cdot \sqrt{\frac{\lambda_r}{3\pi^2 d}}. \quad (4.3)$$

λ_r	wavelength of resonance line
d	optically active volume
τ_o	natural lifetime.

d represents the size of the optically active volume in the form of a thin slab (here $d = 1$ mm). The values calculated of $\tau \simeq 4$ and $1 \mu\text{s}$ are in agreement with the experimental data obtained by fitting the transient signals to an exponential decay. The actual lifetime of the metastable atoms (approx. 0.1 ms) is still significantly larger than that of the resonance state. The end-on measurements of $K_r(t)$ for the 800.835 nm line were performed at various argon pressures and in both vertical (x) and horizontal (y) directions. Figure 4.13 shows $K_r(x, y = 0, t)$ measured at two argon pressures (10 and 50 mbar) between the electrodes.

The distance between the temporary cathode and the absorption maximum is pressure dependent. It is approximately 400 and 200 μm for 10 and 50 mbar, respectively. This behavior is similar to the situation in a glow discharge, where the negative glow is shifted towards the cathode if the pressure increases. Furthermore, figure 4.13 shows that the absorption maximum is shifted towards the temporary anode after the discharge current

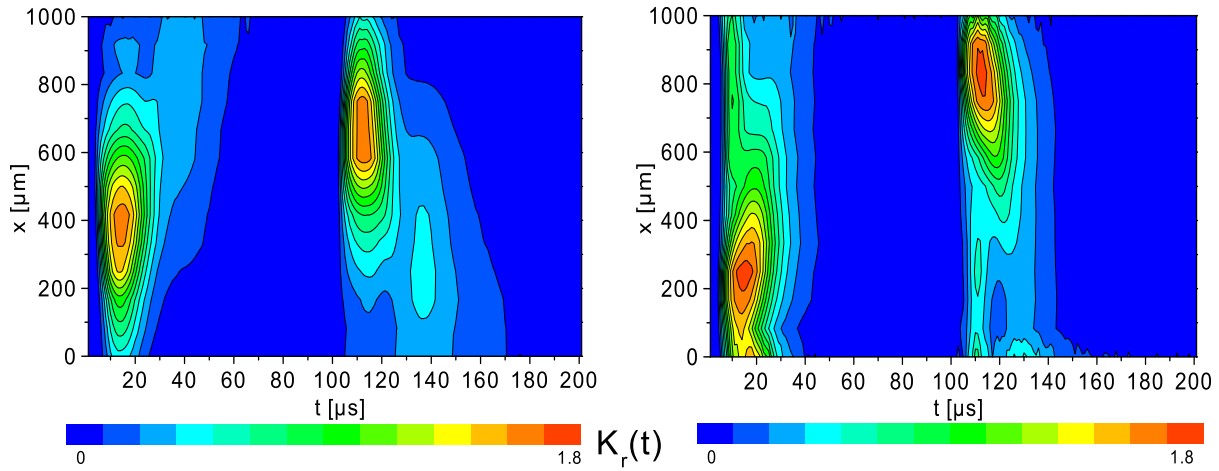


Figure 4.13: Time dependence of the optical depth K_r of the 800.836 nm Ar line measured end-on at 10 (left) and 50 mbar (right).

has peaked. This effect should either be due to excitation processes caused by a much weaker second discharge maximum at 37 μs which is barely evident in figure 4.10 or by a movement of the excited particles. In order to determine the plasma distribution outside the region between the electrodes, $K_r(x_{max}, y, t)$ was measured. As indicated, the data were taken at the x -position where the highest concentrations were detected at 10 and 50 mbar. The results are displayed in figure 4.14. The concentration of excited atoms depends on the pressure, and at lower pressure, the distributions are broader (figure 4.13). However, the excited atoms are mostly confined to the region between the electrodes. Therefore, the shift of the absorption maximum in the x -direction with time cannot be caused by the diffusion of atoms. On the other hand, the excited atoms outside the electrode region indicate the extension of the plasma at lower pressures, i.e. the diffusion of free electrons in the y -direction.

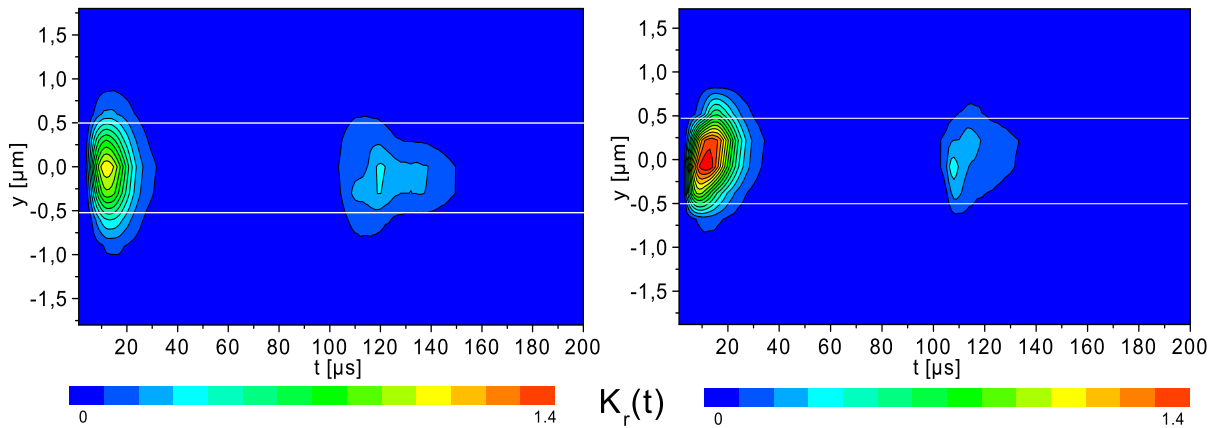


Figure 4.14: Time dependence of the optical depth K_r of the 800.836 nm Ar line measured end-on at the positions of the highest population density at 10 (left) and 50 mbar (right).

Plasma diagnostics The results presented in the previous section show that excited atoms are mainly generated in a very thin layer near the temporary cathode. Therefore, the time-dependent and spatially non-homogeneous discharge is a rather challenging system for plasma diagnostics of the gas temperature and the electron density. These data were obtained by analysis of the absorption profile of the Ar 800.836 nm line measured end-on at the position of highest concentration (x_{max}). The optical depth $K_r(x_{max}, y = 0, t)$ was measured by tuning the laser stepwise in the wavelength region between -15 and $+15$ pm around the line center at λ_o . In this way, a set of data for $K_r(t)$ with the laser detuning parameter, $\Delta\lambda = \lambda_o - \lambda$, was measured. Typical results obtained for three different laser detunings are shown in the left hand side of figure 4.15. Taking into account the complete data set, the absorption profile $K_r(\Delta\lambda)$ at particular times can be constructed, as shown in the right hand side of figure 4.15. At this point, it should be noted that the line profiles might be affected by interference effects in the observation plane if the laser beam is not sufficiently spatially filtered. In this case, the variation of the refractive index within the line profile may cause asymmetries in the absorption line measured. Blue, as well as red, asymmetries may be observed. This effect can be very pronounced if the optical depths in the line centers are greater than 2. The measurements were performed in the line kernel, where the line profile is generally determined by Doppler and impact broadening and can be analytically described by Gaussian and Lorentzian functions, respectively [Uns68]. The profiles measured for $K_r(\Delta\lambda)$ are of the Voigt type, i.e. the convolution of Gaussian and Lorentzian profiles. The shape of the Voigt profile depends on the parameters w_g and w_l which represent the full-widths at half-height (half-widths) of the Gaussian and Lorentzian contributions, respectively. The

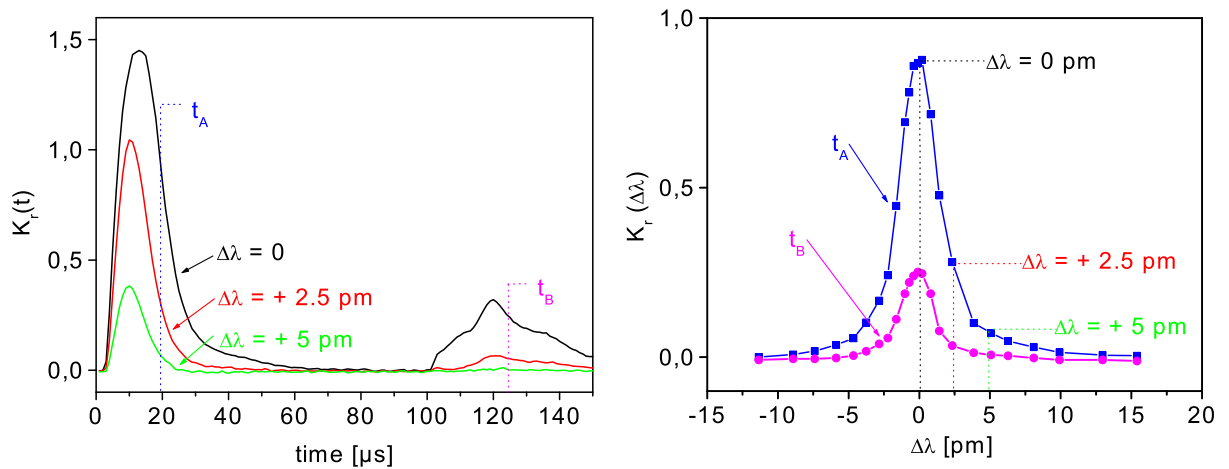


Figure 4.15: Procedure for the construction of the 800.836 nm Ar line profiles at different times (for details see text).

half-width w_v of the Voigt profile is related to w_l and w_g according to equation 3.13. The half-width w_g of a Gaussian profile gives information on the gas temperature T_g by

$$w_g = \frac{2\pi\lambda}{c} \cdot \sqrt{\frac{2RT_g \ln 2}{M}}. \quad (4.4)$$

R	universal gas constant
M	mass of absorbing atoms

On the other hand, the half-width w_l of the Lorentzian profile is given by the sum of particular broadening contributions. In DBD, the main contributions are due to interactions between the optically active atoms on one side and the ground-state argon atoms (pressure broadening) and electrons (Stark broadening) on the other. Therefore, the actual Lorentzian half-width is of the form $w_l^{press} + w_l^{stark}$, $w_l^{press} = \gamma_a N_{Ar}$ where γ_a is the gas temperature-dependent broadening parameter and N_{Ar} the argon density. The Stark-width w_l^{stark} is a complex function of the electron temperature T_e and the electron density N_e . The data for γ_a and w_l^{stark} can be found in [Tac82] and [Gri64], respectively. In order to extract w_g and w_l from the absorption coefficients measured, a standard method which is based on the fact that the normalized Voigt profiles $P_v(\Delta\lambda)$ have Lorentzian wings

$$P_v(\Delta\lambda) \sim \frac{1}{2\pi} \frac{w_l}{(\Delta\lambda)^2}, \quad (4.5)$$

if $(\Delta\lambda) \gg w_v/2$, was used. Then, w_l can be derived from the profile measured for $K_r(\Delta\lambda)$ applying:

$$w_l = 2\pi(\Delta\lambda)^2 \frac{K_r(\Delta\lambda)}{\int K_r(\Delta\lambda) d\lambda}. \quad (4.6)$$

Taking into account the experimental w_l and w_v , the corresponding values for w_g were calculated via equation 3.13. The time-dependent Gaussian half-widths are plotted in figure 4.16. The data represent the widths measured in the volume of highest population density (at x_{max}). Furthermore, the values calculated for the gas temperature are also displayed.

Gas temperature At the time of maximum excitation, the gas temperature is approximately 1000 K. The gas then cools down to room temperature within 10 μ s. During the remaining time of the discharge cycle, the temperature stays constant within the limits of experimental uncertainty, even during the period when the polarity has changed and the second, weaker excitation maximum can be observed. The rapid decreasing of the gas temperature seems implausible, but will be enlightened in the following lines.

quantity	ρ kg/m ³	c_p J/kg K	λ W/mK	η Pa μ s	u m/s	l' mm	k m ² /s
300 K	0.08	520	0.017	22.2	3	1	$4.08 \cdot 10^{-4}$
1000 K	0.02		0.05	70.8			$4.81 \cdot 10^{-3}$

Table 4.2: Specific values for argon at 300/1000 K, 50 mbar and 200 ml/min.

Three different mechanisms have to be taken into account for cooling by heat transfer: radiation, convection and conduction. The radiation follows the Stefan-Boltzmann law and is only important for high temperatures or in the case of low heat conductivity. This term can be neglected due to the low gas temperature and the appropriate values of argon heat conductivity. Heat convection is heat transfer by mass motion. In this case a forced convection as a result of the gas flow appears.

The gas flow at 200 ml/min through an orifice of 1 x 1 mm² is less than 3 m/s. In order to estimate the role of convection, the type of flow in the chamber has to be evaluated. In this case, the Reynold number, defined by

$$Re = \frac{u\rho l'}{\eta}, \quad (4.7)$$

- u gas velocity
- ρ density
- l' characteristic length
- η viscosity

divides the region in the laminar flow ($Re < 2300$), the transient and the turbulent ($Re > 4000$) one. With the values given in table 4.2, the Reynold number amounts to 10 which determines a laminar flow in the chamber. Therefore, most probably only the heat conduction takes part.

This mechanism is defined by means of molecular agitation within the gas without any motion of the material as a whole. The process can be mathematically described by the heat conduction equation, here for a simplified 1-dimensional case:

$$\frac{\partial T(x, t)}{\partial t} = \frac{\lambda}{\rho c_p} \frac{\partial^2 T(x, t)}{\partial x^2}. \quad (4.8)$$

- ρ density
- c_p heat capacity
- λ thermal conductivity
- x distance between electrodes

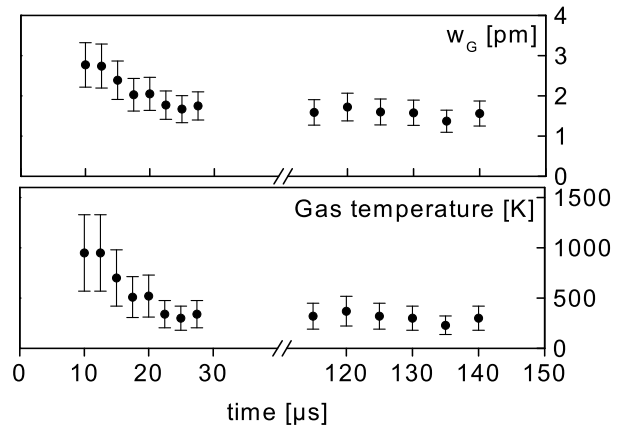


Figure 4.16: Time dependence of the Gaussian half-widths w_g (upper graph). The corresponding gas temperature dependence on time (lower part).

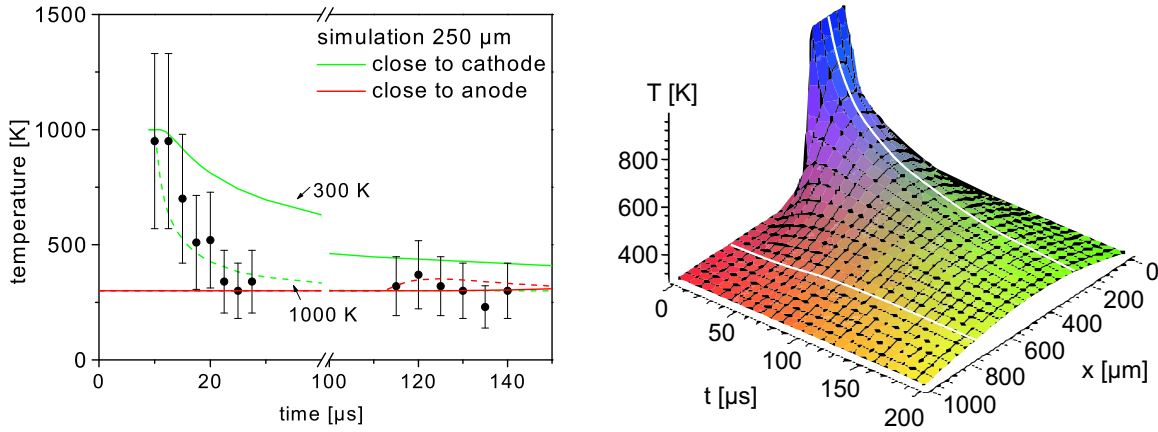


Figure 4.17: left: Experimental measured gas temperatures (as in figure 4.16) and simulated curves; right: simulated temperature profile for data of 1000 K

The cooling of the gas can be simulated, x again being the direction perpendicular to the electrodes and h the height of the chamber. The boundary conditions are chosen in such a way that the walls of the discharge remain at room temperature all the time. This seems to be a reasonable approximation, because excited particles could only be measured in a specific distance of the electrodes. Furthermore, the initial condition for the temperature at time zero can be chosen arbitrary:

$$T(0, t) = 0, \quad T(h, t) = 0 \quad \text{and} \quad T(x, 0) = \phi(x). \quad (4.9)$$

The final solution of this partial differential solution with the above given initial and side conditions is given by

$$T(x, t) = \sum_{n=1}^{\infty} b_n e^{-\left(\frac{n\pi}{h}\right)^2 kt} \sin\left(\frac{n\pi x}{h}\right) \quad \text{with} \quad b_n = \frac{2}{h} \int_0^h \phi(y) \sin\left(\frac{n\pi y}{h}\right) dy. \quad (4.10)$$

In this case, k represents the ratio of $\lambda/\rho c_p$. It is in good agreement with the experimental data to approximate the initial temperature distribution $\phi(x)$ by a rectangular function with 1000 K at a distance of 200 to 400 μm of the cathode and 300 K elsewhere. The factors of k are not invariable over the time, because the temperature is changing. As can be seen in table 4.2, the factor varies for the two extreme temperatures by one order of magnitude. Consequently, the exponential decay is different as plotted in figure 4.17 for the two temperatures of 300 and 1000 K.

The temperature at later times (100 – 150 μs) corresponds to the equivalent temperature close to the anode. Consequently, the simulation shows the values obtained for earlier

times 750 μm far away from the cathode (see right hand side of figure 4.17). As it can be seen, there is good agreement with the experimental data for this very simple model. For further investigations one would have to revise the assumption of laminar flow, because of the strong temperature gradients. Furthermore, a 2-dimensional heat equation could include the gas flow. Interestingly, the dependence on anode side can be well simulated, too.

Electron density The time dependence of the Lorentzian width w_l , displayed in figure 4.18, qualitatively shows similar behavior as the Gaussian width. With the exception of the time of the first discharge maximum, w_l is constant during the whole discharge cycle ($w_l \simeq 1.7$ pm). Taking into account the experimental error bars, this room-temperature value of w_l agrees well with the values for pressure-broadening w_l^{press} derived from [Tac82]. The contribution of pressure broadening to w_l for the ‘hot’ discharge period (see figure 4.18) was calculated taking into account the reduced number density in the discharge volume probed (application of Dalton’s law) and the typical temperature dependence ($\propto T^{0.3}$) of the pressure-broadening parameter. The difference between the values measured for w_l and the w_l^{press} data calculated yields the contribution of Stark broadening (w_l^{stark}) to the measured half-width w_l . The Stark widths w_l^{stark} are plotted in figure 4.19. Outside the ‘hot’ discharge period, the w_l^{stark} data cannot be evaluated, since the experimental error bars are too large. The calculation of the electron density from w_l^{stark} requires the electron temperature according to [Gri64]

$$\Delta\lambda_{Stark}^{width} = 2(1 + 1.75 \cdot 10^{-4} \sqrt{N_e} \alpha (1 - 0.068 \frac{\sqrt[6]{N_e}}{\sqrt{T_e}})) \cdot 10^{-16} w N_e \quad (4.11)$$

and the corresponding values are enlisted in table 4.3.

Unfortunately, the electron temperatures could not be determined within the scope of the present work. However, taking into account the experimental conditions, the electron temperature should be in the range of 10 000 – 300 000 K. The lower limit of 10 000 K corresponds to the excitation temperature of the resonance and the metastable argon

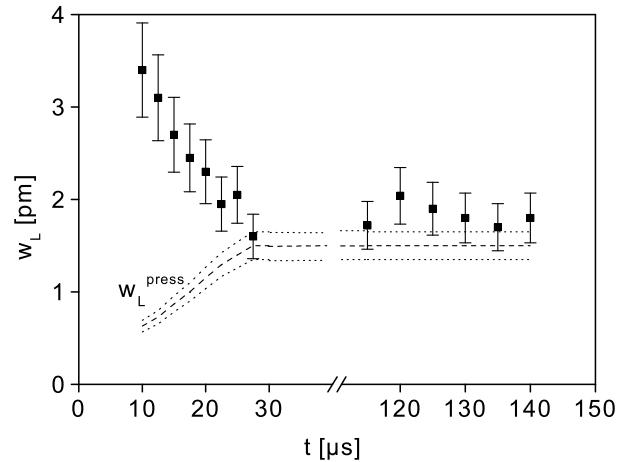


Figure 4.18: Time dependence of the Lorentzian half-width (near the temporary cathode).

T	2 500 K	5 000 K	10 000 K	20 000 K	40 000 K	80 000 K
w	$3.5 \cdot 10^{-2}$	$4.38 \cdot 10^{-2}$	$5.76 \cdot 10^{-2}$	$7.65 \cdot 10^{-2}$	$9.43 \cdot 10^{-2}$	$1.04 \cdot 10^{-1}$
d/w	1.768	1.655	1.381	1.032	0.752	0.565
α	0.047	0.040	0.032	0.026	0.022	0.021

Table 4.3: Coefficient for Stark broadening given in Angstrom, $\lambda=800.835$ nm [Gri64].

states obtained from the excited to ground-state argon atoms density ratio, while the upper limit is related to the maximum kinetic energy the electrons can accumulate on the average free path in the electric field applied. Nevertheless, this large uncertainty in the experimental electron temperature does not affect the uncertainty of the electron density to the same extent. Furthermore an electron temperature of around 1 eV can be determined by the particle balance presented in figure 2.3.

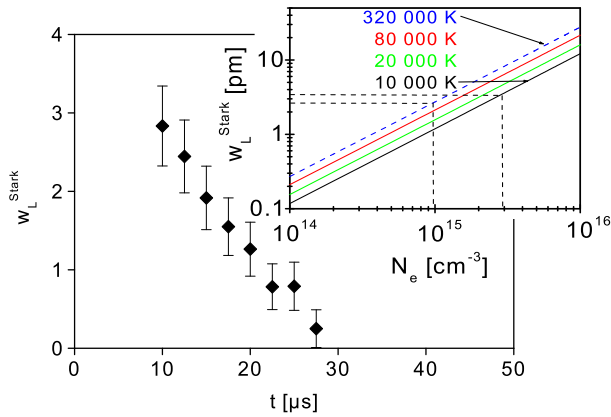


Figure 4.19: Time dependence of the Stark width obtained from the data shown in figure 4.18. Inset shows theoretical values of w dependent on electron density.

The inset of figure 4.19 shows w_l^{stark} in relation to N_e and T_e obtained by use of the theoretical results published in [Gri64]. The Stark broadening parameters were calculated for electron temperatures in the range between 2 500 and 80 000 K. The dashed blue curve ($T_e = 320\,000$ K) in figure 4.19 is an extrapolation of the theoretical results. Taking into account the experimental errors and the uncertainty in T_e , the data show that the largest value of w_l^{stark} corresponds to an electron density in the range $1 \cdot 10^{15} - 3 \cdot 10^{15} \text{ cm}^{-3}$.

Taking into account the maximum electron density of $3 \cdot 10^{15} \text{ cm}^{-3}$ and the Ar number density of about $1.5 \cdot 10^{17} \text{ cm}^{-3}$ at 20 mbar and 1000 K derived from the ideal gas equation, approximately 1 % of all Ar atoms are ionized. The number density of the Ar atoms N_{Ar}^* in the metastable and resonance states can be calculated from equation 3.5, taking into account the side-on measured optical depths K of the corresponding lines at the time and position of maximum absorption (see figure 4.12) and the approximate absorption length for side-on measurements (1 mm). The maximum number density values were found to be $5 \cdot 10^{11}$, $5 \cdot 10^{11}$, $2 \cdot 10^{12}$ and $1 \cdot 10^{13} \text{ cm}^{-3}$ for the $1s_2$, $1s_3$, $1s_4$ and $1s_5$, respectively.

Concluding remarks High spatial-resolution plasma diagnostics of low-pressure DBD diode-laser absorption spectroscopy gave clear evidence for a thin, short-lived plasma layer

of approximately 40 μm thickness and 1 mm width near the temporary cathode. In this layer, plasma atoms are efficiently excited, the gas temperature reaches approximately 1000 K and an electron density of greater than 10^{15} cm^{-3} can be found. In all other areas, the excitation is less efficient, the gas temperature is near room temperature, and the electron density is below 10^{14} cm^{-3} . This means that most of the electrical power is used to heat a very small plasma volume for a short time. The mean power consumption of the discharge is less than 0.1 W. The discharge volume is given by the electrodes (50 mm x 1 mm) and the distance between the electrodes (1 mm), resulting in a volume $5 \cdot 10^{-2} \text{ cm}^3$. Therefore, the integral power density is about 1 W/cm^3 . The peak power density is 100 times higher, because the highest atom and electron density is strongly localized in about one tenth of the discharge volume. Furthermore, the half-width of the current pulse is also only a tenth of the whole plasma cycle. Consequently, the peak power density of 0.1 kW/cm^3 is in the same order of magnitude as the mean power density of an inductively coupled plasma (ICP). In an ICP with a conical plasma torch length of about 25 mm and a diameter of 25 mm the input power is typically about 1 kW, resulting in an average power density of about 0.5 kW/cm^3 .

4.2.2 Analytical application

Absorption measurements – Improvement of the detection limit

During my diploma work [Kun01], the dielectric barrier discharge was already implemented as a detector for analytical purposes, which was also published in [Mic01]. Diode laser atomic absorption spectroscopy was used to trace halogenated molecules in gases. A laser beam of 1 mm diameter (distance between electrodes) probed the absorption along the discharge channel. The absorption signal was measured by a phase sensitive detector using the ac modulation frequency of the DBD. The different concentrations of halogenated hydrocarbons were obtained by diluting an initial mixture of 17 ppm (v/v) CCl_2F_2 , CClF_3 or CHClF_2 in a rare gas (Ar, He) down to concentrations near the detection limit. The limits of detection (defined by the 3σ -criterion) for all halogenated hydrocarbons in the Ar DBD were approximately 5 ppb, using the 837.824 nm Cl absorption line, which probed the metastable Cl atoms. In He, the detection limits were 400 ppt and 2 ppb for CCl_2F_2 using the Cl 837.824 nm and the F 685.792 nm line, respectively. The absorption signals of Cl and F at high analyte concentration values (several ppm) correspond to the stoichiometric ratios of these elements in the molecules, which prove equal dissociation of different analytes. The averaged gas temperature obtained by the

evaluation of the gaussian profile of fluorine absorption was shown to be low (500 K). This value is in close agreement with an averaged value of the spatially resolved measurements, which would lead to around 400 K. This low medium gas temperature allows the operation of the DBD over a long period of time (over 500 h of continuous operation).

As was presented in the previous section, the excited atoms in the argon discharge are restricted to a small volume. Therefore, the above-mentioned measurements of halogenated hydrocarbons by diode-laser absorption spectroscopy of excited chlorine or fluorine can be improved significantly. In the former experiment, the diode laser beam filled the whole space between the electrodes. However, the main absorption obviously was only in the small layers near the temporary cathodes. Hence, the spatial distribution of excited chlorine atoms in the discharge has to be determined and, finally, the absorption has to be measured only in a restricted volume. For the following investigations, the discharge was operated in He or Ar with CCl_2F_2 admixture. The measurements were performed at a frequency of 5 kHz and about 700 V_{pp} applied. The excited Cl atoms in the metastable level were determined using the high resolution arrangement presented previously (figure 4.11). The laser diode (Hitachi HL8325G) was tuned to the transition of the chlorine line at 837.824 nm ($^4\text{P}_{5/2} - ^4\text{D}_{7/2}^o$). The distribution of the excited Cl atoms on the metastable ($^4\text{P}_{5/2}$) level was measured in Ar with 150 ppm CCl_2F_2 (total flow rate 150 ml/min) for pressures between 20 and 50 mbar where the discharge presents a uniform working regime (glow type discharge). At higher pressures, filaments are formed, which can be observed easily in the shape of the current pulse. Measurements were also performed in He in which the discharge is working in a stable mode up to 120 mbar. It has to be noted that this high CCl_2F_2 concentration has no analytical relevance. It was only used in order to obtain direct absorption signals which give the spatial and temporal distribution.

The relative distributions of the excited Cl atoms for one period of the applied voltage in Ar as well as in He are presented in figure 4.20 for different pressures. From these measurements it can be seen that there is a difference between the absorption signal if Ar or He as carrier gas is used. In Ar the maximum density of excited Cl atoms is close to the temporary cathode, similar to the results obtained only in the Ar plasma. Furthermore, increasing the pressure, this maximum is moving closer to the cathode; this proves that the main part of energy is dissipated in a layer near to the cathode. The distribution of Cl atoms in He follows a totally different behavior. Most of the excited atoms on the metastable level are produced between the middle of the discharge and the anode.

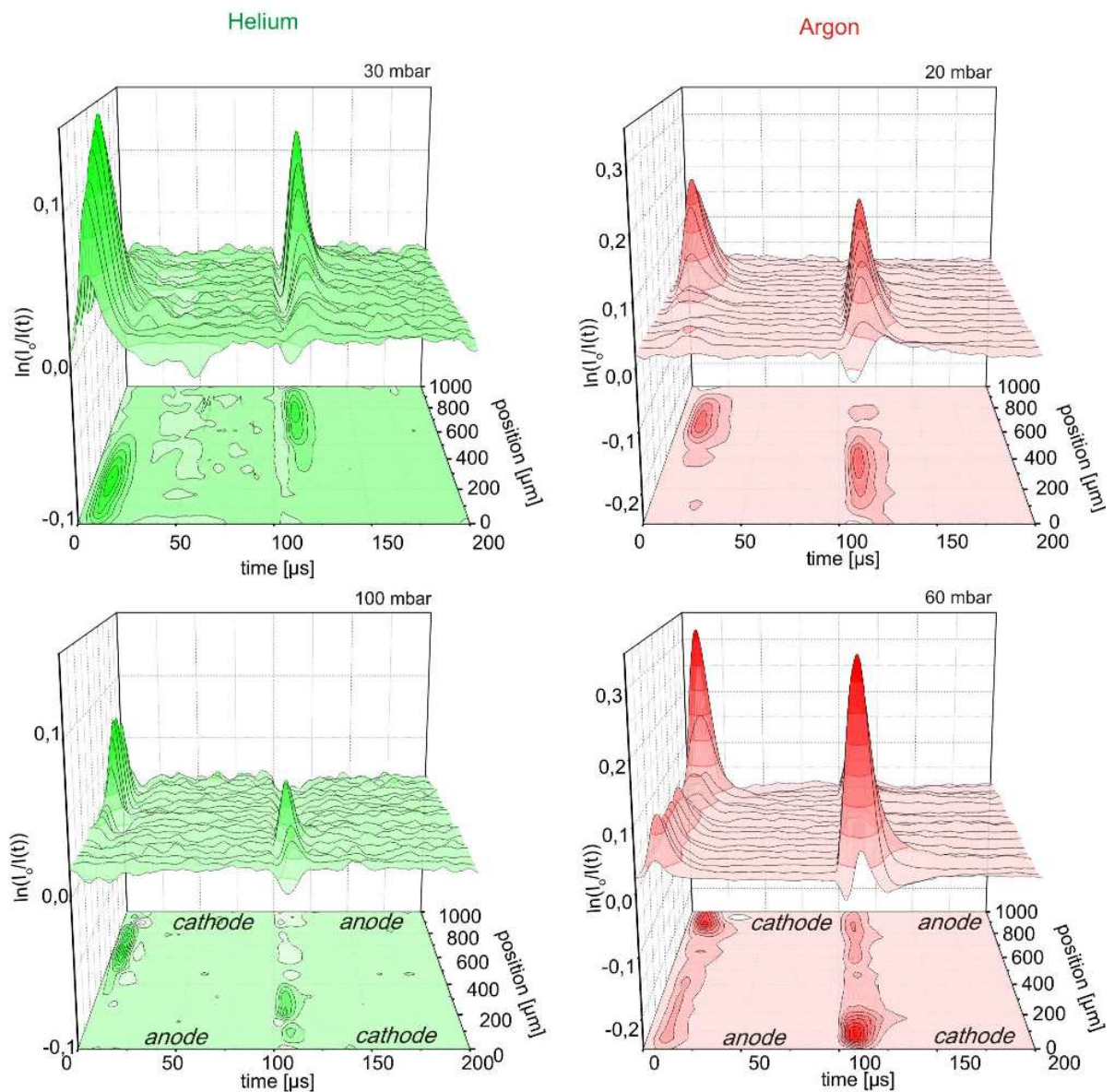


Figure 4.20: Spatial distribution of chlorine atoms on metastable state in a helium (left) and argon (right) discharge for different pressures.

Only at much higher pressures the maximum is displaced in the direction of the cathode. Measurements of Ar excited atoms in an Ar/He mixture showed the same distribution like Cl/He mixtures.

The different distribution of excited Cl atoms in these two carrier gases can be explained taking into account the mechanisms of production of these excited atoms. The CCl_2F_2 molecule is dissociated in collision with the energetic electrons (complete dissociation energy around 16 eV) and Cl negative ions are formed. The electron detachment process followed by collisions with electrons and neutral atoms lead to the formation of Cl atoms in the ground and excited states. There are few factors that generate different density

distribution of the excited atoms between the electrodes. First of all, the electron density in the He plasma is smaller than in Ar at the same operation conditions. As a consequence, there is a smaller density of excited Cl atoms in He (3 times smaller as can be seen from figure 4.20) than in Ar, since the excitation is caused by electrons.

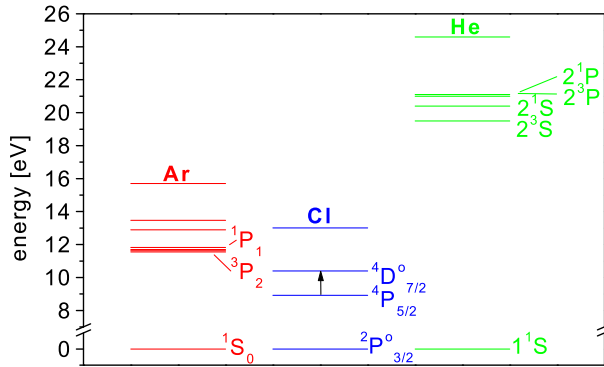


Figure 4.21: Energy diagram of Ar, He and Cl.

The metastable atoms of the buffer gas (see figure 4.21) have also an important role in the feeding of the $^4P_{5/2}$ Cl level because they are a deposit of energy in the discharge. The first excited levels of Ar are close (3 eV) to the Cl $^4P_{5/2}$ level and collisional transfer between these levels resulting in the population of Cl level is very probable. In He the metastable levels are much higher and Cl atoms cannot be excited to metastable levels through the same mechanism as in Ar.

The displacement of the maximum density of Cl excited atoms can be explained (i) by the value of the mean free path of the electrons which is 3 times smaller in Ar than in He [Eng75] and (ii) the drift velocity of electrons that is in He 3-5 times higher at the same reduced electric field. Electrons produced close to the cathode are moving further in a helium discharge than in an Ar discharge. If we assume that Cl atoms are generated mostly by collisions with electrons then the distribution of these excited atoms between anode and cathode is much broader in He than in Ar.

The temporal behavior is also different, the absorption signal of Cl excited atoms is narrower in He than in Ar. The excited atoms are decaying faster from the metastable level in the case of He. Furthermore, with Ar as buffer gas, the absorption signal of Cl reaches another maximum at later times (later than 5 μ s after the first maximum) and the formation time of this maximum depends on the position in the discharge. It is assumed that the second maximum is connected with the time dependent diffusion of the metastable atoms [McD64] produced in the negative glow of the discharge. This proves that Ar metastable atoms have a strong influence. Such behavior was not observed in the He plasma.

According with these results, it is clear that measuring the density of the excited Cl atoms in Ar spatially resolved will improve the detection limit reported in [Mic01]. No change is expected in He due to a much broader spatial distribution. It has to be mentioned that the modulation and detection of the signal must be adapted to the new arrangement.

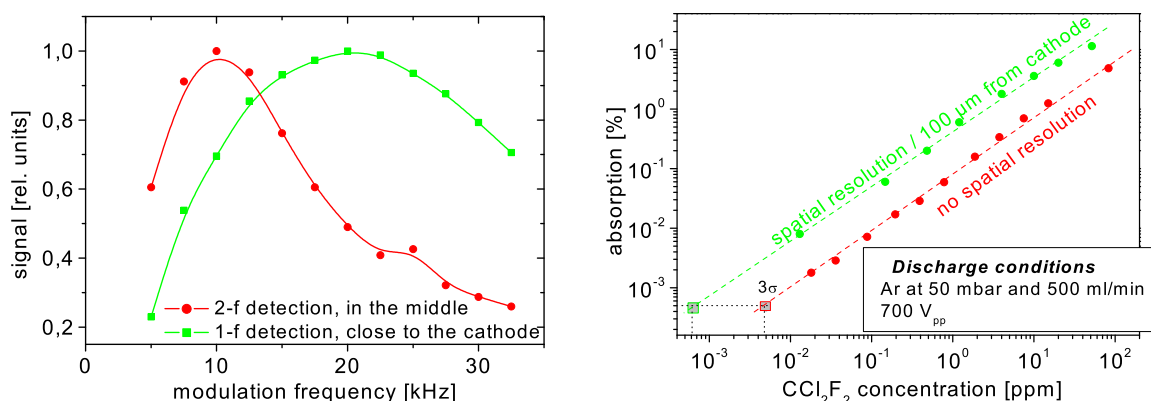


Figure 4.22: left: Cl signal dependence in Ar discharge on modulation frequency; right: Calibration curve of CCl_2F_2 in Ar measured with and without spatial resolution.

In the earlier case, the detection was performed phase-sensitive on twice the modulation frequency because the plasma was switched on and off twice during one period of the applied voltage. A Fourier transform of the absorption contains accordingly only 2- f components.

If the measurements are resolved spatially (close to the cathode), absorption is only obtained once in the period of the applied voltage. Consequently, the strongest component of the Fourier transform is the 1- f signal. Furthermore, because the temporal decrease of the absorption signal depends not on the modulated voltage, but on the lifetime of the investigated species, the frequency has to be customized. Different densities in the discharge, changing by pressure and gas flow, result in different lifetimes of the species. Figure 4.22 shows the signal dependence on the modulation frequency for 1- and 2- f detection. The signal for the 2- f modulation was obtained spatially resolved in the middle of the discharge. This corresponds to the previous measurement without spatial resolution because on each two half period the signals are equal. The 1- f signal was measured close to the cathode with only one signal for one period. The 2- f modulation reveals a maximum at 10 kHz as it was already reported earlier [Mic01]. In contrary, using 1- f detection the frequency has to be twice as large, which can be explained by the same exponential decay of the excited species.

From the calibration curve shown in the right hand side of figure 4.22, it can be seen that the Cl absorption measured in Ar as carrier gas is one order of magnitude higher if the measurements are performed only in the effective plasma volume located 100 μm from the cathode. Accordingly, using a low noise detector the former detection limit of 5 ppb CCl_2F_2 in an argon discharge can be improved by one order of magnitude, resulting in the same limit of detection as in a helium discharge.

The dielectric barrier discharge as a detector for gas chromatography †

The results presented above showed that the dielectric barrier discharge is as powerful plasma for the detection of halogenated gases. However, in routine analysis, when different molecular species have to be analyzed, a separation before the detection is required (see figure 3.1). Therefore, the capability of the DBD as a detector for gas chromatography was tested.

Experimental arrangement The experimental arrangement is shown in figure 4.23.

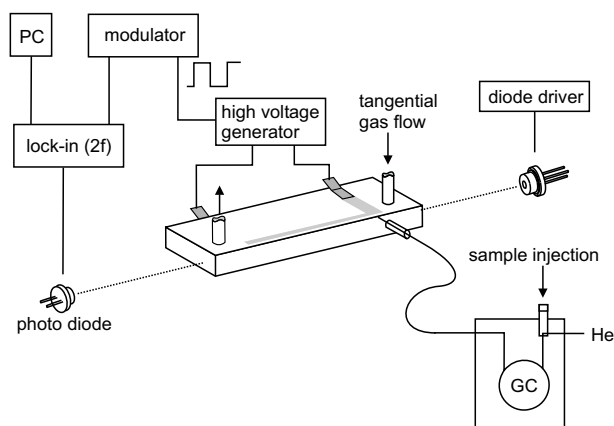


Figure 4.23: Experimental arrangement of DLAAS in the DBD coupled with a GC.

Absorption measurements were performed by passing the collimated beam of a laser diode through the plasma volume without filtering spatially. The transmitted laser radiation was measured by a photo diode. In contrast to the previous measurements [Mic01], the discharge volume was restricted by two additional glass spacers forming a small plasma channel to reduce the dead volume. Most of the measurements were performed in helium and, therefore, it was not necessary to collimate

the laser beam to the size of the plasma which only results in an improvement in the detection limits if DLAAS in Ar DBD's is performed (see section 4.2.2). Beam collimation would complicate the arrangement, too, and makes it less robust, in particular if more than one diode laser is used. The separation of the species was performed by a gas chromatograph (Shimadzu GC-14A), using a fused silica capillary column (FS-SE-54-CB-1). The end of the column was connected to the DBD-chip perpendicular to the plasma gas flow and very close to the plasma volume.

The molecular species in the test samples are enlisted in table 4.4. The initial sample contained 20 $\mu\text{l/ml}$ of each component and was diluted six times by a factor of four. The carrier gas of the gas chromatograph was helium, while helium as well as argon was applied as plasma gas. The temperature program was set as follows: 60 $^{\circ}\text{C}$ initial temperature, 0 min start time, 25 $^{\circ}\text{C}/\text{min}$ heating rate, 200 $^{\circ}\text{C}$ final temperature, 200 $^{\circ}\text{C}$ temperature at injection port. Samples of 1 μl were injected manually with a syringe into the split-less

†This chapter has been published in slightly different form in *The dielectric barrier discharge as a detector for gas chromatography Spectrochimica Acta Part B* **58** (2003) 1435 – 1443 [Kun03].

injector of the gas chromatograph.

For the measurements of the chlorinated hydrocarbons the laser diode that was mentioned before was used (section 4.2.2). The absorption signals were determined as in the previous experiment [Mic01] with a phase-sensitive lock-in amplifier (Stanford Research SR810 DSP) using the double modulation frequency of the plasma generator as reference. The signal was acquired by a personal computer and the data evaluation was done off-line. Two other laser diodes were used in this experiment, a Mitsubishi ML 1012R-01 laser diode for the detection of the fluorinated

fluorobenzene (C ₆ H ₅ F)
1,2-dichloropropane (C ₃ H ₆ Cl ₂)
1-bromobutane (C ₄ H ₉ Br)
1-chloropentane (C ₅ H ₁₁ Cl)
1-iodobutane (C ₄ H ₉ I)
2,5-dimethylthiophene (C ₆ H ₈ S)
1-bromo-4-chlorobutane (C ₄ H ₈ BrCl)
hexane (C ₆ H ₁₄) as solvent

Table 4.4: Samples used for the gas chromatograph.

hydrocarbons (F line at 685.792 nm) and a commercial external cavity diode laser (ECDL, *Toptica*, Germany) for the detection of sulfur (S line at 921.539 nm) as well as iodine containing species (I line at 906.081 nm). The measurements of C₄H₉Br and C₄H₈BrCl by the 827.472 nm Br line could be performed with the same diode as for chlorine. All three diodes were aligned collinear for simultaneous detection, and attenuated with a neutral filter to about 500 μW in order to avoid optical saturation.

Optimization of parameters The dielectric barrier discharge is a very powerful plasma despite the fact that the mean power consumption is relatively low. Therefore, the plasma should be very robust against loading by eluates coming from the gas chromatograph. It was observed that the plasma in helium was only quenched for a short time, when the solvent was released from the column, but it was self-reignited without an auxiliary spark shortly after. In argon the plasma was not extinguished at all, but filamentation of the plasma could be noted when the solvent hexane arrived in the DBD. In order to protect the discharge chamber and to improve the lifetime of the chip, the plasma was manually switched off during the residence time of the solvent and it was switched on after it had passed the discharge chamber. The time between the reignition of the plasma and the first eluate was approximately 15 s. Chromatograms of the test sample detecting F, Cl, Br, I and S are presented in figure 4.24.

The four halogens as well as sulfur were measured sequentially. All responses were normalized for better visualization. The relative absorptions of S, F, Br and I compared with Cl were smaller by factors of about 5, 10, 20 and 100, respectively. There are weak

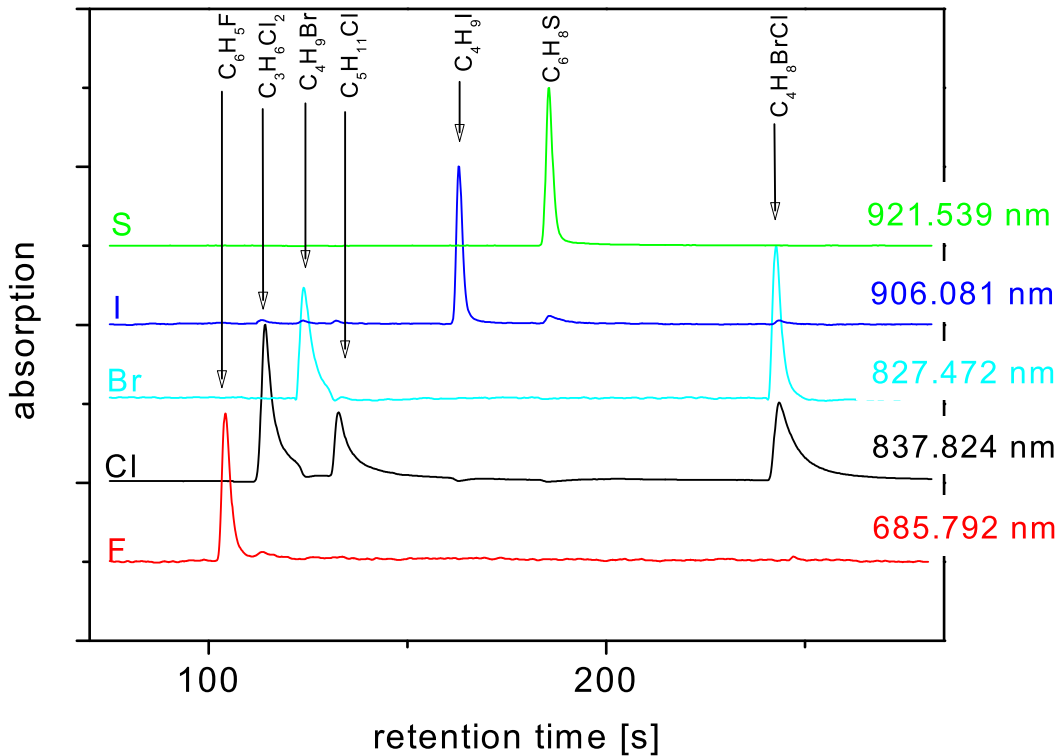


Figure 4.24: Normalized chromatograms of the substances enlisted in table 4.4 in hexane monitoring the different elemental absorption lines. The concentration of each species is 300 nl/ml.

absorption signals in the iodine chromatogram at the retention times of the species that do not contain iodine. These signals are non-specific for iodine. They are a result of changes in background absorption at the position of the I-line affected by the respective species. Furthermore, there is a broadening of the Cl signals that will be discussed later. Although all elements could be detected, the measurements were mainly restricted to the detection of chlorine. The test sample with all species was used to study the influence of different species on the signals analyzed. An influence of one substance on the detection of the other is also called matrix-effect in analytical spectroscopy. The detector was optimized for Ar and He by varying the flow and pressure of the plasma gas, as well as the discharge voltage. The time constant of the lock-in was chosen in such a way that both the peak shape and noise were acceptable. While the noise is reduced with higher time constant, the shape of the absorption signal was affected by time constants higher than 300 ms. Therefore, 300 ms was used for all measurements. The DBD can be operated at voltages less than 500 V but atomic absorption is not measurable. An increase in the voltage improves the signal until it reaches a constant value. Here, an efficient dissociation of the species is assumed. However, the voltage which is necessary for complete dissociation depends on the concentration of the analyte. It should increase with

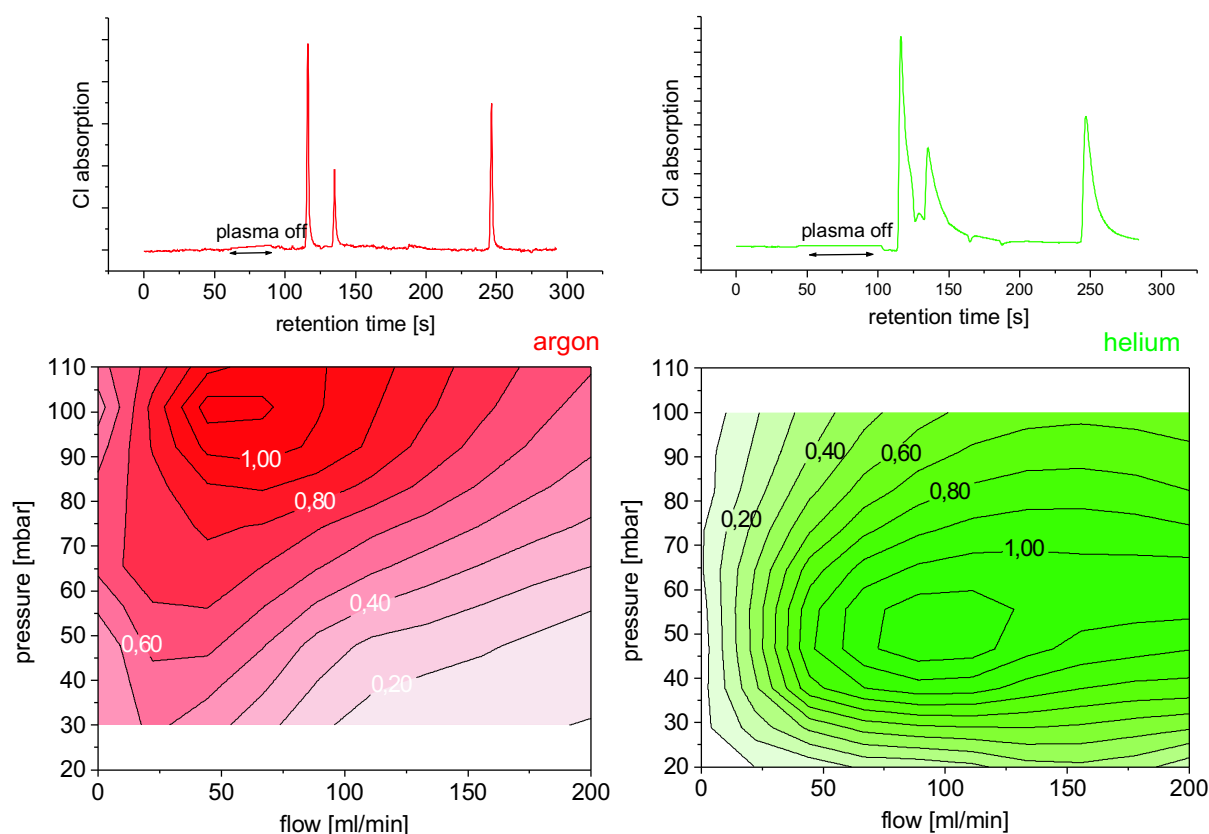


Figure 4.25: Upper part: chromatograms obtained in helium and argon discharges by DLAAS of the Cl 837 nm line; lower part: Cl absorption measured with 1-bromo-4-chlorobutane (C_4H_8BrCl) dependent on pressure and gas flow, normalized to the best obtained conditions.

increasing concentration. On the other hand, at high voltages (1 kV) plasma filaments can be observed and the lifetime of the discharge is reduced. Consequently, the peak to peak voltage was kept constant for the measurements at 800 V. It should be noted that an increase in signal dependent on the voltage could partly be due to an expansion of the constricted plasma volume (see section 4.2.2). However, this was not investigated. The dielectric barrier discharge can be sustained with small gas flows. The flow through the GC-column (about 5 ml/min) is sufficient to operate stable plasma. Anyhow, it was noted that the signal shapes in the chromatograms are very broad. Additionally, the background was not constant over the whole chromatogram, because the pressure, as well as the viscosity of the gas, changes as a result of the temperature ramp generated by the GC. Therefore, the use of an additional gas flow is advisable as was also reported by [PB96]. Figure 4.25 (upper part) shows a Cl chromatogram taken with argon and helium as buffer gases. In the lower part the relative absorption of 1-bromo-4-chlorobutane (the third peak) dependent on pressure and gas flow is plotted for each gas.

With respect to the absorption in the argon plasma a strong dependence of the signal on both the pressure and the flow was observed. In contrast, the signal in helium is

less dependent on the flow, as long as there is an additional flow, since the contour lines are almost parallel to the x -axis. In argon the flow has to be low (50 ml/min) and the pressure as high as possible to obtain the best signal. In helium the pressure has to be lower, about 50 mbar. This dependency on flow and pressure is due to changes in the plasma conditions. The strong pressure dependent increase of the signal in argon could be explained by the transition from a homogenous plasma to a filamentary one. The latter plasma mode shortens the lifetime of the plasma chip significantly; consequently, pressures lower than 100 mbar should be used.

Analytical results The stoichiometry of the three chlorine containing substances $C_3H_6Cl_2$, $C_5H_{11}Cl$ and C_4H_8BrCl , has a ratio of 2 : 1 : 1. However, experimental ratios calculated from the signal heights as well as from the integrated signals were 2 : 0.97 : 1.67 for Ar and 2 : 0.89 : 1.44 for the He DBD as can be seen in figure 4.25. While the measured ratio of the first two components is similar to the theoretical ratio, the third component is too large. It could be possible that the plasma is still affected by the solvent at the retention times of the first two components. The time between the arrival of the solvent and the first eluates has to be increased in order to improve the stoichiometry, e.g. by application of a solvent with a lower boiling point. Another possibility is the use of a bypass line for the solvent. In commercial devices this problem is solved by a reversed flow, whereby the gas flow is inverted for the time of the solvent preventing it to pass the chamber.

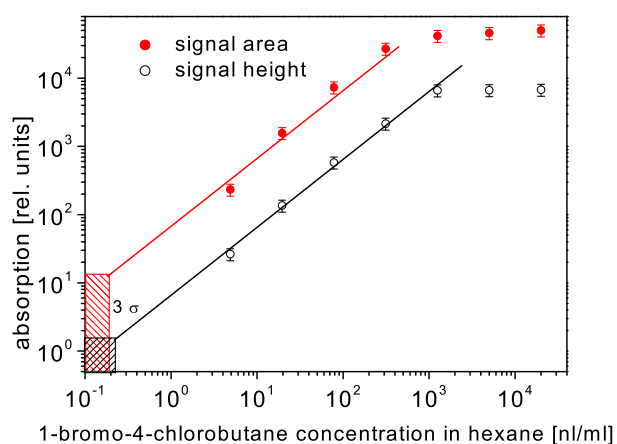


Figure 4.26: Calibration curve for 1-bromo-4-chlorobutane (C_4H_8BrCl) in hexane obtained by DLAAS of the Cl 837 nm line.

of each substance. A 3σ detection limit of 200 pl/ml was found for C_4H_8BrCl . Taking

A calibration of 1-bromo-4-chlorobutane for the helium discharge is shown in figure 4.26. The amplitude of the peaks (open circles) is linear over 3 orders of magnitude, while at high concentrations the calibration curve flattens. If the signal areas of the chromatograms are taken into account (full circles) a similar calibration curve and detection limit is obtained. At high concentrations (more than 1 μ l/ml) the plasma conditions are greatly affected which can even be seen directly, i.e. the color of the discharge changes during the elution time

into account the injected volumes of 1 μl this corresponds to detection limits of 300 pg for $\text{C}_4\text{H}_8\text{BrCl}$ and 60 pg for Cl. The half-width of the peaks is about 10 s and therefore, the chlorine flow at the limit of detection is about 6 pg/s. Although the plasma is still slightly affected by the solvent, the first two species in the chromatogram ($\text{C}_3\text{H}_6\text{Cl}_2$ and $\text{C}_5\text{H}_{11}\text{Cl}$) have linear calibration curves and detection limits in the same order as found for $\text{C}_4\text{H}_8\text{BrCl}$. With the measurements summarized in the first part of this section a detection limit of 400 ppt for freon (CCl_2F_2) was reported using DLAAS for Cl at a gas flow of 500 ml/min in a helium discharge. This amounts to a chlorine flow of 10 pg/s at the limit of detection, which is in the same order of magnitude compared to the actual experiment. The detection limit in the argon discharge was a factor of 10 higher, which can be seen in the GC measurements as well. While the absorption signal is almost the same, the noise is one order of magnitude higher than in helium. Therefore, a calibration leads to a detection limit of 300 pg chlorine.

Improvement of selectivity It is remarkable that the width of the chromatographic peak in argon is much narrower than that in the helium discharge (see figure 4.25). Accordingly, the chlorine flow at the limit of detection is comparatively higher with 150 pg/s. The reason for the different peak shapes in different buffer gases is unknown. There could be several reasons for this phenomenon. First of all, the discharge parameters are different, even at the same flow, pressure and voltage. The electron density in a helium discharge is known to be one order of magnitude lower than in an argon discharge, while the electron temperature is higher. Secondly, the masses of the plasma gas atoms are different, this results in the energy transfer collisions in an argon discharge being more effective than in a helium discharge. Furthermore, the adsorption and desorption of analytes from the walls is probably different for the two plasma gases since the temperatures at the wall are not the same. In an argon discharge the constricted zone of high excitation is closer to the temporary cathode and with this to the discharge wall. This results in higher temperature and less desorption process, than in a helium discharge. The broad peaks are a major problem in the helium discharge because two neighboring peaks can overlap. A reduction of the width is desirable since the detection limits in helium are much better than in argon, and it is the same gas that is used in the GC. The Ar DBD has the problem of an unspecific absorption, already reported in an earlier publication [Mic01], that gives rise to higher noise and detection limits. If the peak tailing in helium is due to the deposition of carbon on the discharge wall, the addition of oxygen (so called scavenger gas) to the plasma gas should keep the carbon volatile and, therefore, prevent carbon deposition. As a result, the resolution should improve. However, the addition

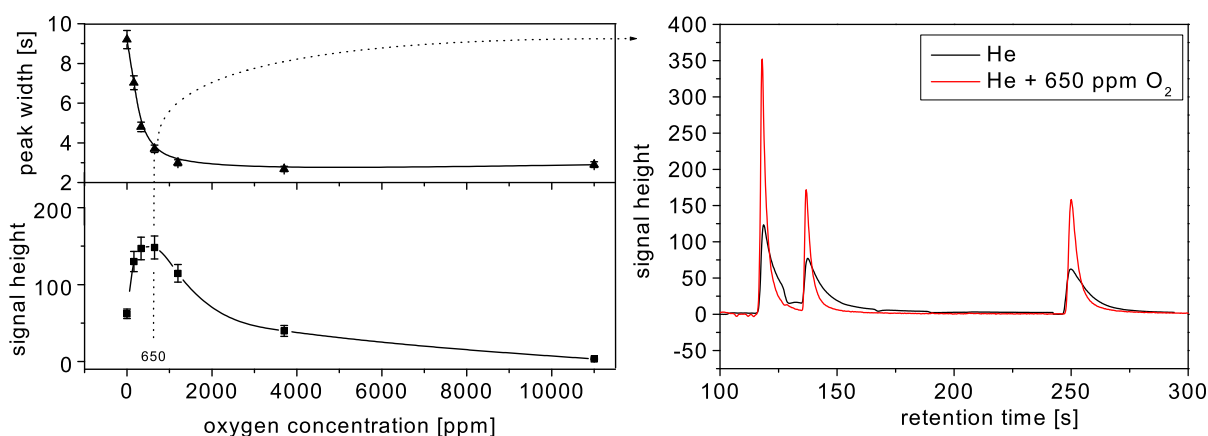


Figure 4.27: left: Signal widths and height of C_4H_8BrCl on the oxygen concentration; right: Cl chromatogram in pure helium and He with an addition of 650 ppm O_2 .

of oxygen could lead to collisional quenching of the excited states and, therefore, to a decrease of sensitivity for the halogens [Dal77]. The dependence of the DLAAS signal height and width on the amount of oxygen in a helium discharge is shown in figure 4.27. The amount of scavenger gas was decreased starting at 1 percent. By adding oxygen, the peak not only narrows and, therefore, increases the resolution but also increases the sensitivity in a small range. A concentration of about 600 ppm increases the signal height by a factor of 2 to 3, while the width is reduced by approximately the same amount (right hand side of figure 4.27). With 600 ppm oxygen a detection limit of 60 pl/ml was found for C_4H_8BrCl which was three times better than without the scavenger gas. Addition of oxygen to the Ar DBD had no influence on the shape of the signal, but decreased the amplitude of the DLAAS absorption signal, mainly by quenching of the excited states. To my knowledge an increase of signal amplitude in chromatograms by the addition of oxygen was not reported so far, while an increase in selectivity is well known. It is assumed that the carbon deposition on the wall is reduced by the formation of CO. Therefore, the adsorption of halogen atoms on the walls of the discharge is lower and pronounced peak tailing is avoided. Furthermore, the absorption signal is higher because atoms stay in the plasma.

Comparison with other GC detectors Similar GC experiments with DLAAS detection were performed a few years ago using non-miniaturized plasmas [Zyb95]. The detection limits by double-modulation DLAAS were 0.12 pg/s and 0.25 pg/s in a microwave induced plasma and in a DC discharge, respectively. Recent atomic emission measurements using a microwave plasma and a miniaturized Echelle spectrometer gave detection limits of 95 pg/s chlorine in helium [Koc04]. A detection limit of 13 pg/s for chlorine has been reported for the commercial atomic emission detector (AED) G2350A

built by Agilent [Qui96]. Lately, Bessoth et al. published a Cl detection limit of 800 pg/s after applying their DC plasma on a chip and a conventional GC instrument [Bes02]. They also report on strong peak broadening. The detection limits obtained with the system reported are in the same order of magnitude or even better than those listed above. Therefore, the DBD can be regarded as a powerful and promising device for integration in μ TAS. However, some problems still remain to be solved, such as improvements in the peak tailing and the stoichiometry.

Emission measurements

DLAAS is a sensitive detection method employed in analytical spectroscopy, but it is limited to one or a few elements because the experimental setup becomes more complicated by using different laser diodes simultaneously. Nevertheless, this has been demonstrated by [Gro93]. Contrary, emission spectrometry is a powerful method for multi-element analysis, and coupling of a plasma source with such a detection is a much simpler arrangement. Following this idea, the dielectric barrier discharge was coupled with the echelle spectrometer described in section 3.2. Normally, the plasma is imaged with a lens onto the slit or the fiber of the spectrometer. However, it was observed that this does not result in an improvement of the detected light intensity compared to a setup with a fibre as close as possible to the channel. Probably the optical depth of the imaging cannot be larger than it is by direct measurements due to the aperture formed by the glass spacers on the side. Two echelle spectra of the dielectric barrier discharge operated in argon and helium with an admixture of CCl_2F_2 as analyte are presented in figure 4.28. The exposure time was 4 s in both cases and 10 spectra were averaged. The strongest emission lines of the rare gas and the detected chlorine and fluorine lines are marked. It is obvious that fluorine is not detectable in an argon discharge because the excited fluorine levels are higher than the first excited argon level. This was already noticed during the laser absorption measurements. Additionally, impurities like oxygen, nitrogen and hydrogen are excited. Furthermore, the gradient of the diffraction orders of the echelle grating is visible by some saturated lines. It follows a slightly bended curve starting on the lower left going to the upper right hand side. Some lines are observable in two diffraction orders of the echelle grating, such as the helium 667.815 nm or argon 751.465 nm line. In order to obtain low detection limits for one element, the lines diffracted in different orders, as well as different transitions can be summed up. A further improvement is achieved by a binning of several pixels of the CCD during the read-out time of the detector. In this case, a specific amount of neighboring pixels is read-out at once, which increases the sensitivity since the read-out noise appears only once. Additionally, the dead time of the detector is reduced which is important for

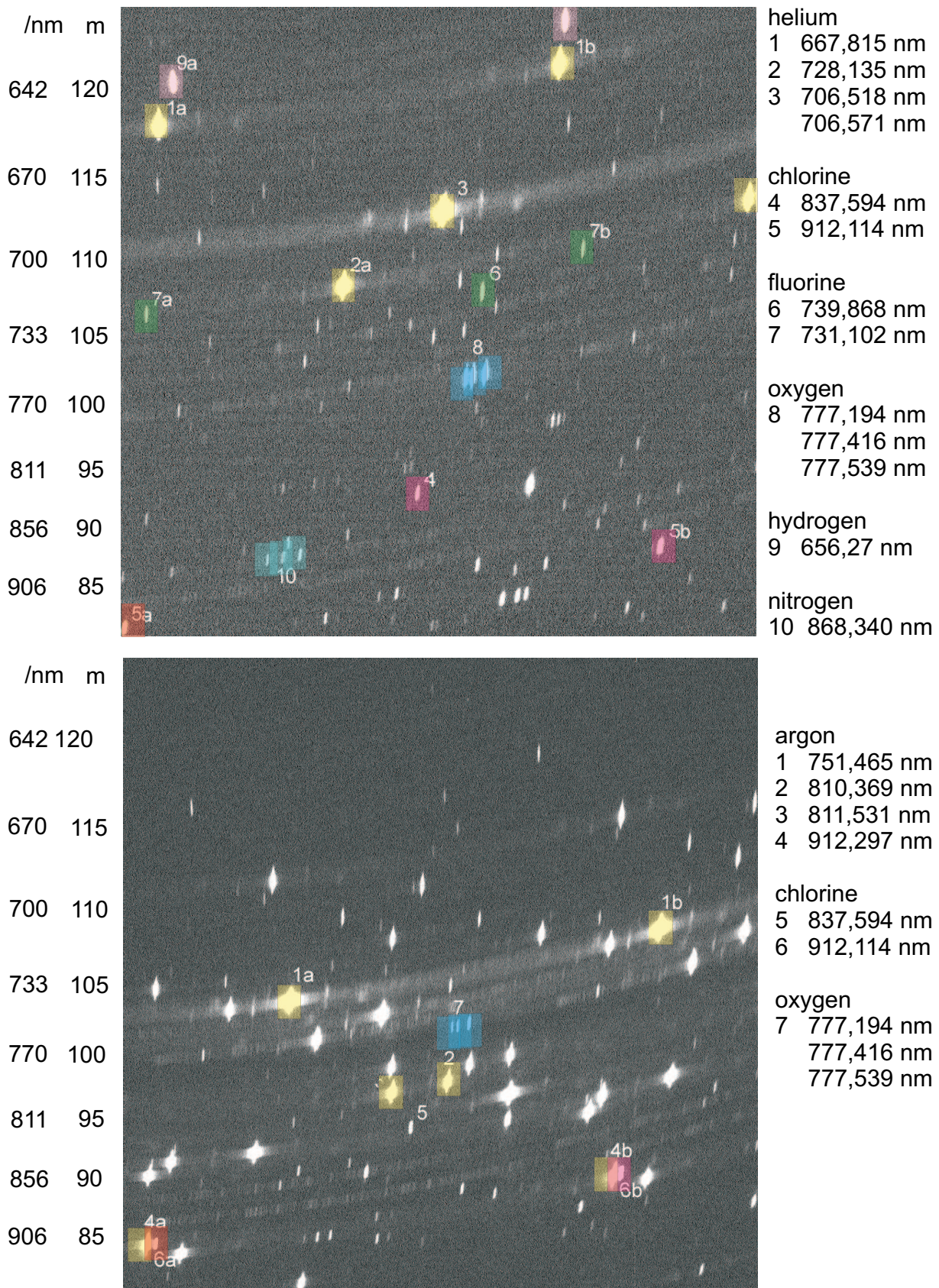


Figure 4.28: Emission spectrum of a DBD discharge burning in helium and argon with an admixture of 17.5 ppm and 190 ppb CCl_2F_2 respectively.

fast measurements, like the coupling with a GC shown in section 4.3.

The chlorine emission signal for 500 ppb CCl_2F_2 in helium is shown in figure 4.29.

A calibration curve results in a 3σ detection limit of 150 ppb. At first glance, this is not consistent with the signal-to-noise ratio at 500 ppb, but one has to take into account the nonlinearity of the calibration curve. The detection of fluorine was impacted by a contamination of the discharge wall. The detection limit in emission is obviously worse than for absorption spec-

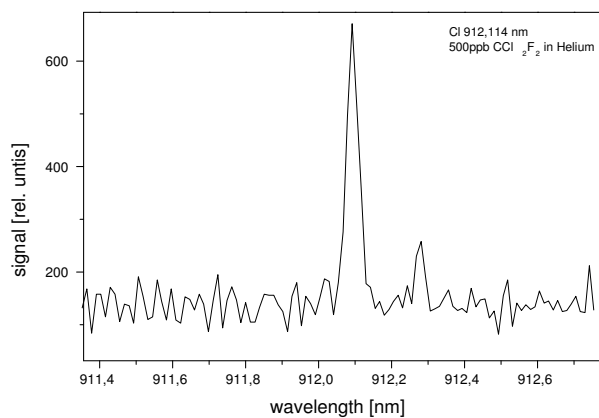


Figure 4.29: Emission signal of chlorine line.

troscopy, even though the time constant was higher. This can be explained by the fact that the discharge has a low emission efficiency, which can be overcome in absorption by a long absorption length. Furthermore, the emission volume is small.

4.3 High-pressure dielectric barrier discharge

For more simplified analytical devices, high-pressure operation is preferred because the vacuum system can be economized. Furthermore, high-pressure discharges have a higher density and, therefore, a higher excited state and electron density, and also a higher gas temperature. This would lead in turn to a more efficient dissociation and excitation. However, the disadvantage of high-pressure operation is a higher sputtering rate at the discharge electrodes, which makes it necessary to improve the design of the discharge. The dielectric barrier discharge presented operates in a streamer-like mode at atmospheric pressure, which strictly limits the lifetime of the thin dielectric layer. Therefore, the dielectric thickness has to be increased and, according to the similarity laws, the electrode distance has to be decreased. A very simple but, at the same time, successful design has been developed. The main idea was the use of a chromatographic column (inner diameter of several hundred micrometer) and two metal electrodes which are externally attached parallel to the capillary, each a few cm long. The most challenging task was the positioning of the electrodes without generating sparks on the outer part of the column, but igniting the discharge only inside the capillary. The thicker dielectric requires a higher voltage than can be obtained with the generator used previously. Therefore, a commercial high voltage supply for UV lamps was adapted to the experimental setup. The generator of

the *Hansen-Neon* company used in this setting offers a high voltage of 3 000 V and a current up to 20 mA with a frequency of 16 – 20 kHz, depending on the electrical circuit. Lower voltages are obtained by a potential divider, while the current is limited by a series resistance. The rare gases Ar and He were used as plasma gases. This discharge can be used for analytical spectroscopy, either as a source for emission spectroscopy or as a primary ion source for chemical ionization in combination with mass spectrometry.

4.3.1 Emission spectroscopy

The discharge was coupled with the echelle spectrometer described in section 3.2. The device was first tested with gas mixtures as in the case of absorption spectroscopy in the low-pressure DBD. Thereby the signal depends strongly on the applied voltage and the inlet pressure used, both changing the plasma conditions. The capillary was connected directly to the gas supply and the gas was flowing through the discharge into open air. This means that increasing the pressure in the discharge will increase the flow of the gas. Therefore, the increase of the signal with higher pressure is expected, as higher gas flow leads to higher particle density as well as less contamination and quenching.

The design of the discharge is suitable to use the plasma as an emission detector for gas chromatography. The discharge can be mounted directly at the end of a GC column, while it can be sustained only by the gas flow of the gas chromatograph. This makes the device easy to handle. Nevertheless, the small gas flow of the chromatograph deals also with the disadvantage of air diffusing into the discharge, leading to quenching and, therefore, lower detection capability.

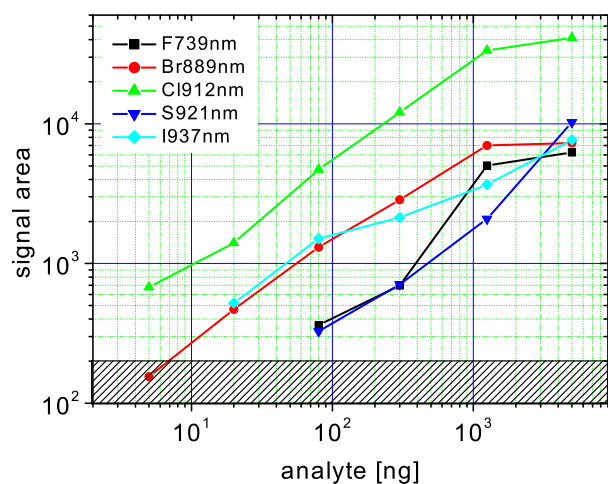


Figure 4.30: Calibration curve for the halogens in a He discharge.

Figure 4.31 shows a series of echelle spectra, taken at different eluent times using the same samples as in table 4.4. The lower part shows the signals of the different atomic emission lines. As it can be seen, the molecule can be well determined from the different elemental components. Peak broadening, as it was observed in the low-pressure dielectric barrier discharge (see section 4.2.2), was not noticed. This might be due to the presence of air and, consequently, quenching of the excited molecules. A calibration curve, plotted in

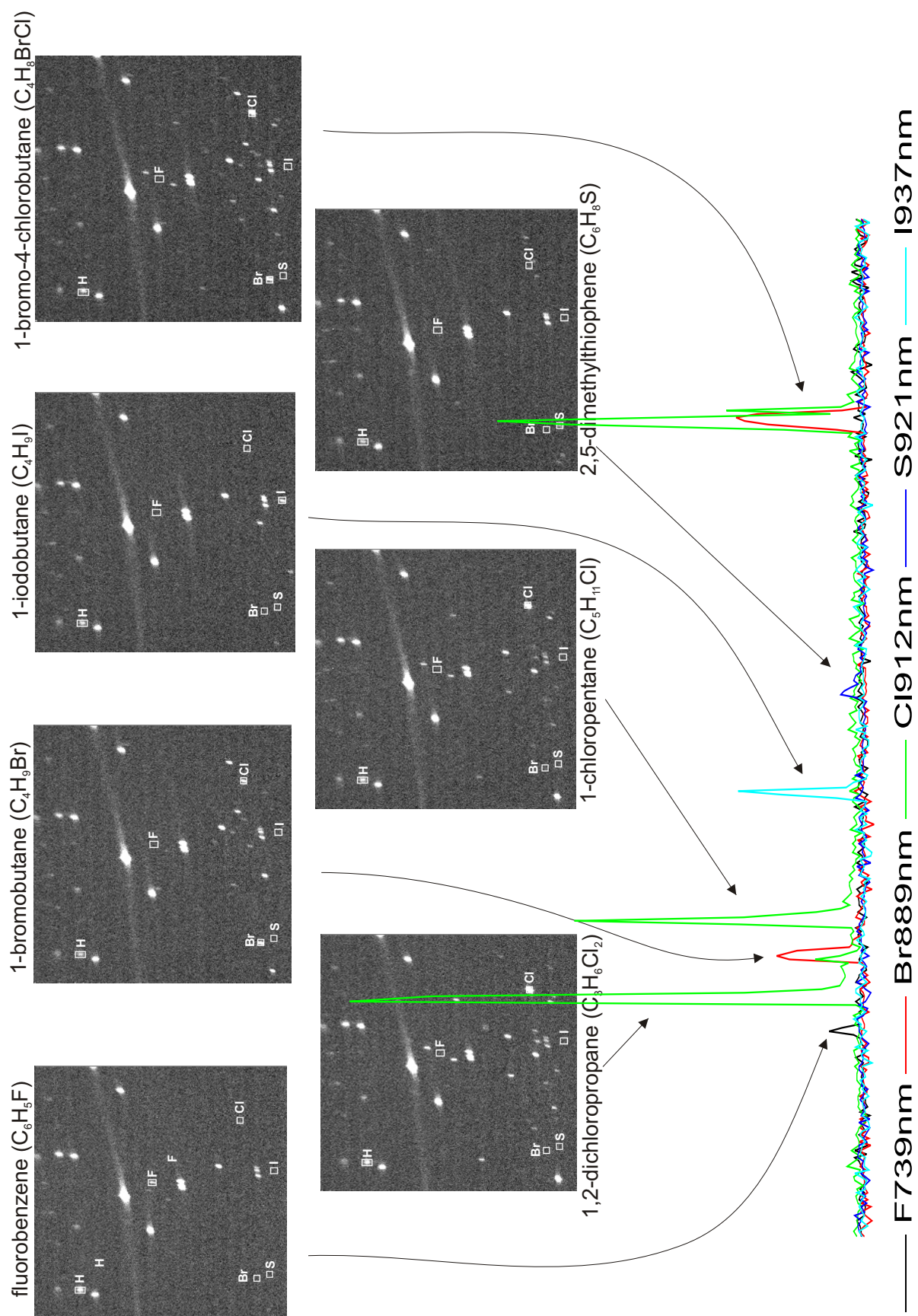


Figure 4.31: Chromatograms obtained on the five element lines Cl, F, Br, S and I (lower part) and the corresponding echelle spectra of a He discharge.

figure 4.30, is linear over almost three orders of magnitudes (at least for Br and Cl), resulting in absolute detection limits of several ng. Despite the higher applied voltage these values are much worse than those obtained with DLAAS in the low-pressure discharge and also not comparable with the emission measurements in the same discharge. Probably, the discharge is too weak, because the coupling of the electrical power is not optimized and power is lost on the outside by additional sparking.

4.3.2 Ionization source

First attempts to use the high-pressure dielectric barrier discharge as ionization source for atmospheric pressure chemical ionization (APCI) were also performed. Commonly, a corona discharge is used as primary ionization source, whose gas ions ionize subsequently the analyte of interest. In this case, the ionization is weak which means that almost no fragments are observed. Normally, the configuration consists of a needle-plate geometry, having a distance of a few cm and applying a voltage of several kV with a current of μA between the corona needle and the inlet of a mass spectrometer, which is used as a detector. The APCI is a versatile arrangement for detection of gases, aerosols or molecules produced by laser desorption. The high-pressure dielectric barrier discharge seems to fulfill the requirements for an APCI, since it is very flexible. The capillary can be pointed more precisely than the corona discharge at the position of analyte investigated. Preliminary measurements were performed with the same setup comparing a commonly used corona discharge and the DBD. In this case, the total ion current of both ionization sources were similar, but in the case of the DBD more fragments were observed. Nevertheless, the detection power does not differ too much, which provides the DBD as another source for APCI. This topic is subject to further investigations.

The micro hollow cathode discharge

5.1 Generalities about micro hollow cathode discharges

5.1.1 Principle of the (micro) hollow cathode discharge

A hollow cathode discharge consists of a hollow structured cathode and an arbitrarily shaped anode (see figure 5.1). Commonly, the cathode is made up of a hole, while the anode is shaped cylindrically; both are separated by a dielectric spacer. The cathode can be a cavity in a solid metal block, but in the present study it will be a bore, which is possible as well.

For a specific value of pD , the product of pressure p and diameter D , different modes of the discharge can be observed in the current-voltage characteristic. At low currents (figure 5.1, I_1), a kind of glow discharge can be observed with a cathode fall outside the cathode structure. An axial electrical field between cathode and anode is generated.

By increasing the current (I_2), the the positive column moves closer to the cathode until it enters the hole. In this case (I_3), the positive space charges in the middle of the bore can be regarded as a virtual anode. The direction of the electrical field is changing from a transversal into a radial one. This leads to an oscillatory motion of the negatively charged particles. Electrons generated at the cathode are accelerated towards the virtual anode in the middle

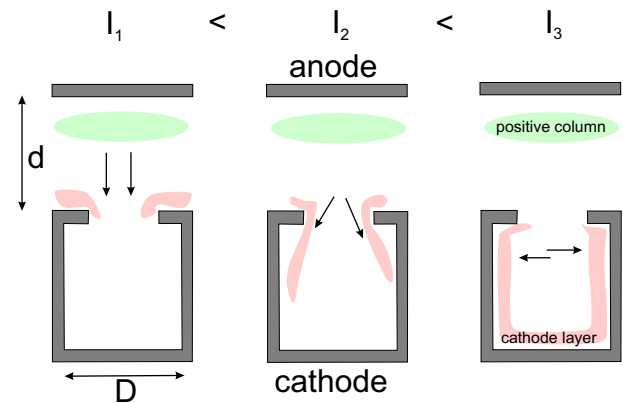


Figure 5.1: Space charges and electrical field in the hollow cathode discharge for different currents.

and repelled at the opposite cathode fall. Then the process is repeated by acceleration and repelling again. In this way, electrons are kept in the discharge for a long time and can ionize and excite various times. This “pendulum effect” causes a decrease in the voltage at an increasing current, which results in a negative differential resistance. With a further increase of the current, a normal glow regime is obtained with a constant voltage.

Finally, if the whole cathode surface is covered by the cathode layer, a further increase of the current results in an increase of the voltage.

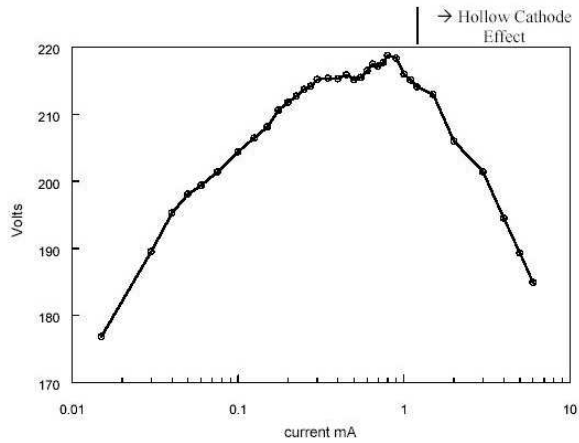


Figure 5.2: *I-U-characteristic [Kur03].*

is a function of pD . A lower limit of pD is given by the fact that the mean free path for ionization should not exceed the hole diameter. For rare gases, this value is around 0.04 mbar·cm [Kur03]. The upper limit is determined by the condition that the sum of the two cathode falls and the glow region should be larger than the distance between the two opposite cathode surfaces. The limit obtained empirically of 14 mbar·cm is by a factor of 10 higher than the theoretical one. One possible explanation for this discrepancy could be that the theoretical calculation was based on a wrong assumption with respect to the amplitude of the pendulum motion. This motion can be observed even before the two negative glows merge.

This reflection implies that an atmospheric pressure hollow cathode discharge needs hole diameters of about 10 μm . Nevertheless, stable operation at bore sizes of 250 μm could be observed as well. This indicates that other mechanisms, apart from the pendulum motion of the electrons, have to be considered for a more detailed model.

The distance d between anode and cathode does not contribute to the considerations mentioned above, but this distance determines the breakdown voltage according to the Paschen law. Empirically, it is given for rare gases as 200 – 400 V for reduced pd values of 1 – 10 Torr·cm.

The secondary electron emission at the cathode surface, the Penning ionization and multistep processes are other mechanisms contributing to the high ionization efficiency in

The negative resistance can be observed in the current-voltage characteristic plotted in figure 5.2. Even if all the plasma modes mentioned can be observed in a hollow designed geometry, usually, the term “hollow cathode discharge” is used only for the mode of pendulum electrons, case in which resistance is negative.

This effect occurs for a specific range of pD^1 values. Hollow cathode discharges follow a similarity law called after Allis and White [Whi59, Stu64], whereas the voltage

¹Note: D is the diameter of the hole, not the distance d between the electrodes as in Paschen law

hollow cathode discharges. The plane discharge geometries that are usually used lead to losses of non-charged particles due to collision with the walls and the anode. In the hollow cathode configuration, they will more probably strike the cathode resulting in a higher secondary electron emission. At the same time, the configuration and the higher current density lead to an increase of the sputtering rate, so Penning ionization of noble gas atoms and sputtered electrode material occurs. Ultimately, the high plasma density favors stepwise ionization, which also contributes to the rise of ionization efficiency.

Design of discharge

The design of the micro hollow cathode discharge (as it was also investigated in the current work) is sketched in figure 5.3. Cathode and anode are made by metal; frequently used materials are Cu, Ni, Pt or W, whereas the insulator is made of Kapton, Mica or ceramic. The thickness of the electrodes and the dielectric d is 20 – 150 μm and 10 – 500 μm , respectively. It is common to chose the same thickness for the anode and the cathode, although it is not necessary. The bore D in the structure is 100 – 300 μm wide.

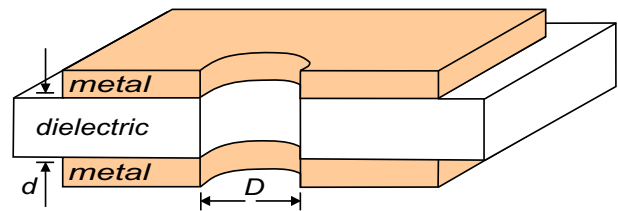


Figure 5.3: Schematic outline of the MHCD.

This structure can either be fabricated by mechanical pressing, bonding of the different materials or by depositing the metal by galvanization or thick film technology onto the insulator. The preparation of the bore depends on the hardness of the materials and it can either be made mechanically, by using carbide metal and diamond drillers, or by lasers ablation.

By using an ac or dc current, a plasma is produced inside the hole between the electrodes in noble gases, rare gas-halide mixtures or air.

5.1.2 Applications of hollow cathode discharges

Micro hollow cathode discharges allow easy parallel operation, which makes them suitable for discharge arrays (see figure 5.4). In this way, larger areas can be illuminated or treated. A discharge array is produced in the same manner as a single discharge, but instead of one hole, several are drilled in the structure. Two modes are possible: (i) the voltage can be applied to the entire electrode; (ii) the discharges can be isolated electrically and each one driven by its own individual ballast. The strong inhomogeneous conditions in the micro hollow cathode discharge enable the emission of excimer radiation.

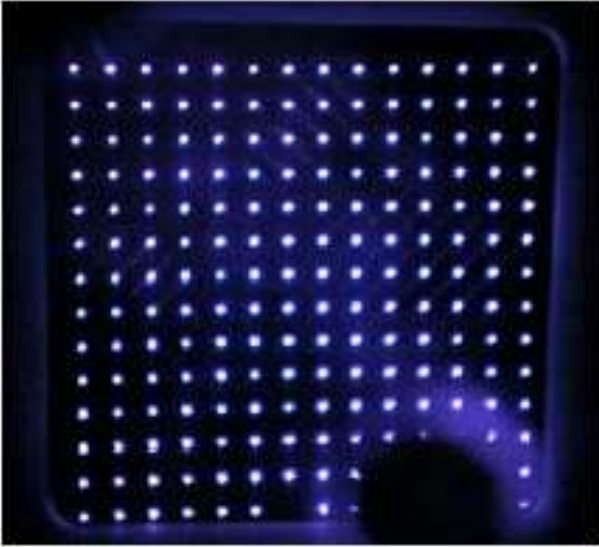


Figure 5.4: Parallel operated micro-discharges in argon at 200 mbar without resistive decoupling. Stable operation at low current [Pen02].

First, the electron energy distribution needs to contain a sufficient concentration of electrons with energies larger than the excitation energy of the excimer gas system. Second, since the formation of excimers is a three-body process, the pressure needs to be in the order of one atmosphere or higher [Sch00]. Hence, several research groups worldwide are investigating and developing this discharge as excimer lamp successfully.

The other potential application area of hollow cathode discharges is the surface treatment. As it was shown by Penache et al. [Pen01], micro hollow cathode discharge

arrays can be used to change the wettability of a surface, for example.

5.1.3 Diagnostics so far

Up to now, intrinsic parameters of the micro hollow cathode discharge are not very well known due to the small dimension of the device and the lack of appropriate diagnostic methods. Nevertheless, several research groups applied different techniques during the last few years.

Penache [Pen02] investigated a micro hollow cathode discharge that is similar to the one used in this thesis. Excitation temperatures were determined by Boltzmann plots of emission lines in the range of 1 eV for the high-pressure MHCD in argon. The value was independent of the power that was applied.

Leipold et al. [Lei00] investigated a MHCD made of 100 μm thin molybdenum foils as electrodes, and a cathode hole size of 100 μm . The dielectric between the electrodes was alumina of 250 μm thickness. Infrared heterodyne interferometry revealed an electron density of 10^{13} cm^{-3} for direct current, atmospheric pressure discharges in air.

Hsu and Graves [Hsu03] used a design with a small hole (200 μm diameter) perforating two thin metallic foils (100 μm thickness) separated by a dielectric of 250 μm . They estimated peak electron densities in the order of $10^{12} - 10^{13} \text{ cm}^{-3}$, by using an ion flux probe outside the discharge for gas pressures in the order of several hundred mbar and

for applied powers of 1 – 10 W. Furthermore, the gas temperature was sized up by N₂ rotational bands to 2000 K for a NH₃ atmosphere.

Lately, Schönbach et al. [Mos03] measured electron densities in an atmospheric pressure argon discharge. The electrode material consisted of 100 µm molybdenum foils separated by a 250 µm alumina layer. A plasma operated either with pulsed or dc voltage was ignited in the hole with a diameter of 130 µm. For DC operation, electron densities of 10¹⁵ cm⁻³ were measured by evaluating the Stark broadening of the H_β line. The electron density increased to values beyond 10¹⁶ cm⁻³ for nanosecond pulsed operation. This increase in electron density and excimer emission intensity was explained by pulsed electron heating, an effect that has raised the mean electron energy from 1 eV, for DC operation, to 2.25 eV in the pulsed mode.

These findings show that the measured quantities vary strongly; they are dependent on the design of the discharge, the gas and pressure applied as well as on the determination method. Many measurements were performed indirectly, and the rotational, vibrational and excitation temperatures can only give a rough upper limit of the gas temperature. Only in LTE discharges these values will be identical. Furthermore, the electron density is often determined by indirect parameters, too, like current, assuming Ohm's law and a uniform electric field, or probe measurements outside the discharge volume. In this way, values as different as 10¹³ to 10¹⁵ cm⁻³ are obtained. Therefore, the knowledge of the intrinsic discharge parameters of the MHCD is still uncertain and contributes to a better understanding of the discharge mechanisms.

5.2 High-pressure micro hollow cathode discharge

5.2.1 Characterization of the discharge

The principal design of the discharge was already presented in figures 2.12 and 5.3. An insulator of several hundred micrometer thickness is sandwiched between two metallic electrodes and a hole is drilled through the setup.

During this work three different structures with different materials and fabrication processes were used. Both structures shown in figure 5.5 use some kinds of Al₂O₃ as insulator. The type on the left hand side was fabricated by *CeramTec* and has an overall thickness of 650 µm, the insulator being 250 µm thick and the Cu electrodes 200 µm each. The thickness of the copper electrodes was reached by deposition followed by galvanization. Finally, the copper was coated with a 5 µm thick Ni film for passivation. The holes were

laser-drilled by the *Laserzentrum Hannover* using a high intensity ultra short pulsed laser. The diameter of the holes was chosen to be about 100 μm and, usually, their shape is single-conical with about 15 – 20 % difference between the entrance and the exit side of the laser beam. The lifetime of this structure is limited by the high sputtering rate of copper. Better electrode materials, like tantalum, tungsten, molybdenum or platinum are more resistant against sputtering processes or high temperature.

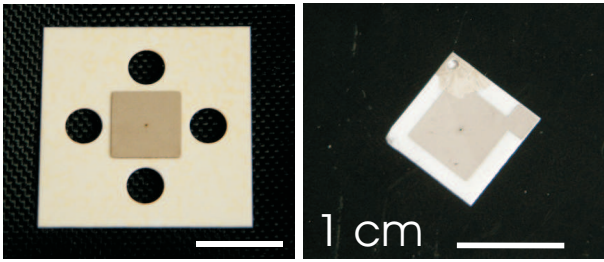


Figure 5.5: Photos of MHCD structures.

The MHCD structure on the right hand side of figure 5.5 is a combination of platinum and alumina layers. It was provided by the *IKF Frankfurt* and it is produced by another technique, using the so-called “green ceramics”. The non-sintered ceramic substrate is covered by the metal paste desired (here 20 μm Pt) using the

so-called screen-printing method. In this stage of the process, the product is still flexible and the holes can be drilled mechanically. Afterwards, the composite sheet is sintered at a temperature of about 1800 K, in which the polymer binder is burned out and the ceramic itself sintered. Both the maximum thickness of the electrodes and the minimum thickness of the insulator are limited by the manufacturing procedure to about 25 μm and 100 μm , respectively. A third method is based on thick-film-technology and was offered by the *Transferzentrum Mikroelektronik* in Göppingen. With this technique a layer of 20 μm can be deposited at once on the alumina structure and the process is repeated as many times until the desired thickness is reached. In this way, different thicknesses of the platinum can be obtained in the same working process. Taking into account the hardness of the material, the holes had to be drilled by laser drilling. The optimization process for the right laser conditions was developed and performed by *Laserzentrum Hannover*, too. Some pictures taken with SEM of the holes are presented in figure 5.6. The two holes on the left (a,b) and right (c,d) hand side were both supposed to be 200 μm and 100 μm ,

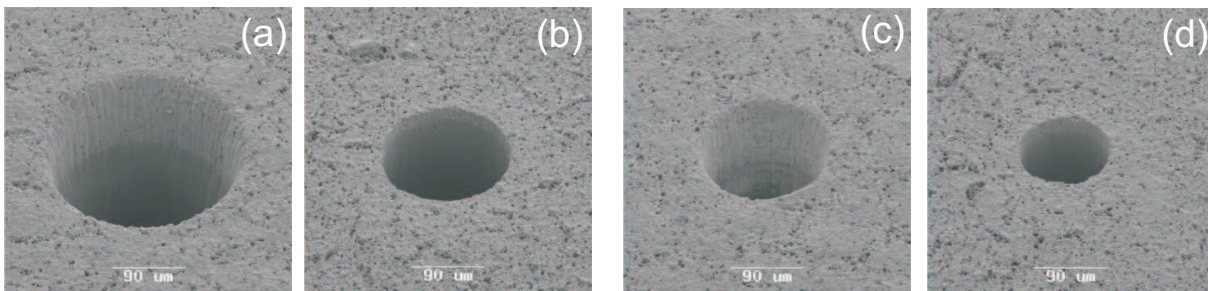


Figure 5.6: Pictures taken by SEM for different laser conditions; a,b: 200 μm hole, c,d: 100 μm hole [Kam04], scale of 90 μm is marked.

respectively. The holes (b) and (d) show a cylindrical hole. On the contrary, inferior conditions for laser drilling results in conical holes as shown in (a) and (c). Different diameters in the two different materials, dielectric and platinum, are observed. All kinds of laser drilling deal with this disadvantage that the holes never have the same diameter at inlet and outlet of the laser beam. In some cases the difference in diameter is 30 %.

Optical measurements

The optical appearance of a MHCD with relatively large diameter of 300 μm at medium pressures is shown in figure 5.7. In the low-pressure case, the discharge is widely expanded like a sphere at the cathode side of the hole. This is due to the fact that the cathode surface has to be larger than the inner surface in order to sustain the discharge. At high-pressure, the discharge is constricted in the hole, which is also visible by the dip on the end-on view. The cathode fall and the negative glow are very small (in the μm range) and, consequently, the production of electrons and excited atoms is closer to the walls of the structure.

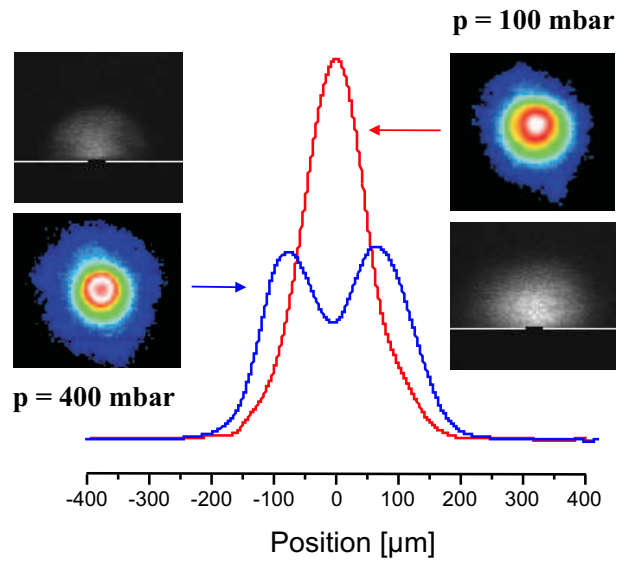


Figure 5.7: End-on and side-on CCD recorded images of the cathode side of an Ar MHCD at different pressures, bore diameter 300 μm .

Electrical characteristics

The breakdown voltage of the micro hollow cathode discharge is, in accordance with the Paschen law, between 200 and 250 V. The current is limited by a 100 k Ω load resistor, placed in series with the discharge. The gas voltage was measured with a conventional multimeter. The current-voltage characteristic of the discharge is given in figure 5.8. It can be seen that the gas voltage is almost constant by variation of the current. This means that the discharge is not working in the so-called hollow-cathode regime anymore. Furthermore, the voltage increases with the pressure. The sustaining voltage in an argon discharge is slightly higher than in a helium discharge, which is in agreement with the Paschen law (figure 2.1). The gas voltage is constant and does not exceed 250 V at atmospheric pressure. For the given geometric parameters and a current of 6 mA, the current density

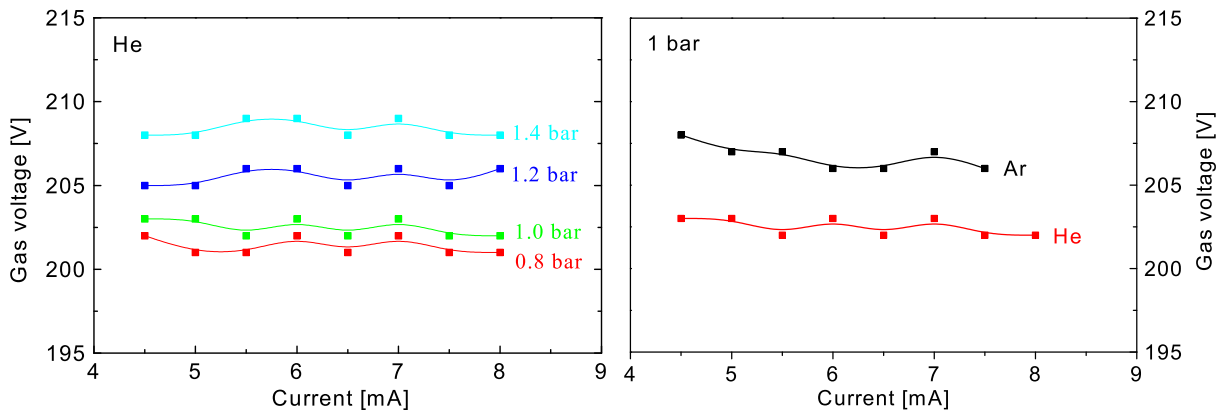


Figure 5.8: Current-Voltage characteristic for different gases and pressures.

and the input power density are about 60 A/cm^2 and 1 MW/cm^3 , respectively. Note that the power density of a MHCD is 3 orders of magnitude higher than that of an ICP (see section 4.2.1).

Determination of gas temperature and electron density by laser spectroscopy

Principle of measurement for low-pressure The determination of plasma parameters should always be non-invasive, like it was shown for the dielectric barrier discharge. The laser diode beam interacts with the discharge but does not disturb it.

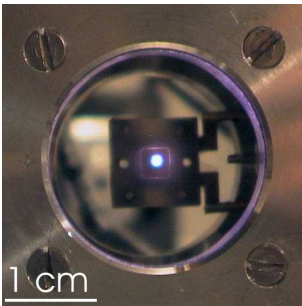


Figure 5.9: Picture of the Ar MHCD.

However, high spatial resolution measurements in the micro hollow cathode discharge are nearly impossible considering the very small dimensions (see also photo 5.9). Therefore, this investigation will be restricted to the determination of plasma parameters in the hole itself. It has to be kept in mind that the obtained values are averaged over the distribution of the excited species, which is shown in figure 5.7. As was shown at high-pressure, the hot region of the plasma is close to the outer diameter of the bore (see figure 5.7), whereas at low-pressure the highest concentration is located in the middle of the bore. As for the dielectric barrier discharge, the plasma parameters can be measured by line profile analysis investigating the width of the spectral lines. This was performed in the low-pressure range from 50 to 400 mbar, where line broadening determination is still feasible.

The measurements were performed with the same laser diodes as in section 4.2.1, probing the argon lines 801.699 nm ($1s_5 - 2p_8$), 826.680 nm ($1s_2 - 2p_2$) and 800.838 nm ($1s_4 - 2p_6$). The beam of one laser diode was adjusted through the hole of the structure as

The measurements were performed with the same laser diodes as in section 4.2.1, probing the argon lines 801.699 nm ($1s_5 - 2p_8$), 826.680 nm ($1s_2 - 2p_2$) and 800.838 nm ($1s_4 - 2p_6$). The beam of one laser diode was adjusted through the hole of the structure as

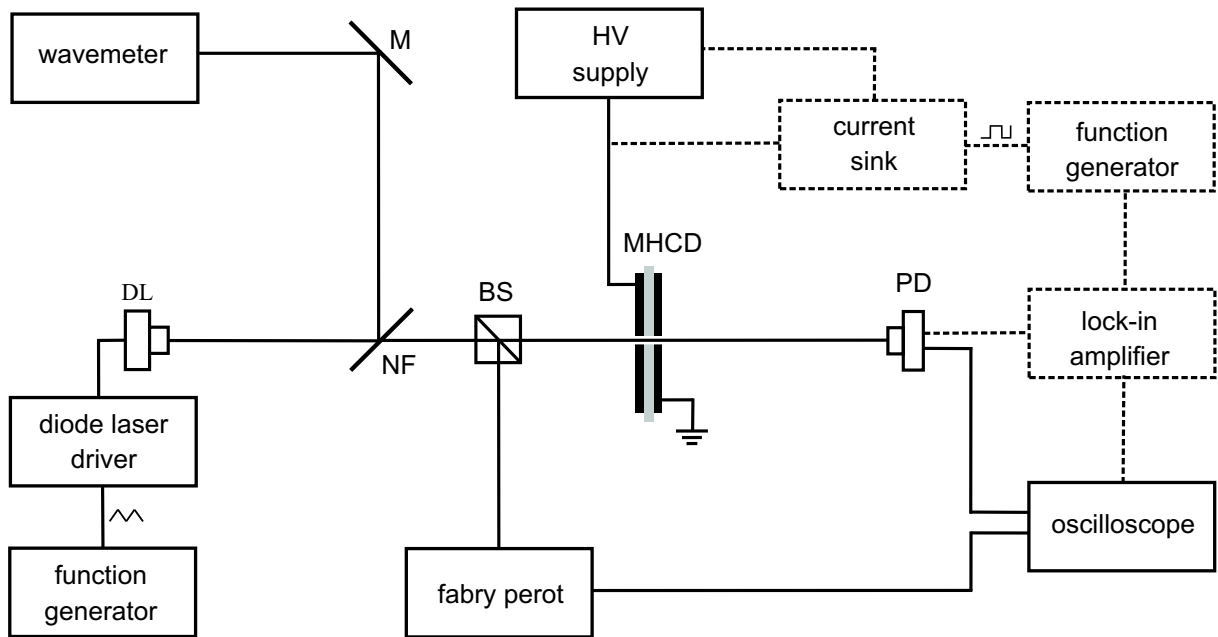


Figure 5.10: Experimental arrangement for plasma diagnostics.

shown in figure 5.10, and the absorption signal was detected by a photodiode. The current through the discharge was modulated with several hundred Hz in order to increase the detection sensitivity by phase selective detection. A beam-splitter (BS) and a neutral density filter (NF) were used to pass a part of the beam to a wavemeter and Fabry-Perot interferometer (free spectral range of 2 GHz) in order to determine the wavelength, and to generate a frequency standard for precise measurements of the absorption linewidths. For the present experiment at low-pressure, structures with 130 μm and 50 μm thick copper electrodes and Kapton insulator, respectively, have been used. The diameter of the holes was 300 μm .

The absolute number density of the excited atoms was determined by the integral absorption. The evaluation is rather difficult, because the absorption length cannot be determined precisely and the plasma is inhomogeneous. As it can be seen from figure 5.7, the excited atoms are not uniformly distributed in the discharge. Furthermore, the optical appearance of the microdischarge changes with the pressure, i.e. at 50 mbar the light emission shows a maximum on the discharge axis, while at 400 mbar it shows a minimum. As absorption occurs inside the MHCD hole and above the cathode as well, a minimum and a maximum absorption length were considered.

For calculating the absolute number density, the maximum value for the total absorption length was taken as the sum of the length of the bore and the plasma length outside the hole. The plasma length outside the hole was evaluated from spatially resolved absorption

measurements above the cathode. It was taken as the distance from the cathode surface to the point where the absorption signal decreases to approximately 10 % from its maximum value. The minimum absorption length was taken as the sum between a third of the hole length and the distance from the cathode to the point where the light intensity diminishes to 20 % from its maximum value. As an example, at 50 mbar the maximum and the minimum absorption length considered were 1100 μm and 600 μm , respectively. At 400 mbar the maximum is 300 μm and the minimum 50 μm . Furthermore, if only an effective absorption area is considered, the absolute number density is increasing by a factor of two. Under these conditions, the errors in determining the absolute number density are in the range of about $\pm 50\%$.

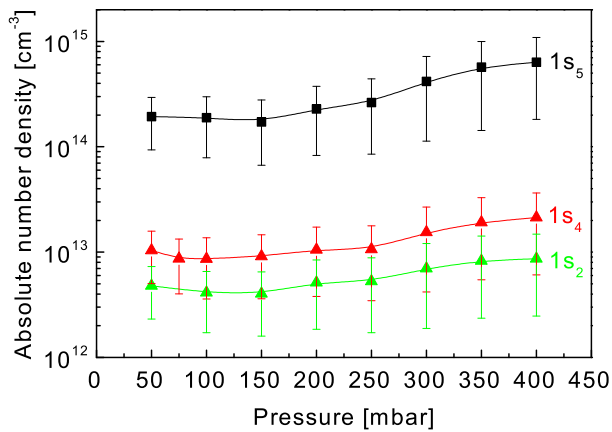


Figure 5.11: Absolute number density of the $1s_2$, $1s_3$ and $1s_4$ excited levels of Ar in the MHCD for the pressure range 50 – 400 mbar.

Figure 5.11 presents the variation of the absolute number density with the pressure for three of the first four excited levels of Ar. In the pressure range 50 – 400 mbar the absolute number density values are varying from $1.9 \cdot 10^{14}$ to $6.3 \cdot 10^{14}$ cm^{-3} for the lowest $1s_5$ level and from $4.8 \cdot 10^{12}$ to $8.8 \cdot 10^{12}$ cm^{-3} for the highest $1s_2$ level. Within this relatively high uncertainty it can be seen that the density is slightly increasing with the pressure mostly due to the rise in the density.

It should be stressed that inside the hole of the MHCD both the production and the destruction of excited states are very efficient. Owing to the high current density, a large number of excited atoms is produced, especially in the negative glow adjacent to the cathode. Since the geometrical dimension of the hole is small, diffusion becomes important in the destruction of the excited species in spite of the high-pressure. The excited atoms can easily reach the walls of the hole where they are strongly quenched. Other processes that are responsible for the depopulation of the excited levels are the two- and three-body collisions, whose importance rises with the pressure. In the region outside the hole, the density of charged particles is lower than inside the hole, and it is expected that only a small fraction of excited atoms is produced by electron impact. The plasma volume above the cathode surface can be considered a spatial afterglow. In this case, the excited atoms are mostly created in recombination processes and by photo-excitation or absorption of the resonance radiation escaping from the hole.

The destruction mechanisms above the cathode are partially different: the depopulation of the excited levels occurs mostly by volume processes, like two- and three-body collisions and quenching due to impurities. Indeed, by measuring without gas flow through the chamber it was observed that the density of excited atoms is strongly decreasing in time. The line profiles were evaluated with the same technique as presented in section 4.2.1. This evaluation reveals the gas temperature and the electron density. First, the Lorentzian part of the linewidth was determined for the wing of the line. Then, the Gaussian width was calculated according to equation 3.13. This evaluation was restricted to the two lines at 800 and 801 nm, since all lines starting from the $1s_2$ level are too broad to tune the line profile completely with the present laser diodes.

As seen in figure 5.12, the gas temperature obtained from the Gaussian width increases almost linearly with the pressure up to 1100 K at 400 mbar. It can be observed that there is a good agreement between the data obtained from the two transitions, which gives confidence in the accuracy of the results. By increasing the pressure, the electron mean free path reduces, the electrons gain less energy between collisions and are transferring more energy to the gas. As the power input in the discharge is constant and the plasma volume is decreasing with the pressure, it results in a higher current density and, consequently, to a more pronounced heating of the gas. Note that the gas temperature corresponds to the plasma region with the highest population density. Thus, for pressures higher than about 200 mbar these measurements represents the gas temperature of the discharge confined inside the hole of the MHCD.

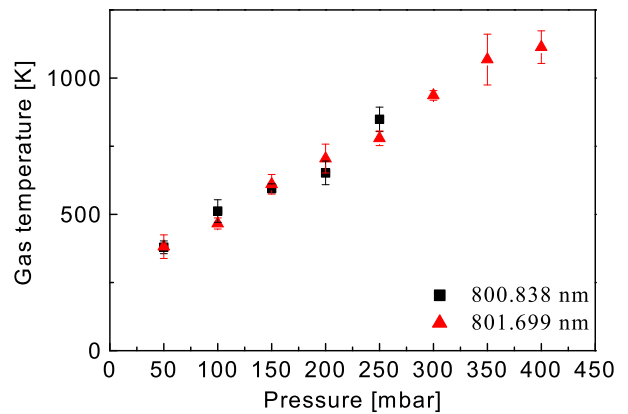


Figure 5.12: Gas temperature in the microdischarge derived from the $1s_5 - 2p_8$ and $1s_4 - 2p_6$ transitions as a function of pressure at constant current.

The Lorentzian width consists of pressure- and Stark-broadening components. The width induced by collisions can be calculated by the values found in the literature, e.g. [Cop76b], taking into account the gas temperature. For both transitions under investigation a significant difference between the total Lorentz width and the collision broadening width was observed. This difference is assigned to the quadratic Stark effect and can be described by equation 4.11.

As expected, the central wavelength of the transition from the metastable $1s_5$ level is additionally shifted. This shift increases with the pressure, due to interaction with neutral

(collisional) and charged (Stark) particles. In the case of the transition from the resonance $1s_4$ level, the line shift is very small (less than 1 pm at 50 mbar) and it does not depend on the pressure.

Subtracting the collision contribution from the total Lorentz width and shift, the electron density was estimated from 4.11 and

$$\Delta\lambda_{Stark}^{shift} = (d/w + 2 \cdot 10^{-4} \sqrt{N_e} \alpha (1 - 0.068 \frac{\sqrt{N_e}}{\sqrt{T_e}})) \cdot 10^{-16} w N_e, \quad (5.1)$$

using the Stark broadening parameters listed in table 4.3 and 5.1.

T	5 000 K	10 000 K	20 000 K
w	0.037	0.049	0.065
d/w	1.630	1.340	0.990
α	0.038	0.031	0.025

Table 5.1: Coefficient for Stark broadening given in Angstrom, $\lambda=801.699$ nm[Gri64].

The electron temperature was assumed to be about 1 – 2 eV taking into account the results presented in [Mos03] and section 2.1. A small variation of this value has no significant influence on the calculated electron density. The electron number density cannot be given very accurate because different values of the collision width and shift could be found in literature (see table 7.2 in the appendix).

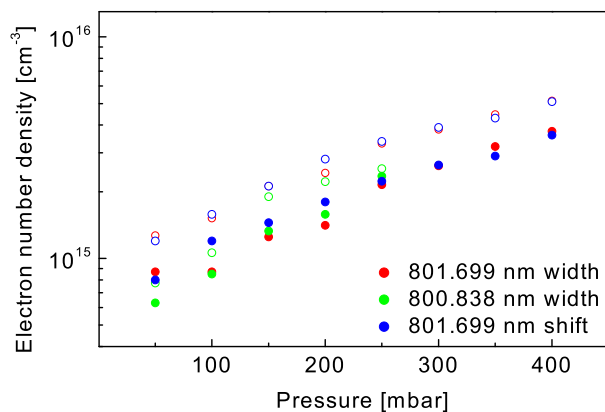


Figure 5.13: Electron number density in the microdischarge derived from the $1s_5 - 2p_8$ and $1s_4 - 2p_6$ transitions as a function of pressure at constant current.

The range of electron density is presented in figure 5.13, whereas the values of the collision broadening parameters were taken from different publications (open and closed data points). It can be seen that the electron number density is increasing by a factor of 5 in the pressure range between 50 – 400 mbar. The present measurements refer to the electron number density in the discharge area, i.e. inside the MHCD hole.

Taking into account the density of neutral atoms and the electron density, it can be concluded that the degree of ionization in

the MHCD is about 10^{-3} . The variation of these values depend strongly on the uncertainty of the broadening coefficients for impact broadening and the discrepancy between different authors.

Principle of measurement for high-pressure Unfortunately, the method presented is not adaptable to high-pressure discharges. First of all, the line profiles are 10 – 20 times broader because of the linear increase of the line broadening with the pressure. This implies that laser diodes with a large tuning range (100 pm) has to be used. In order to determine the line width, the tuning should be few times the widths. Free running laser diodes might be sufficient, but owing to the limited wavelength disposability, external feedback diodes has to be used that are not tuneable in such a wide range. Secondly, the deconvolution of the line profiles is difficult because the Gaussian width is much smaller than the Lorentzian one.

Therefore, sticking to laser absorption spectrometry one has to switch to line shift measurements. As was already shown above, the line shift reveals also the information on electron density and gas temperature. It is obvious that for the determination of two unknown quantities two measured values for the same plasma conditions have to be obtained. This task is fulfilled by measuring the line shift for different transitions.

In principle the line shift is given by the sum of pressure and Stark shift:

$$\Delta\lambda = \Delta\lambda_{Ar} + \Delta\lambda_{Stark} \quad (5.2)$$

$$= \beta_{Ar-Ar} N_{Ar} + \Delta\lambda_{Stark} \quad (5.3)$$

β_{Ar-Ar} shift coefficient

N_{Ar} Ar density

While the second term depends only slightly on the three investigated transitions (10 % variation), the first one varies strongly with the chosen transition. Therefore, in a first approximation the difference between two line shifts will be the difference of the corresponding collision shifts. This results in the gas density, and according to the ideal gas law in the gas temperature. Considering the possibility of obtaining different wavelengths with the ECDLs, a few transitions were used for this measurement. The figure 5.14 shows for a constant pressure the collision induced shift depend

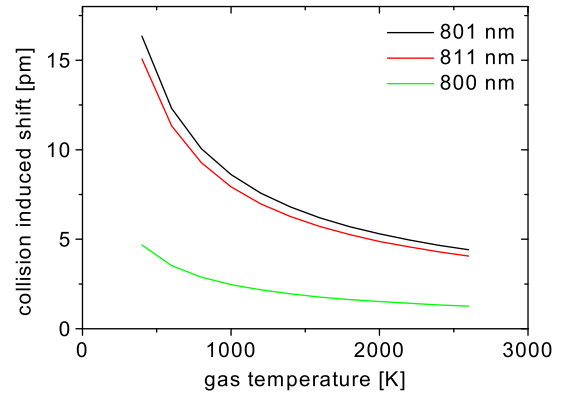


Figure 5.14: Collisional induced shift for 1 bar.

on the gas temperature. While only a small difference occurs for the shift between the two lines of the metastable states, a significant variance is visible between one transition starting from a metastable level and the one starting from the resonance level (800 nm).

Knowing the gas temperature one can estimate the electron density by subtracting the pressure shift corresponding to the obtained gas temperature from the experimental shift. This is a recursive procedure. Indeed, there exists a small deviation in Stark shift for the two lines that has to be taken into account in the following approximation. Knowing the difference for the specific electron density, a second loop can be started, determining again gas temperature and electron density. In principle after two iterations the correct values should be obtained.

This procedure is appropriate for gas mixtures, too. Discharges in He are normally better for analytical spectroscopy, but plasma diagnostics is more difficult. In the visible or infrared region only few lines are achieved by laser diodes. In the case of gas mixtures the pressure broadening is the sum of the foreign and self-broadening, but the principal evaluation is the same:

$$\Delta\lambda = \beta_{Ar-Ar}N_{Ar} + \beta_{Ar-He}N_{He} + \Delta\lambda_{Stark} \quad (5.4) \quad \left| \begin{array}{ll} \beta_{Ar-Ar/He} & \text{shift coefficients} \\ N_{Ar/He} & \text{density} \end{array} \right.$$

The accuracy of this method is given by the experimental error of the shifts measured as well as the spreading of the shift coefficients in the literature. Those for argon are given in the appendix (table 7.2) measured by different authors. It is obvious that the procedure contains large errors as a result of the variance of the data. According to the Lindholm-Foley theory, based on the assumption of a Van-der-Waals interaction of the particles, the coefficients have to be scaled with $T^{0.3}$. This is in close agreement with the scaling law obtained by comparing the data of the different authors. Therefore, this temperature dependence is used, even though the assumption of pure Van-der-Waals interaction might be insufficient. It has to be mentioned that this procedure gives larger errors than for the one presented in the first part of this section and section 4.2.1. There, the gas temperature was determined by the Doppler broadening and the correction of the broadening coefficients only affected the electron density.

The experimental arrangement is the same as sketched in figure 5.10. The calibration of the wavelength was either performed by the fringes of a 2 GHz Fabry-Perot interferometer or directly with a high-resolution wavemeter (resolution 0.1 pm); both devices were inserted in the experiment by the use of beamsplitters. A comparative measurement was always done in a dc discharge for the detection of the unshifted wavelength. It is known that in such a low-pressure discharge the shift is negligible because of the low electron and gas density. The structures used for this experiments were made of platinum and had a bore diameter of 100 μm .

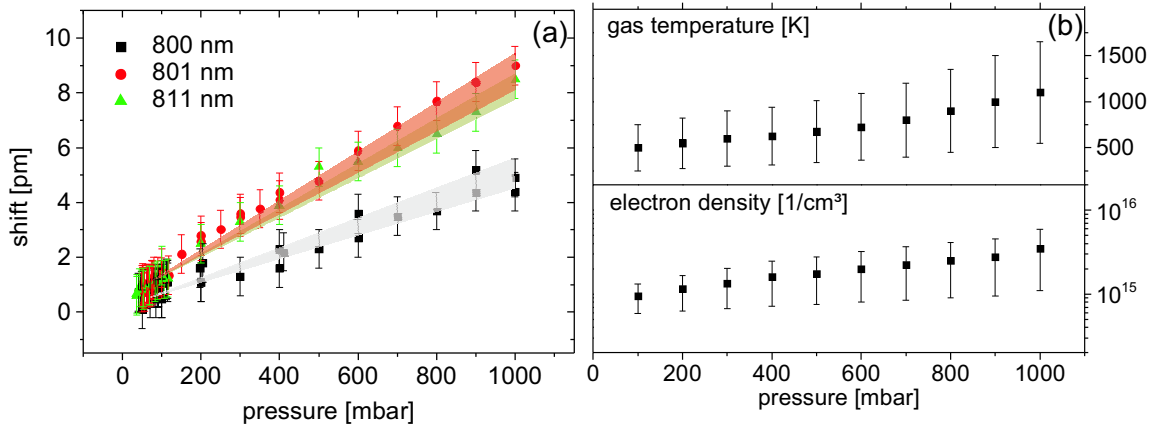


Figure 5.15: Measured line shifts for 800, 801 and 811 nm as well as calculated shifts (a) for the plasma conditions plotted in (b).

Measurements in Argon

The shifts obtained experimentally for an argon discharge are plotted in figure 5.15 (a). As one may see, all three lines reveal a linear dependence of the shift on the pressure. Furthermore, the shift of the 800 nm line, starting from a resonance level, is always much smaller than for the two transitions starting from a metastable level, as it is also expected by the shift coefficient enlisted in table 7.2. The error of the shifts, given by the uncertainty of the determination of the central wavelength, is large. This is due to the fact that only a part of the profile is obtained with the laser diodes used and the evaluation of the profile is unprecise. However, for the proposed method an error in the line shifts of less than 0.3 pm would be required. Therefore, as can be seen in figure 5.15, a wide range of values for gas temperature and electron density fulfills the shifts obtained experimentally. Figure 5.15 (a) displays the measured line shifts as well as the calculated shifts (shaded) and (b) the corresponding plasma parameters.

The exact evaluation of the gas temperature with this data set is impossible. Nevertheless, the electron density can be estimated to be in the range of $1 - 5 \cdot 10^{15} \text{ cm}^{-3}$. Interestingly, this is in close agreement with the measurements in the low-pressure region (figure 5.13), although two different structures were used. The one for lower pressure consists of copper electrodes and has a hole diameter of 300 μm optimized for low-pressure, whereas the other one is made of platinum and has a diameter of 100 μm .

Measurements in Argon and Argon-Helium mixtures

The method could also be used for the investigation of gas mixtures. In this way, the electron density and gas temperature could be determined in a helium discharge, without using helium lines, because helium offers only few lines for plasma diagnostics.

The shift coefficients (all lines are blue shifted in contrary to the red shift of the Ar self-broadening investigated) are enlisted in table 5.2. Unfortunately, only the data for the two lines 801 and 811 nm could be found in the literature.

line	β [10^{-20} cm $^{-1}$ cm 3]
801 nm	0.79
811 nm	0.37

Table 5.2: Blue shift coefficient for different transitions in Ar/He mixtures [Cop76a].

The line shifts are presented in figure 5.16 for different admixtures of He to an Ar discharge. Again, large errors occur by the determination of the central wavelength.

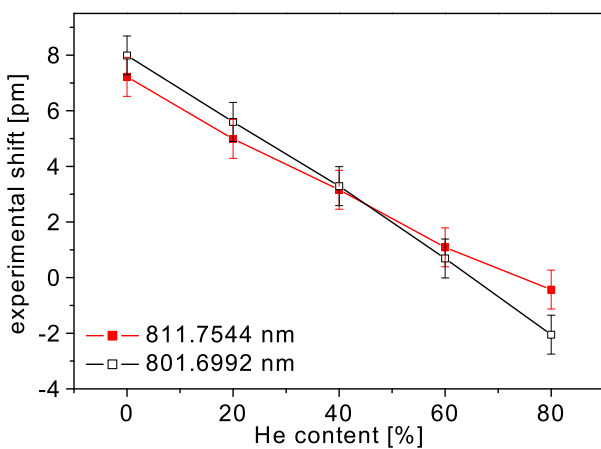


Figure 5.16: Measured line shifts for 800 and 801 nm line for different Ar/He mixtures.

Since the difference between the shifts of the two transitions which start from the metastable level is small, the relative error is much larger than in the case of the measurements discussed before. Therefore, no reliable conclusion can be drawn from these measurements. It can be estimated that the gas temperature and electron density will decrease by a factor of 2 and 10, respectively, by increasing the amount of helium in the discharge up to pure helium plasma. Nevertheless, absolute numbers are too uncertain to be presented. These results are

in agreement with figure 2.5, showing that the electron density in a helium discharge is one order of magnitude lower than in an argon discharge.

Measurements in Helium

Finally, the results obtained above for gas mixtures (showing the decrease of electron density with addition of helium) could be verified in a pure Helium plasma. For this case, the 667.999 nm line obtained by a Toshiba diode with external feedback was used. The advantage of this line is the absence of a collision-induced shift [Cop76b]. Therefore, the electron density could be determined directly with the help of the Stark coefficients given in [Mij95]. On the other hand, the gas temperature is not achievable by this method.

Line shifts in the helium MHCD were measured several times. It was observed that the shifts depend linearly on the pressure. Again, a large error occurs due to the small part of the line profile measured by the laser diodes and, consequently, sophisticated shift determination. However, the absolute values of the shifts varied strongly by several pm depending on the alignment of the laser diode through the discharge. The corresponding values for the electron density are in the range between $5 \cdot 10^{14}$ and 10^{15} cm 3 for atmospheric

pressure. These values are slightly higher than it is expected from the measurements in an argon discharge, as the values in the helium discharge should be one order of magnitude smaller. This discrepancy might be explicable by a systematic error in the determination of the line shifts in helium. As long as the laser diode passes such a small bore as in the MHCD, diffraction and refraction will appear. This may influence the line profiles and subsequently the determination of the shift. Surprisingly, the lines of the argon transitions were symmetric and well reproducible, while helium lines showed distortion.

This discrepancy could be checked applying emission spectroscopy with a high-resolution spectrometer. If so, the emission inside the hole could be detected without problems of diffraction. Additionally, line width can be determined by the measurements of the whole line profile. Hence, the unknown quantities, gas temperature and electron density, could not only be determined by comparison of the line shifts, but also from the line widths of different lines. Furthermore, the combination of the line width and shift of one transition should be consistent. In such a way the ambiguity of the broadening coefficients could also be compressed.

Nevertheless, the results obtained so far are in agreement with the simulations made by Kothnur et al. [Kot03] plotted in figure 5.17. A closed micro hollow cathode discharge was used with dimensions of 200 μm and 100 μm as the bore diameter and the cathode/dielectric thickness, respectively. They obtained an electron density of $3 \cdot 10^{14} \text{ cm}^{-3}$, and a gas temperature of more than 1500 K at atmospheric helium pressure. However, as was shown by Schönbach et al. [Mos03], modulated discharges also used in the present setup owns a higher electron density.

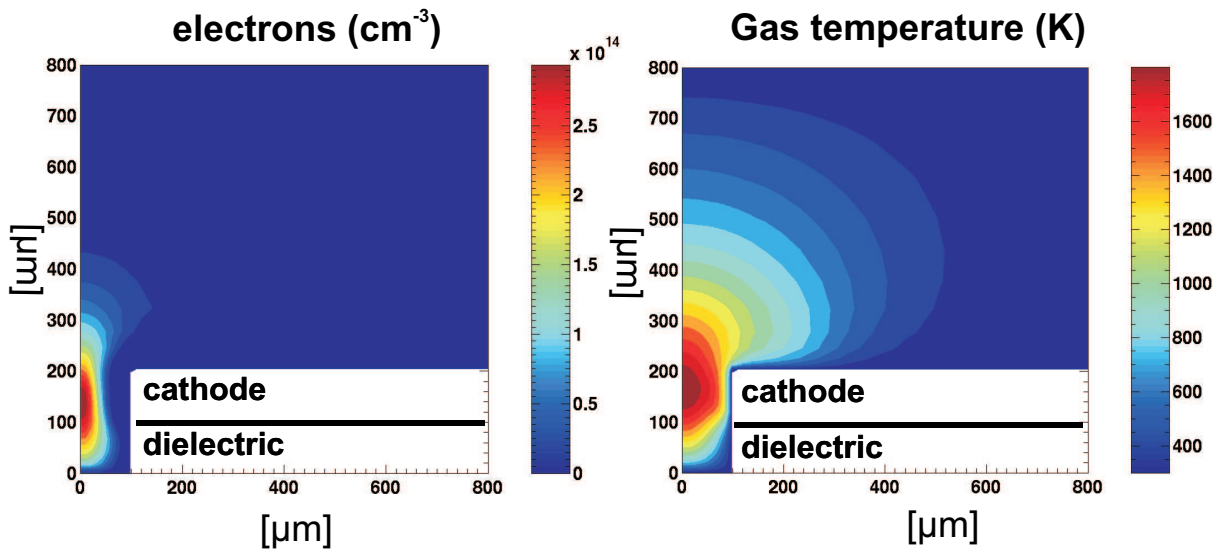


Figure 5.17: Simulation of a closed helium micro hollow cathode discharge [Kot03], $V_{gas} = 180 \text{ V}$, $p = 896 \text{ Torr}$, $D = 200 \mu\text{m}$, $I_{pl} = 3.95 \text{ mA}$.

5.2.2 Analytical applications [‡]

As presented above, the micro hollow cathode discharge is a powerful plasma with relatively high gas temperatures and electron densities. Therefore, it is applicable for analytical spectroscopy. Considering the small absorption length in the device bore, emission spectroscopy is preferred.

Atomic emission spectroscopy with an echelle spectrometer (see section 3.2) was applied for the detection of chlorine and fluorine resulting from the decomposition of the molecules. The light emitted by the plasma was imaged 1:1 on the 20 μm x 200 μm spectrometer entrance slit through an optical fibre. The entire spectral range was recorded simultaneously with an exposure time of 50 ms.

Element	λ [nm]
Cl	894.802
F	739.868
He	728.134
H	656.358
N	868.028
O	844.675
Ar	811.531
C	965.843

Table 5.3: Emission lines measured in MHCD.

The emission lines measured, belonging to the investigated halogens and the buffer gas, are summarized in table 5.3. The measurements were performed mainly in He because both Cl and F atomic lines can be recorded while in Ar fluorine could not be measured. This is due to the fact that the excited fluorine levels are higher than those of Ar [Mic01].

Figure 5.18 shows one order of the echelle spectrum in which the chlorine emission line at 894 nm appears for different amounts of freon. As can be seen, the lines are well separated and no spectral interferences occur. The intensity of different atomic lines is plotted in dependence on the CHClF_2 concentration in He at 1 bar and 4 mA in figure 5.19. For this purpose, the halogenated hydrocarbons were pre-mixed with He before the

gas was introduced into the plasma. The measurements started always from an initial mixture of He with 17 ppm halogenated molecules and this mixture was diluted down to a concentration at which the signal was 3 times the noise. The intensities of the emitted lines of the buffer gas are independent on the molecule concentration. This indicates the robustness of the discharge, as the excitation process is not disturbed by the analytes. The intensities of the Cl and F lines are linearly dependent on the amount of freon. Assuming the complete dissociation and atomization of the introduced molecules, it is expected that the H and C signals depend linearly on the CHClF_2 concentration as well. However, this is not the case. The reasons might be a contamination of the plasma gas by H_2O and the formation of parasitic species, such as CO or CO_2 in the discharge.

[‡]This section has been published partially in *Plasmas for lab-on-the-chip applications*, Spectrochim. Acta, Part B **57** (2002) 1585 – 1592 [Mic02].

Figure 5.19 presents calibration curves for Cl and F for different freon gases in He. The calibration curves are linear over almost 3 orders of magnitude, but at small concentrations it can be noticed that the calibration curves of the F line flattens owing to a memory effect of the discharge walls by fluorine. Nevertheless, CCl_2F_2 detection limits of 20 ppb in He were found using the Cl 912.114 nm as well as the F 739.868 nm line. This was also obtained with other halogenated hydrocarbons. The detection limits with Ar as a buffer gas were in the same order of magnitude.

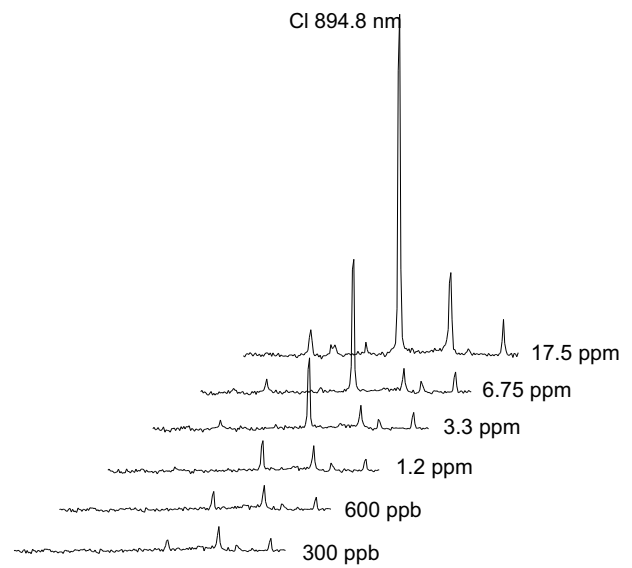


Figure 5.18: 84th order of the echelle spectra for different concentration of freon.

In order to study the capability of complete dissociation, the Cl and F line intensities with CCl_2F_2 and CHClF_2 in the He MHCD discharge were measured by varying the species concentrations. On the right hand side of figure 5.19 it can be seen that the F line intensities are independent on the species within the experimental errors. On the other hand the Cl line intensities obtained with CCl_2F_2 is a factor of two higher than with CHClF_2 as it is expected from the stoichiometry. This does not prove complete, but similar dissociation of the molecules. The complete structure of the molecule can be obtained by measuring all atomic lines of interest.

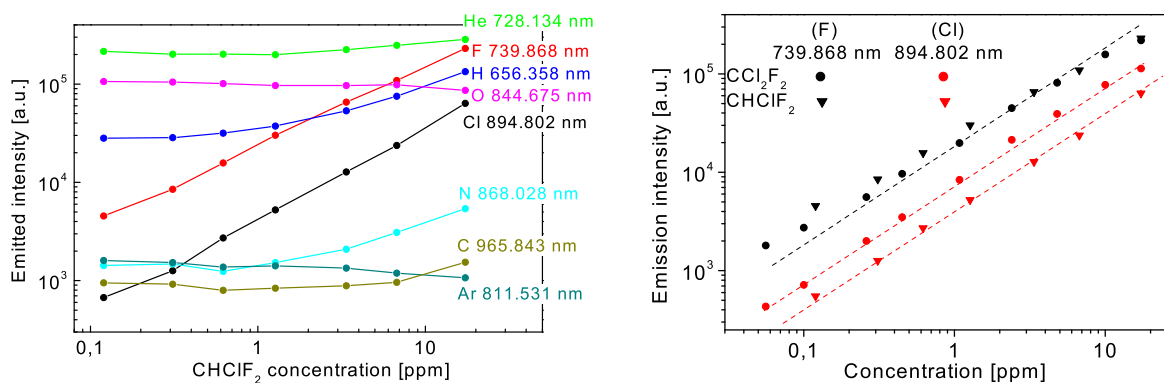


Figure 5.19: Evolution of the emitted lines with the halogenated molecule concentration in He with an admixture of CHClF_2 and calibration curves for different freon gases concerning the chlorine and fluorine line (parameters: $p = 1$ bar, $I_{pl} = 4$ mA).

It is advantageous that the complete analyte is forced to pass the bore by this setup of the discharge. However, it was observed that the same analyte signals were obtained, if the gas mixtures were flushed around the discharge. If a vacuum tight connection for the structure is used, so that the gas is flowing only through the hole of the structure, the discharge chamber can be abandoned. The micro hollow cathode discharge can be directly mounted onto the rare gas supply and it is burning with a slightly higher pressure than atmosphere also in an air environment. A signal decrease of less than a factor two was observed.

5.3 Micro hollow cathode plasma jet

As shown in the previous section, the micro hollow cathode discharge at atmospheric pressure is well suited for trace analysis. The detection limits in emission show a good dissociation and, furthermore, the electron density is high. Therefore, the MHCD should be an efficient ion source for mass spectrometry. However, the high-pressure discharge has to be coupled with a low-pressure detection system (see section 3.4). In order to obtain this low-pressure, pressure stages have to be used. In common mass spectrometry (e.g. ICP-MS), so-called sampler and skimmer with an opening diameter of several hundred micrometers are used. The sampler cares for the first separation stage and the skimmer is the entrance orifice to the mass spectrometer. In the sampler-skimmer interface an adiabatically expansion of the gas occurs.

The MHCD can be operated in two modes: the static mode, in which at both sides of the structure is the same pressure, and the jet mode when a pressure difference is established between the anode and the cathode side [Pen02]. The gas temperature, the electron density and the electron energy distribution function are changing by varying these parameters. As lower the pressure on cathode side, as lower the values are. Therefore, at the first glance, the static mode of the discharge is more suitable for mass spectrometry. The gas temperature and electron density in the discharge are higher, and, therefore, better dissociation and ionization take place. Furthermore, the residence time of the particles in the discharge is much higher than in a jet, where the particle pass the hole of the structure in microseconds. On the other hand the atmospheric pressure results in a mean free path of a few micrometer for the ions. Even though no charge transfer is observed in helium because of its ionization potential, the ions are lost because they do not reach the sampler. In order to increase the number of ions passing the sampler, the distance has to be very

small and the diameter large. However, a small distance results in turbulent flows and electrical disturbances, while a large diameter prevents the small pressure demanded in the quadrupole. Additionally, on the basis of the small flow a large time constant might appear for transient analyte signals. On the contrary, a plasma jet has a residence time of a few microseconds leading to no delay in transient analyte signal and offers a much more feasible arrangement because the structure is fulfilling the function of the ion source and the sampler simultaneously. The adiabatic expansion of the jet leads to highly directed ion velocities, wherefore more ions are reaching the skimmer than in the static case.

In the following experiments, the investigations were constricted on helium discharges: first, the sputtering rate in an argon discharge is higher than in a helium discharge leading to shorter lifetimes of the structure. Secondly, the charge transfer in a helium discharge is prevented because of the ionization potential. On that basis, analyte molecules and atoms, once ionized will stay ionized, while in an argon discharge the charge transfer leads to de-ionization of the analyte.

This plasma jet was invented by the group of Prof. Schmidt-Böcking at *IKF Frankfurt*, who investigated the metastable helium atoms [Hoh02]. In cooperation with them, the first measurements of coupling the MHCD with a mass spectrometer were performed.

5.3.1 Adiabatic expansion

If a gas is flowing through a small orifice applying a pressure gradient, an adiabatic expansion can occur. On the high-pressure side, the gas can be described by the macroscopic state variables like the pressure p_o and the temperature T_o . The gas is in a thermal equilibrium and no direction of velocity is favored. As long as the pressure in the low-pressure region is small compared to the stagnation pressure, but higher than a critical value, an effusive expansion is present, in which the particles still have a broad but Maxwellian distribution. In order to reach an even narrower velocity distribution the pressure has to be reduced further, and a supersonic jet is formed. In the case of

$$p \leq p_o \left(\frac{\gamma + 1}{2} \right)^{\frac{\gamma}{\gamma-1}}. \quad (5.5) \quad \left| \begin{array}{l} \gamma \quad c_p/c_v \\ c_{p,v} \quad \text{specific heat capacity at constant p,v} \end{array} \right.$$

the velocity of the particles at the end of the narrow orifice equals the sound velocity, and the pressure the upper limit of equation 5.5. In the case of an ideal mono-atomic gas like helium, γ is 5/3 and the critical pressure almost half the stagnation pressure p_o . As the pressure of the nozzle exceeds the background pressure of the vessel p_b , the

flow is “underexpanded” and subsequent expansion occurs. In this case, the temperature decreases, while the velocity increases. The atoms and molecules reach velocities that can be much higher than the sound velocity ($c_s = \sqrt{\gamma kT/m}$). The ratio between both velocities (Mach number M) is equal to one in the nozzle, while in the low-pressure chamber much higher values are obtained.

The maximum achieved velocity can be calculated assuming the change in energy for a mono-atomic gas (like helium) given by

$$\begin{aligned} dh &= \frac{v^2}{2} & (5.6) \\ &= c_p dT. & (5.7) \end{aligned} \quad \left| \begin{array}{l} h \text{ mass-specific enthalpy} \\ v \text{ velocity} \\ c_p \frac{\gamma}{\gamma-1} k/m \end{array} \right.$$

This equation can be solved for the velocity supposing that the specific heat capacity c_p is constant in a range of $T_o - T_{jet}$ and that the gas is drastically cooled, so $T_{jet} \ll T_o$

$$v_{jet} = \sqrt{2c_p T_o} = c_s \sqrt{\frac{2}{\gamma-1}}. \quad (5.8) \quad \left| \begin{array}{l} c_s \text{ velocity of sound} \\ \gamma \ c_p/c_v \end{array} \right.$$

This maximum achievable velocity corresponds to the total conversion of thermal energy into kinetic one.²

A schematic jet is shown in figure 5.20. The background pressure given by the finite pumping power, results in the generation of shock waves. These are areas of high density in which the particles of the beam are slowed down due to collisions. They can be ostensively explained assuming that the gas expands with a Mach number larger than one but the information propagates only with sound velocity. Therefore, the jet does not sense the background pressure; nevertheless, it has to adjust with this incident. The solution of this dilemma is in the occurrence of shock waves. The most important one is the so-called “Mach disc” which is in the line of the flow. The distance of the Mach disc from the nozzle is given by the empirical formula [Mil88]

$$\frac{x_m}{D} = 0.67 \sqrt{\frac{p_o}{p_b}}. \quad (5.9) \quad \left| \begin{array}{l} x_m \text{ mach disc} \\ D \text{ diameter of nozzle} \\ p_o \text{ pressure before nozzle} \\ p_b \text{ background pressure} \end{array} \right.$$

²This simple model assumes a zero velocity at the beginning of the nozzle. If the gas is already flowing into the source before it starts to expand, the factor 2 has to be replaced with $\gamma + 1$. So in the plasma jet v_{jet} amounts to $c_s \sqrt{\frac{\gamma+1}{\gamma-1}}$. [Mil88]

Concluding, in the case of an adiabatic expansion the undirected velocity of the particles is transferred into a directed motion of the particles. They are slowed down again at the Mach disc. The skimmer of the pressure stage has to be placed inside the Mach disc in order to extract the ions without the disturbance of the background pressure.

Two types of jet – skimmer configurations are known, the Fenn- and Campargue setup. In the Fenn configuration the background pressure is chosen to be smaller than $5 \cdot 10^{-3}$ mbar which necessitate strong pumping systems like diffusion pumps. Considering the long Mach disc spacing, the adjustment of the skimmer is less critical. In contrary, the Campargue type was developed in earlier days, when less strong pumps were available. Typically, the pressure in the chamber is higher

than $5 \cdot 10^{-2}$ mbar. In this case, the shockwaves are more pronounced and help to shield the jet from the background gas. Due to the different geometry of the two skimmer types, the angle of the skimmer is in the first 30° and in the second case 50° .

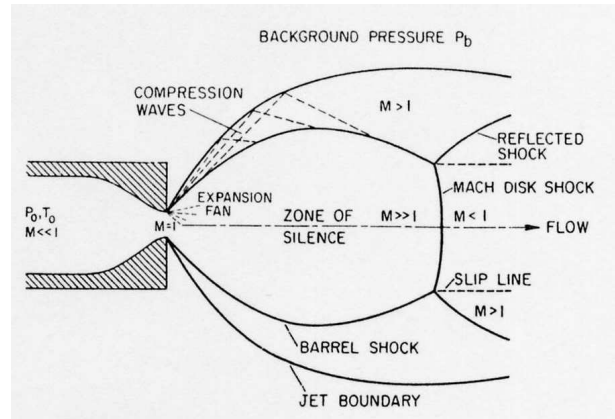


Figure 5.20: Continuous free-jet expansion [Mil88].

5.3.2 Plasma diagnostics

The optical appearance of the discharge, the electrical characteristics and the determination of excited atom density were performed in two arrangements, one connected to the mass spectrometer and one in a bigger chamber without interface. For the plasma jet configuration the structure of the micro hollow cathode discharge had to be mounted between two separated chambers, allowing the gas to expand only through the bore. A picture of the mounting is shown in figure 5.21. The MHCD structure is mounted on the left side. A

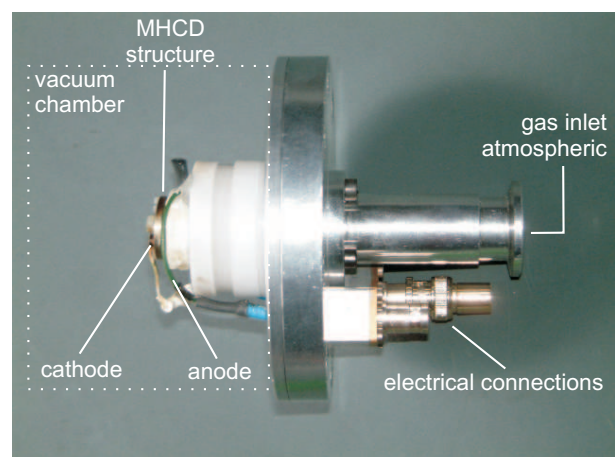


Figure 5.21: Picture of the MHCD jet configuration for the pressure drop.

vacuum tight connection between the vacuum chamber and the high-pressure gas inlet was either performed with an O-ring or, in the case of the copper structures, using a crimp connection. The low-pressure on the cathode side was generated mainly by a rotary pump. Using atmospheric pressure on anode side and with a hole diameter of 100 μm , pressures down to 0.5 mbar could be obtained. Lower pressures can only be achieved by using a stronger pump, like a small turbo pump (50 l/s). Nevertheless, for a continuous operation of the turbo pump the pressure and gas flow in the chamber are too high. Therefore, the investigations were restricted to pressures in the range of 1 mbar. It was also observed that the analyte signals are increasing with the pressure on cathode side (see next section).

Optical measurements

The transition of the micro hollow cathode discharge from high to low-pressure is clearly visible by naked eye. While the discharge at high-pressures at both anode and cathode sides is constricted in the plasma hole and on the cathode surface, the discharge expands outside the hole if the pressure at cathode side is reduced. At a pressure ratio of 2 a thin discharge needle is vacating the structure hole. Snapshots for different cathode side pressures and fixed anode side pressure of 1 bar are shown in figure 5.23.

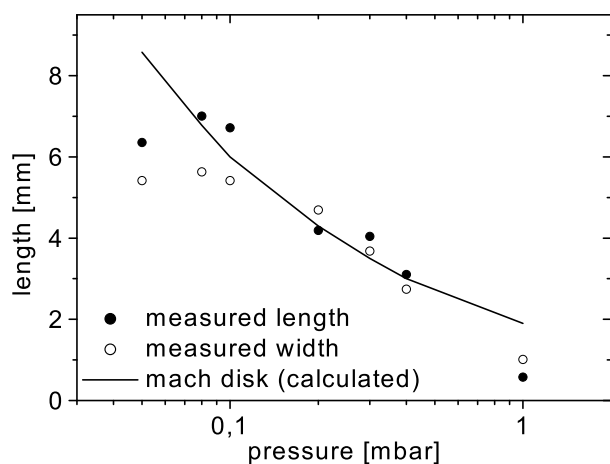


Figure 5.22: Length of Mach disc in dependence on pressure.

As can be seen, the background color of the discharge changes from dark blue to cyan lowering the pressure, which means a shift of the emitted line region from 450 to almost 500 nm. This displacement is based on different excitation and de-excitation mechanisms, which has to be investigated further in emission spectroscopy. One can further observe on the pictures the size of the plasma jet and the formation of a Mach disc. It is possible to measure the size of the Mach disc at different pressures using the distance of the screws (dimly visible at 0.2 mbar below and above the jet) as a reference and determining the extent of the light ball. The result for the measured length and horizontal diameter is plotted in figure 5.22. They are in good agreement with the data calculated from equation 5.9.

As can be seen, the background color of the discharge changes from dark blue to cyan lowering the pressure, which means a shift of the emitted line region from 450 to almost 500 nm. This displacement is based on different excitation and de-excitation mechanisms, which has to be investigated further in emission spectroscopy. One can further observe on the pictures the size of the plasma jet and the formation of a Mach disc. It is possible to measure the size of the Mach disc at different pressures using the distance of the screws (dimly visible at 0.2 mbar below and above the jet) as a reference and determining the extent of the light ball. The result for the measured length and horizontal diameter is plotted in figure 5.22. They are in good agreement with the data calculated from equation 5.9.

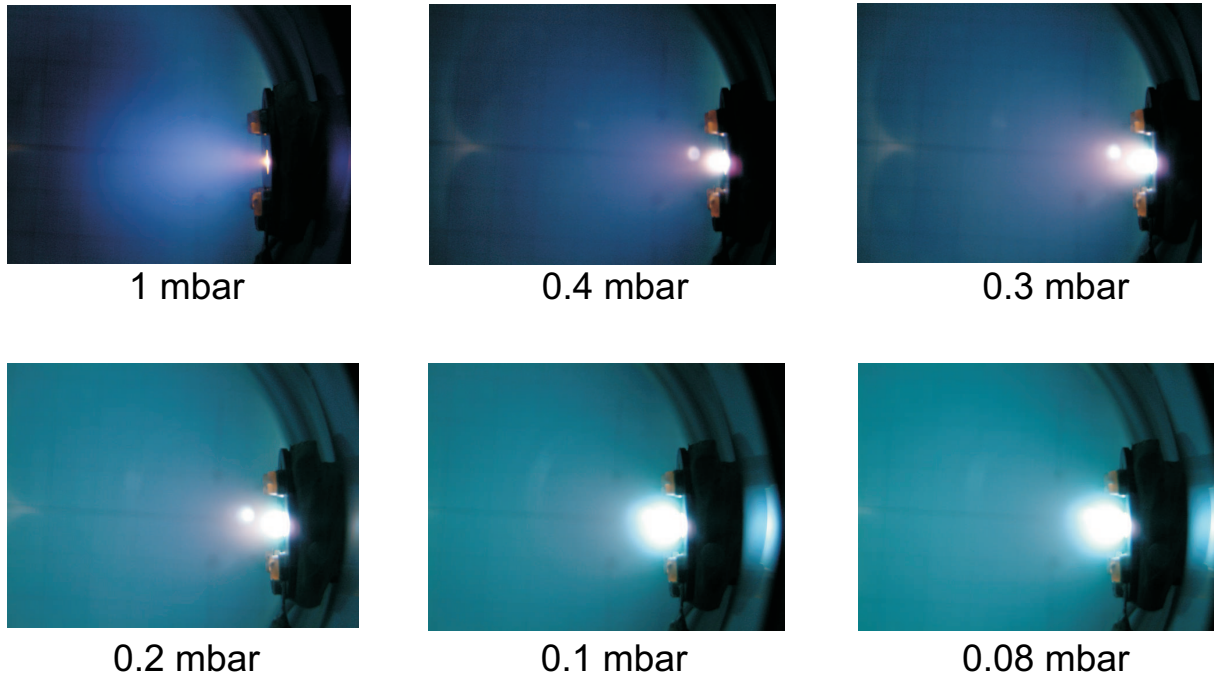


Figure 5.23: Photos of the plasma jet at different cathode side pressures, anode 1 bar.

Electrical characteristics

The transition of the high-pressure discharge to a plasma jet is also visible in the current-voltage characteristic plotted in figure 5.24. Compared to a static discharge (see figure 5.8), the gas voltage is higher and clearly decreasing with the current. The need of higher gas voltage in the jet configuration can be explained by the energy removal due to the high gas flow that has to be compensated. In the configuration with the skimmer it was observed that the presence of the skimmer changes the plasma potential in such a way that the gas voltage is decreased or increased depending on whether the skimmer is grounded or floating.

For stable plasma the grounded configuration was chosen, otherwise the skimmer was charged up to 200 V, depending on the voltage and the current applied. It has to be mentioned that the short distance of the skimmer to the micro hollow cathode discharge leads to an additional current flow over the skimmer. This can be measured using a 50 Ω resistance and its value is up to 1 mA. This is almost a third of the power at the 3 mA current commonly used.

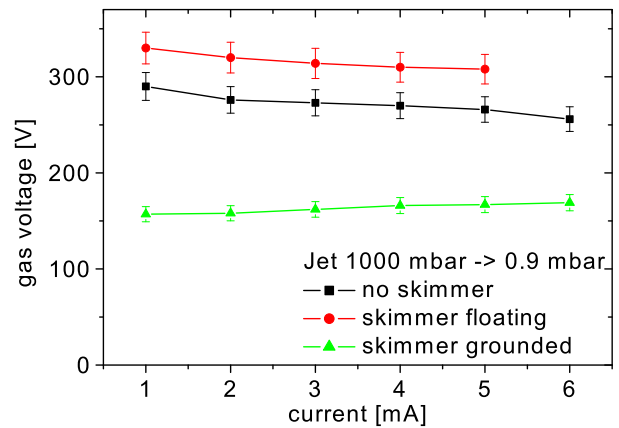


Figure 5.24: Current-voltage characteristic.

Laser absorption

Spatially resolved measurements of excited atoms The spatial distribution of the excited helium atoms was investigated with a similar arrangement as shown in section 5.2.1. The collimated beam of the laser diode was either adjusted through the hole of the structure or it was passed parallel to the cathode surface in a specific distance; the plasma was modulated with several hundreds Hz in order to improve the signal to noise ratio.

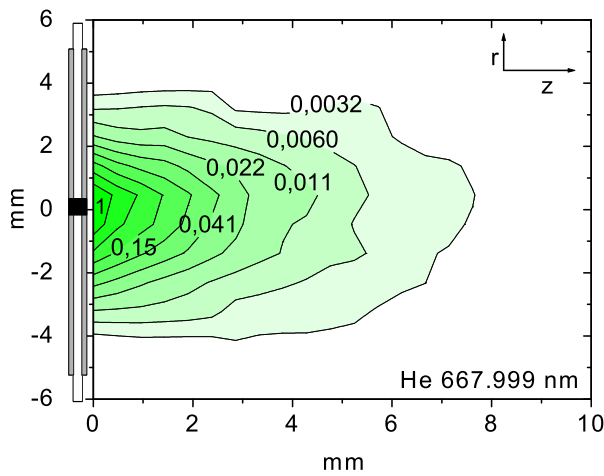


Figure 5.25: Abel-inverted spatial distribution of the helium atoms in resonance state, $1000 \rightarrow 0.7$ mbar, 3 mA, 250 V.

The spatial distribution of the relative absorption of the excited helium atoms in the resonance state is shown in figure 5.25. The absorption was probed side-on with a step width of $500 \mu\text{m}$ and 1 mm in z - and y -direction, respectively.

Firstly, the absorption measured perpendicular to the plasma jet is averaged over different radial positions. However, the cylindrical symmetry of the plasma jet enable the deconvolution of the image by the Abel inversion. The measured values $I(y)$, which are the transmitted laser intensities integrated along the x -direction, at various

points along the y -axis. They can be converted to the spectral radial distribution $\epsilon(r)$. The measured intensity is given by

$$I(y) \sim \int_{x_1}^{x_2} \epsilon(\sqrt{x^2 + y^2}) dx = \int_y^R \frac{2r\epsilon(r)}{\sqrt{r^2 - y^2}} dr, \quad (5.10)$$

while the inversion of this expression yields the desired quantity

$$\epsilon(r) = -\frac{1}{\pi} \int_r^R \frac{dI(y)}{dy} \frac{dy}{\sqrt{y^2 - r^2}}. \quad (5.11)$$

R is the radius of the cylindrical shape. This conversion can be done by a discrete method, described and tabulated in [LH68]. In this measurement, 8 positions in y direction were used for each distance in z -direction.

Excited atoms can be observed even several mm outside the hole. The expansion of the particles in the Mach disc is so close to the bore that the distribution is not resolvable.

The density of excited atoms can be calculated according to equation 3.5. As can be seen, the absorption length L has to be known very well, but it can only be estimated in the current experiment by evaluation of figure 5.25. A medium value for the absorption length close to the hole of the structure is assumed to be 3 mm. In this case the density of excited He atoms in resonance and metastable state is $3 \cdot 10^{10} \text{ cm}^3$ and $1.5 \cdot 10^{12} \text{ cm}^3$ probing the transition at 667 and 388 nm, respectively. An error of 30 % has to be kept in mind for the uncertainty of the absorption length. In addition this value is only valid close to the hot region of the structure; the spatial decrease is according to figure 5.25, and the maximum value inside the hole is unknown.

Line profile measurement It was shown that the electron density in the atmospheric pressure helium MHCD might be 10^{15} cm^3 which is reduced by decreasing the pressure. The measured absorption line shift of the 667 nm line by reducing the pressure on cathode side is shown in figure 5.26. The laser beam passed the hole in the direction of the flow and opposite to it. The difference between both directions is clearly seen and given by the Doppler-shift of the lines. Furthermore, an increase of the line shift for pressures of several hundreds of mbar is visible. This phenomenon has not been explained yet, but the determination of the shift is very critical in this regime, because the line profiles are broad and begin to be distorted due to the transition to a non-Lorentzian line shape. Therefore, in the following plot the evaluation is limited to the low and medium pressure range in which the line shift could be measured within a reasonable error. Furthermore, it was proved that these line shifts do not depend on the alignment.

As can be seen for pressures below 100 mbar, a constant shift, negative in forward direction and positive in opposite direction, is obtained. Both have the same amount, but different

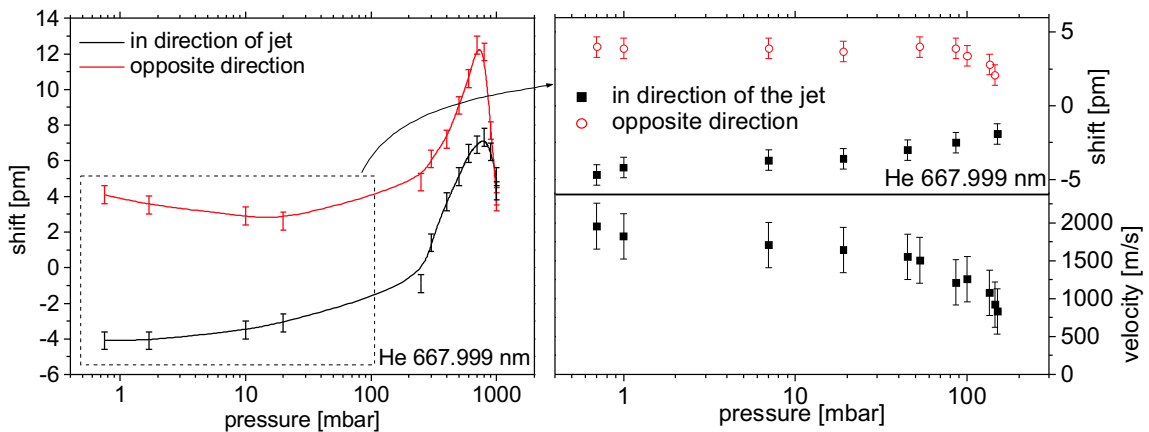


Figure 5.26: Line shift measurements in the micro hollow cathode jet and determined velocities therein.

signs. This indicates that the electron density does not contribute anymore to the shift, because it is smaller than 10^{14} cm^{-3} and is not detectable by this method. The shift obtained is identified as the Doppler shift, which is directly connected to the velocity of the particles. This is plotted in the right hand side of figure 5.26. It has to be mentioned that the line profile at reduced pressure is not anymore symmetrically because of the favored directed motion of the particles and consequently, no Gaussian profile is obtained. The value of the first order Doppler shift is given by

$$\Delta\lambda = \lambda_0 \frac{v}{c}. \quad (5.12) \quad \left| \begin{array}{l} v \text{ velocity of the atoms} \\ c \text{ velocity of light} \end{array} \right.$$

At the lowest pressure directed velocities of almost 1800 m/s are approached. If this is the maximum velocity of the jet, this equals – according to equation 5.8 – to a gas temperature of 315 K in the hole. It has to be mentioned that this value implies that particles in the bore have a Maxwellian distribution. However, such an assumption cannot be proved.

5.3.3 The MHCD as ion source for analytical mass spectrometry[‡]

Experimental setup The experimental arrangement is presented schematically in figure 5.27. The MHCD was mounted in front of the quadrupole mass filter as already described in section 3.4. The discharge could be mounted at different distances from the skimmer. The distance plasma skimmer was calculated according to the theory of free flow (equation 5.9) in order to collect the ions from the free jet centerline. The skimmer cone with a diameter of 0.8 mm was installed mostly around 3 mm away from the plasma, which was in agreement with the size of the Mach disc at the pressures used. The skimmer produced a perturbation of the plasma potential because of the small distance to the structure, and was grounded to obtain stable conditions. For each experimental operation condition, the five ion lenses behind the skimmer were adjusted to get optimum signals. The gas was flowing from the anode side, where the positive high voltage was applied, to the cathode side, which was grounded.

The analyte samples passed the plasma with the main gas stream. The samples were (1) mixed with the plasma gas, (2) introduced from a calibrated permeation source to the gas flow, or (3) separated by a gas chromatograph and then introduced into the main gas

[‡]Part of this chapter is accepted for publication in J. Anal. At. Spectrom. [Mic04]

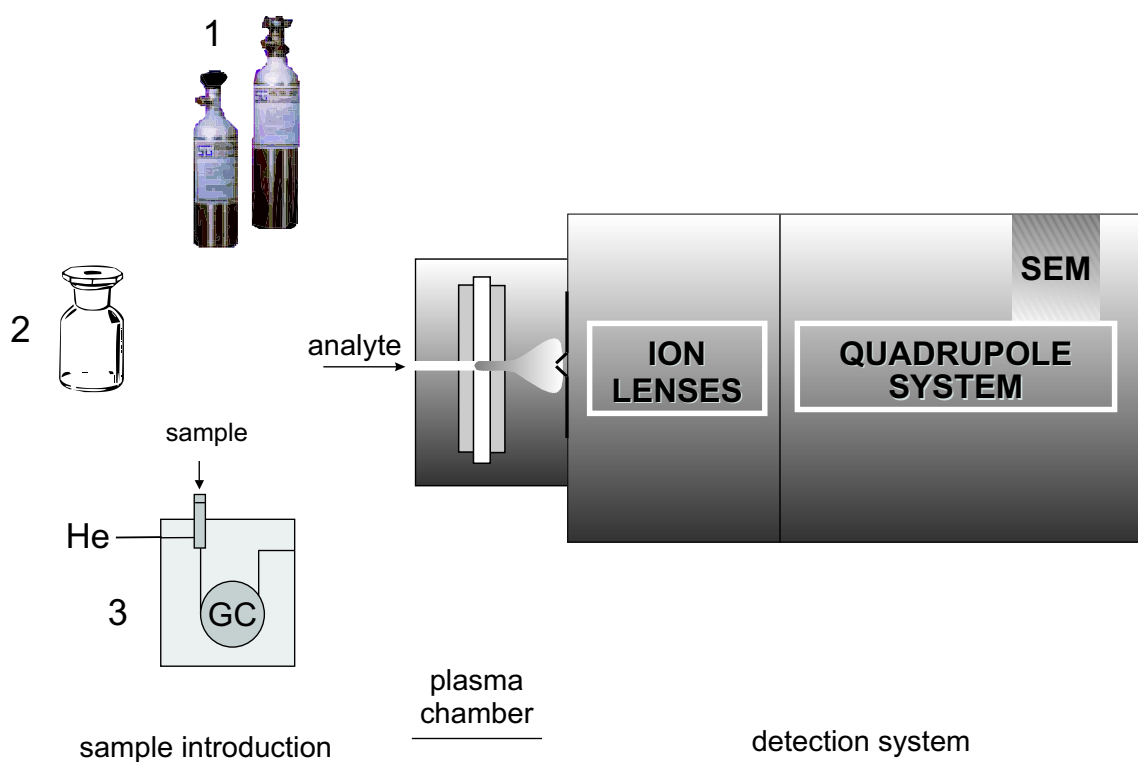


Figure 5.27: Experimental arrangement consisting of: different sample introduction systems ((1) gas mixture, (2) permeation source, (3) gas chromatograph), plasma jet source and mass spectrometer.

stream. The used samples are summarized in table 5.4. In the case of gas mixtures (1), the analyte was pre-mixed with He in a gas bottle, obtaining an initial concentration of a few ppm. The bottle was connected at the anode side and the gas mixture passed through the plasma. For smaller concentrations, the initial mixture was diluted with He and reconnected to the system. In the second case (2), the permeation source (a small glass vial sealed with a 0.1 mm Teflon membrane and filled with the volatile analyte) was placed in a small chamber directly in the He gas flow providing the plasma. After a few minutes, equilibrium between the permeating gas and the He gas was established, and this stayed constant during the measurements. For the gas chromatography coupling (3), the column of the gas chromatograph (Shimadzu GC-14A, column FS-SE-54-CB-1) was placed at a distance of a few mm in front of the anode and an additional gas flow was inserted in front of the structure for an additional supply with helium. The gas flow from the gas chromatograph alone (less than 4 ml/min) was not enough to sustain a stable plasma jet. The plasma was switched off for the time when the solvent was eluted, because high concentration of organic compounds could not be tolerated. The reason is that significant amounts of carbon deposited in the hole would destroy the microstructure. The constant addition of small amounts of oxygen (less than 2 %) that was added to the gas flow helped

Gas mixtures	Freon-12 CCl_2F_2 Freon-22 CHClF_2
Permeation source	carbon tetrachloride CCl_4 chloroform CHCl_3 dichloromethane CCl_2H_2
Gas chromatograph	fluorobenzene $\text{C}_6\text{H}_5\text{F}$ 1,2-dichloropropane $\text{C}_3\text{H}_6\text{Cl}_2$ 1-bromobutane $\text{C}_4\text{H}_9\text{Br}$ 1-chloropentane $\text{C}_5\text{H}_{11}\text{Cl}$ 1-iodobutane $\text{C}_4\text{H}_9\text{I}$ 2,5-dimethylthiophene $\text{C}_6\text{H}_8\text{S}$ 1-bromo-4-chlorobutane $\text{C}_4\text{H}_8\text{BrCl}$
solvent	pentane C_5H_{12}

Table 5.4: Samples used for mass spectrometric measurements.

to prevent deposition of carbon without influencing the ion signals. The lifetime of the device was not shortened by the addition of oxygen, while it was considerably decreased by the presence of high amounts of reactive species or carbon.

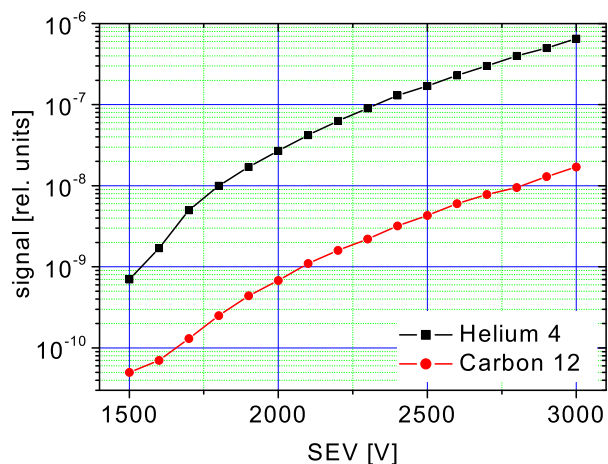


Figure 5.28: Variation of signal for different electron multiplier voltages.

The variation of the signal on the electron multiplier voltage is shown in figure 5.28 for the two ion channels corresponding to carbon and helium. As can be seen, an amplification of almost 3 orders of magnitude can be obtained by changing the applied voltage. Most of the measurements were carried out at moderate voltages of 2500 V.

Mass spectra and generated ions

A sample mass spectrum of a mixture of helium with CCl_2F_2 is shown in figure 5.29. The three plotted spectra are measured with three different preamplifications so as

to determine all ions, which would be either saturated or not detectable just by a fixed amplification factor. The strongest signals are those of the buffer gas helium (4 u) and impurities as nitrogen (14 u), hydrogen (1 u), oxygen (16 u) or water (18 u). These impurities can either be introduced in the system by the buffer gas itself (the used He 4.9 contains several ppm of different impurities) or by a small leak in the whole system. The analytical signals by decomposition of CCl_2F_2 are two orders of magnitude smaller.

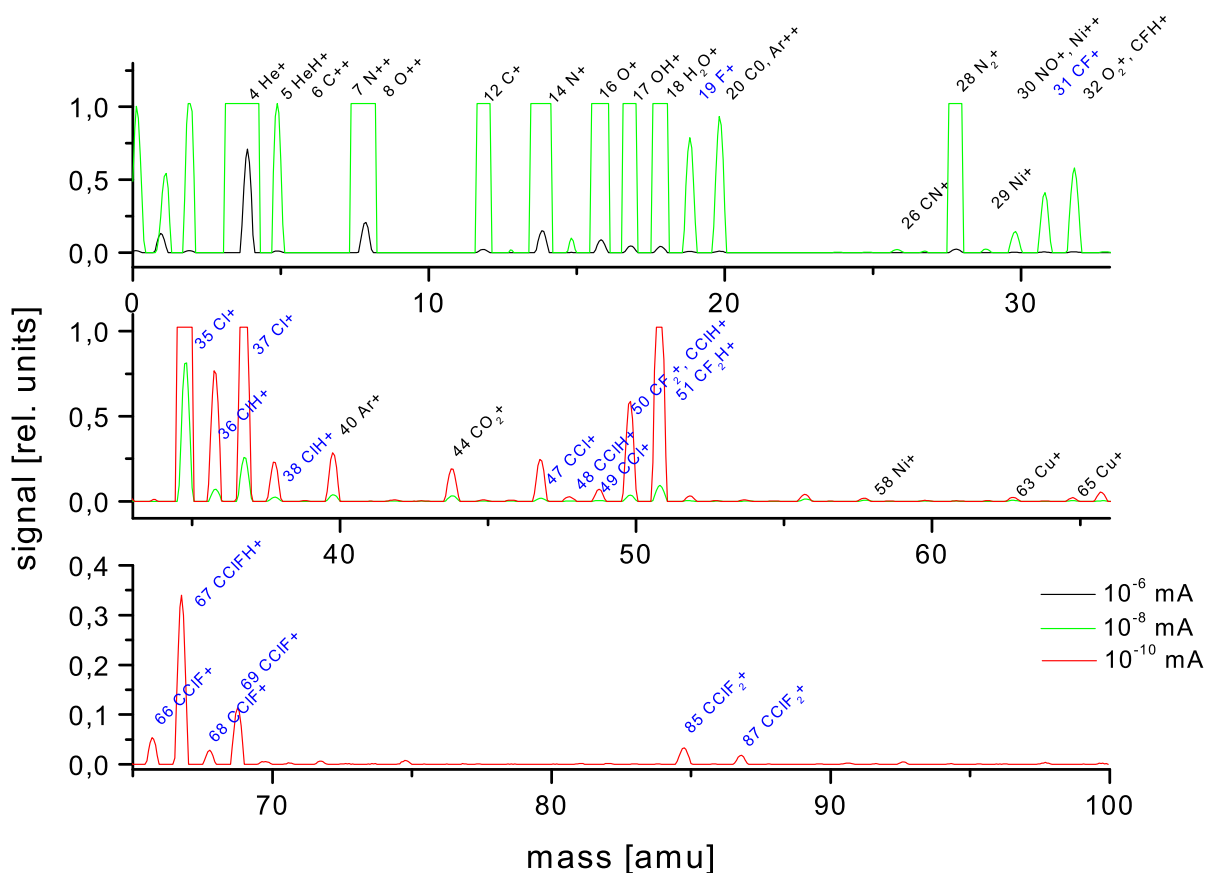


Figure 5.29: Mass spectra for a mixture of 17 ppm CCl_2F_2 in helium, structure made of Cu/Ni.

The strongest signals belong to the atomic ions of chlorine, fluorine and carbon. It has to be mentioned that the carbon signal is not only obtained from the analyte of interest, but could also be due to contamination with CO_2 or CO . These gases are present in the order of several ppm in the He gas. Chlorine has two isotopes with a mass of 35 and 37 u, having a natural ratio of 3 : 1. This fraction can be found in the plot, too. In the following plots, the discussion will be restricted to the ^{35}Cl mass for simplicity reasons³. Furthermore, molecular fragments resulting from the decomposition of CCl_2F_2 are detected. In any case, it has to be noted that the whole molecule (mass 120 u, not plotted) cannot be measured, which is in accordance with mass spectra obtained by electron impact published by NIST [NISov]. This is caused by the smaller (at least 2 orders of magnitude) partial electron ionization cross section of the CCl_2F_2 molecule compared with the other fragments [Lei88]. It has to be mentioned that only sputtered metal ions (copper, nickel) were measured but no molecules formed with the analytes or plasma gas impurities. The appearance of many protonated ions, like FH^+ , ClH^+ or CClH^+ is very conspicuous,

³The isotope ratio complicates the spectrum, starting to have 2 or more chlorine atoms in a compound, because the fraction is overlapped with the statistical probability 1:2:1 to form molecules with two different atoms.

even though they are no fragments of the introduced molecule. This is because of the strong proton affinity of products in the discharge.

Optimization of the operational parameters The power coupled into the plasma and the pressure in the interface are the only parameters that can be optimized as long as the pressure at the anode side is in the atmospheric pressure range. The gas flow through the plasma depends only on the pressure in front of the anode, the hole diameter and the source gas kinetic temperature. For this system with a 100 μm hole diameter, the gas flow varied between 100 ml/min and 200 ml/min for a pressure of 1000 mbar and a gas temperature between 400 and 1000 K. For such flow rates, the transit time of gas particles through the hole is about 1 μs , which is still 3 orders of magnitude higher than the mean time between collisions. At such reduced transit times, it is expected that a weak dissociation takes place, which can be seen in the measured mass spectra showing atomic ions and ions of molecular fragments. It has to be mentioned that the incomplete dissociation can be used to indicate the chemical structure of the analytes that can be configured from the signals of the fragments. The optimization of the plasma operating conditions was performed by drastically changing the pressure at the cathode side in order to analyze its effect on the measured mass spectra. The distance plasma – skimmer was always adjusted so that the skimmer was placed in the Mach disk to avoid ion recombination and reactions which, additionally, change the mass spectra.

In figure 5.30 the mass spectra of CCl_2F_2 in He are shown after the subtraction of the background gas spectrum. Figure 5.30a displays a spectrum measured at a pressure of

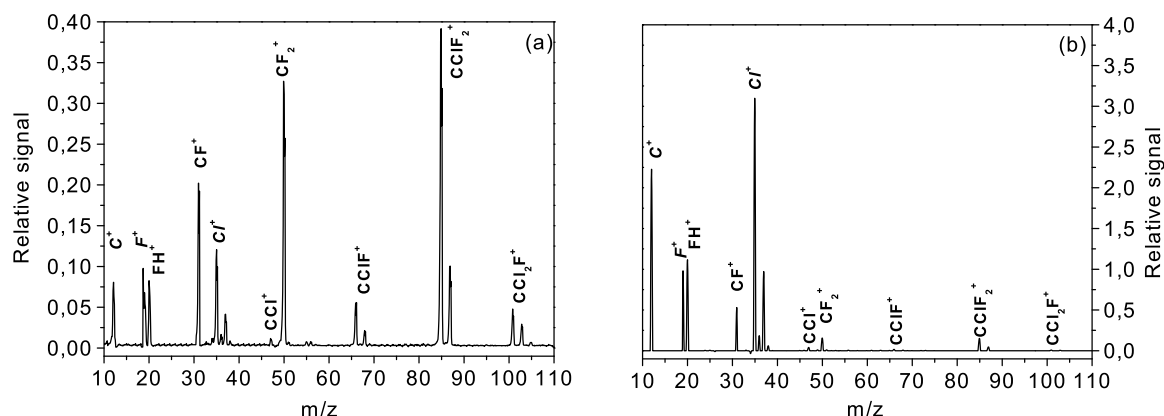


Figure 5.30: Mass spectra of the MHCD in He + 3 ppm CCl_2F_2 after subtraction of the background for different operational conditions: a) W structure, $D = 110 \mu\text{m}$, $p = 840 \text{ mbar} / 7 \cdot 10^{-4} \text{ mbar}$, $V_{\text{gas}} = 260 \text{ V}$, $I_{\text{pl}} = 2 \text{ mA}$; b) Pt structure, $D = 100 \mu\text{m}$, $p = 840 \text{ mbar} / 4 \cdot 10^{-1} \text{ mbar}$, $V_{\text{gas}} = 192 \text{ V}$, $I_{\text{pl}} = 2 \text{ mA}$.

$p_c = 7 \cdot 10^{-4}$ mbar. A higher pressure ($p_c = 4 \cdot 10^{-1}$ mbar) has a significant impact on the spectrum as shown in figure 5.30b. There are more fragment ions if the pressure is lower (note also the difference in scale in the figures). A possible explanation is that the electron energy and the gas temperature are decreased at lower pressure leading to a reduced dissociation and ionization. Furthermore, it can be seen that the relative concentration of atomic ions (here $^{35}\text{Cl}^+$) is increasing with pressure. This simplifies the whole experimental arrangement because only one fore pump has to be used.

Plasma gas as well as analyte ion signals depend on the pressure at the cathode side of the MHCD. For example, the analyte signals are increasing one order of magnitude while the He ion signal is decreasing less than one order of magnitude if the pressure p_c was varied from 0.6 to 1.5 mbar at constant pressure on the anode side (750 mbar). Higher pressure give rise to better dissociation in the bore while the decrease of the He signal should be due to a faster recombination at higher electron density.

The different behavior of analyte and buffer gas ions can be explained by the charge transfer collisions and ionization processes, too. If the pressure is increasing the collision rate is growing and therefore, more charge can be transferred from helium to the analytes. Hence, the number of helium ions decreases proportionally as the number of analyte ions is increasing.

The influence of the discharge current was examined for atmospheric pressure on the anode side and 0.8 mbar on the cathode side. A significant increase of the ion signals by two orders of magnitude and a slight improvement of the dissociation were observed, if the current was changed, e.g., from 2 to 4 mA. This can be extracted from figure 5.32 that shows the relative signals of all ions measured with CHClF_2 as analyte molecule in He at three different discharge currents.

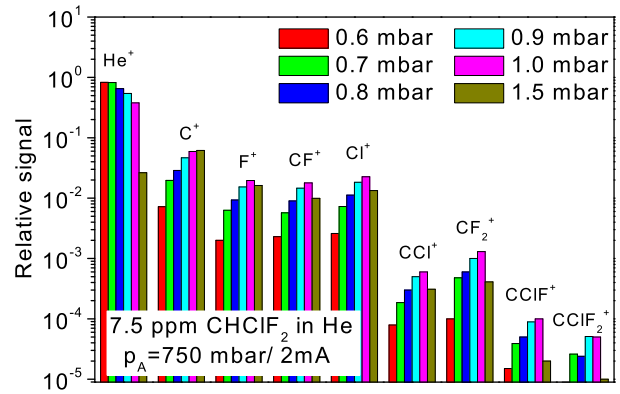


Figure 5.31: Dependence of the ion signals on the cathode side pressure p_c .

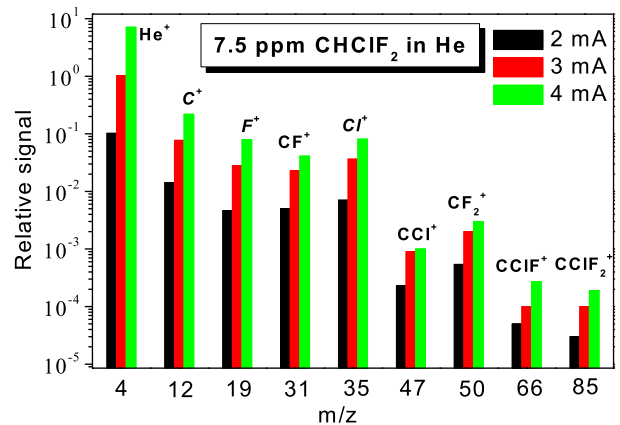


Figure 5.32: Dependence of the ion signals on the discharge current for 7.5 ppm CHClF_2 in He, $p_a = 1000$ mbar / $p_c = 0.8$ mbar.

Analytical results The analysis of molecules such as the halogenated hydrocarbons and their detection limits are of specific interest in environmental science. In the following passage, the analytical performances of the plasma jet coupled to a mass spectrometer will be presented.

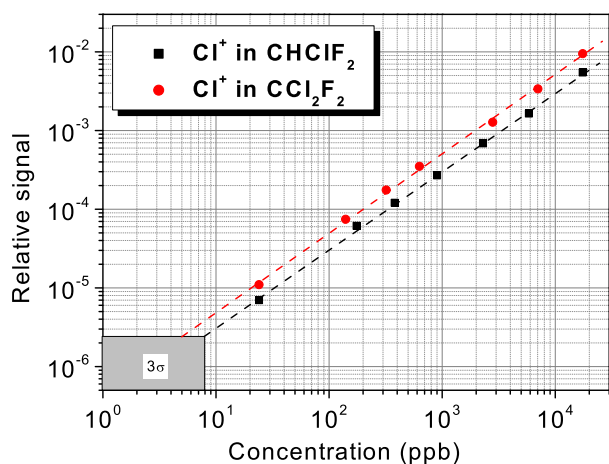


Figure 5.33: Calibration curves for CCl_2F_2 and CHClF_2 detection Cl^+ at $p_a = 800$ mbar / $p_c = 0.6$ mbar, $I = 3$ mA.

First of all, mixtures of freon with the plasma gas were introduced into the instrument and Cl ions were measured. Different freon concentrations were obtained by diluting standard gas mixtures. Calibration curves are presented in figure 5.33 for two freon molecules (CHClF_2 and CCl_2F_2). They are linear over 3 orders of magnitude. The detection limits are 5 and 8 ppb for CCl_2F_2 and CHClF_2 , respectively. These values correspond to about 20 and 32 pg/s. The detection limit for CCl_2F_2 by MHCD-MS can be directly compared with the data

obtained by MHCD-optical emission spectrometry (see section 5.2.2) which was of the same order. From figure 5.33 it can be immediately noticed that the Cl^+ signal ratio of both species is two, which reflects the Cl ratio in the analytes. This is also in accordance with the previous results, applying the MHCD as a source for optical emission spectrometry.

In a second experiment the volatile compounds CCl_4 , CH_2Cl_2 and CHCl_3 were filled separately in glass vials and capped with a Teflon PTFE membrane of 100 μm . These permeation sources were gravimetrically calibrated over a few weeks in order to measure the permeation rate. At room temperature, the flow rates of these hydrocarbons are in the range of a few ng/s (CH_2Cl_2) to hundreds of pg/s (CCl_4 , CHCl_3). The sources were introduced one after the other in the He flow and the mass spectra were recorded. Unfortunately, it was not possible to obtain calibration curves, because no facility to vary their concentration by changing the flow rates of the He gas stream was present. However, the detection limits could be estimated from the signal to noise ratio according to the 3σ criterion.

In figure 5.34 (a – c) the mass spectra of CCl_4 , CH_2Cl_2 and CHCl_3 are shown to give an idea of the Cl^+ signal relative to the decomposition products. Note that the Cl^+ ratio from figure 5.34 is in agreement with the ratio of the mass flow rates taking into account

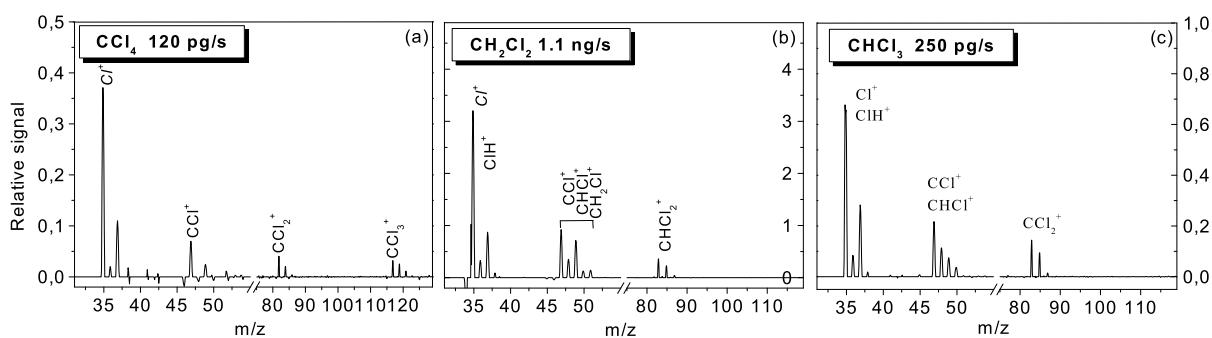


Figure 5.34: Mass spectra of volatile organic compounds (a: CCl_4 , b: CH_2Cl_2 , c: CHCl_3) introduced from a permeation source. Experimental conditions: $p_a = 800 \text{ mbar}$ / $p_c = 0.6 \text{ mbar}$, $I_{pl} = 3 \text{ mA}$.

the Cl masses in all three species and the total masses of the molecules. The detection limit for Cl ions found in this experiment was comparable to the one obtained in the gas mixtures.

In a third experiment the discharge was coupled with a gas chromatograph for the introduction of volatile halogenated molecules. In this case the halogenated molecules were measured by element-selective detection (see section 3). Figure 5.35 displays the chromatographic signals of C^+ , F^+ , Cl^+ , Br^+ , I^+ for the samples given in table 5.4. The concentrations of the different species were in the order of several $\mu\text{l/ml}$. The He^+ signal was independent of time for analyte concentrations lower than several hundred nl/min proving that the plasma was sufficiently robust. Considering its high reactivity, fluorine contaminated the walls of the hole and a background was visible in the measured F^+ signal. Another reason for this background can be the interference with the H_3O^+ ions present at the $m/z = 19$. The detection limits (see figure 5.35) for F^+ , Cl^+ , Br^+ and I^+ were found to be 300 pg/s , 40 pg/s , 150 pg/s and 40 pg/s , respectively. These results are in the same order of magnitude as found without the gas chromatograph. An influence

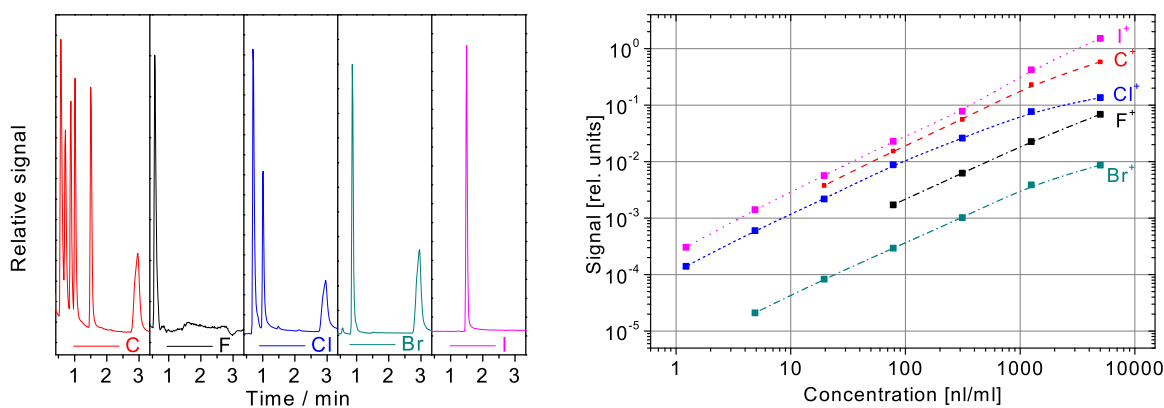


Figure 5.35: Chromatograms of C^+ , F^+ , Cl^+ , Br^+ , I^+ ; sample concentration of $5 \mu\text{l/ml}$ of the analytes, $p_a = 800 \text{ mbar}$ / $p_c = 0.5 \text{ mbar}$, $I_{pl} = 3 \text{ mA}$; Calibration curve.

on the discharge operation was observed when the solvent was entering the plasma as a result of carbon deposition in the bore. This effect was reduced by switching the plasma off in between measurements or by adding oxygen to the plasma gas. It was found that oxygen flow rates lower than 1 ml/min removed the carbon deposition from the walls of the MHCD. This procedure improved the chromatographic resolution but had no influence on the detection limit.

The detection limits obtained are comparable with those found in the DBD and the others listed in section 4.2.2. Additionally, compared with the optical spectrometry, the MHCD-MS detector offers the possibility to determine the stoichiometric structure of molecules by the detection of the fragments.

Conclusions & Outlook

Two miniaturized discharges for quantitative analysis were investigated, the dielectric barrier discharge (DBD) and the micro hollow cathode discharge (MHCD). Both were examined concerning some important plasma parameters, like electron density and gas temperature. For the diagnostics of both discharges, two spectroscopic techniques were improved, based on diode laser atomic absorption spectrometry or emission spectroscopy. In the case of the DBD, a spatial resolution of 50 μm was achieved in order to determine the distribution and density of excited species responsible for dissociation and excitation. This was not studied before and the results obtained are an important contribution to the theory of dielectric barrier discharges. That completes and confirm the theoretical models predicted for the plasma. For the MHCD, a method for determining electron density and gas temperature by line shift measurements was applied. This second method was not successful so far due to the large uncertainties in the experimental data as well as the pressure broadening coefficients. This could be overcome by emission measurements with high spatial resolution; it could be verified whether the proposed line shifts measurements at high-pressure are appropriate for plasma diagnostics.

For the DBD, plasma diagnostics revealed that the hot region of the plasma is constricted close to the temporary cathode for a short time of each discharge cycle. In this thin layer, the electron density reaches 10^{15} cm^{-3} and the gas temperature is about 1000 K, while the rest of the discharge remains cold. The mean power consumption of the discharge is much smaller than 1 W. Nevertheless, the peak power density of 1 kW/cm^3 is in the same order of magnitude as the mean power density of an inductively coupled plasma.

In the case of the MHCD, it could be shown that the gas temperature and electron density at atmospheric pressure in Ar are in the range of 1500 K and $5 \cdot 10^{15} \text{ cm}^{-3}$, respectively. The power density of this discharge is in the order of 1 MW/cm^3 and, therefore, even 3 orders of magnitude higher than in an ICP.

The high power density qualifies both discharges as a powerful tool. Additionally, it was proven that they are also long-living devices. Analytical measurements applying absorption, emission or mass spectrometry manifest the versatility of each discharge for the detection of halogenated hydrocarbons in gaseous and liquid state. Detection limits of several ppb or pg/s were obtained for atomic detection. The stoichiometric ratio of the

elements, present in the investigated substances, was close to the theoretical calculation which allows to determine the molecular structure of the substance. In the case of the coupling of the MHCD with the mass spectrometer, the spectra offer even the possibility of obtaining information on the fragments that were generated.

It was shown that the DBD is an adequate discharge for absorption spectroscopy as the excited state density is quite high and the absorption path relatively long. On the contrary, the MHCD is well adapted for emission spectroscopy. Furthermore, it was observed that mass spectroscopy with a MHCD jet does not reveal lower detection limits than optical spectroscopy. Certainly, the coupling of the discharge to the mass spectrometer has to be improved. However, it is not clear how much the performance is degraded by reducing the pressure on the cathode side in order to form a plasma jet. The electron density is quite low ($< 10^{14} \text{ cm}^{-3}$), as long as it is not measurable with the proposed methods. Additionally, the gas temperature in the bore was determined to a value near room temperature. Such conditions are probably not enough for an efficient dissociation, excitation and ionization of analytes.

A problem of small-scaled discharges is the sample introduction system, because it has to be as small as the discharge itself and the injected sample volume has to be adapted. Several research groups are investigating downscaled sprays and gas chromatographs which have a potential use as sampler for the micro-discharges. Only in combination with these, a powerful detector can be developed. Nevertheless, one has to keep in mind that micro-plasmas can never be all-rounders, but only substitute other analytical instruments in specific areas.

It was discussed that sample introduction of liquid or solid samples into miniaturized discharges is difficult. Therefore, one should also regard a laser induced plasma also as micro-discharge for future analysis. The power densities obtained in LIBS (laser induced breakdown spectroscopy) are much larger than those obtained with electrical discharges. Focusing a ns-pulse of a laser with an energy of some mJ into a volume of 10^{-9} cm^3 , results in power densities of $10^{15} \text{ W/cm}^{-3}$. This is more than sufficient to evaporate any wet aerosol in the sample sprayed by a common nebulizer. Such measurements were already performed [Mar00, MN00] and are under way in our laboratory.

In the next few years, it will become clear whether miniaturized discharges are capable for analytical purposes in series production or not. Some spin-off companies already announced to have market-able products within the next two years. Choosing one of the two discharges investigated, only the MHCD seems to be powerful enough for routine analysis. It could be successfully coupled with a gas chromatograph in order to obtain a

new GC-AED (atomic emission detector). Compared to the standard Agilent device (the only one on the market at this moment), both the discharge as well as the spectrometer should be replaced. The MHCD deals with the advantage of a simple sample introduction, as any material has to pass the hole of the structure and, therefore, the plasma volume. As was shown, efficient excitation took place. Furthermore, the spectrometer used currently offers only a small wavelength range, limiting the analysis to one or a few elements simultaneously. This spectrometer could be replaced by an Echelle spectrometer, as it was developed at ISAS Berlin providing a spectrum of 300 nm for detection of several elements simultaneously. Especially organic compounds consisting of halogen, sulphur and phosphor in addition to C, H and O could be detected.

Furthermore, the MHCD could be coupled with the miniaturized mass spectrometer presented in section 3.4, too. The size and gas flows of both systems are well adapted and with this a complete miniaturized system could be built. A cooperation within this field is envisaged for the near future.

Other potential applications for miniaturized discharges in analytical devices could be the implementation in robotic devices, which will be utilized in situations where man could not be present. If the plasmas are able to work in ambient atmosphere and, additionally, offer good capabilities they could be versatile tools even for missions to other planets.

Appendix

7.1 Coefficients for particle and energy balance

The calculations concerning the particle and energy balance were done with the parameters enlisted in the following tables. All of them are based on a collisional radiative model presented in [Jon98].

Diffusion

The ambipolar diffusion coefficient is given by

$$D_a = \frac{3k_b}{8n_g M \Omega(T_g)} (T_g + T_e) \quad (7.1)$$

with the ion-atom collision integral Ω for argon and helium given by

$$\Omega^{Ar}(T_g) = (3.03 + 6.82 \cdot 10^{-4} T_g - 3.7 \cdot 10^{-8} T_g^2 + 9.15 \cdot 10^{-13} T_g^3) \cdot 10^{-16} [m^3 s^{-1}] \quad (7.2)$$

$$\Omega^{He}(T_g) = (1.72 + 8.26 \cdot 10^{-4} T_g - 5.2 \cdot 10^{-8} T_g^2) \cdot 10^{-16} [m^3 s^{-1}]. \quad (7.3)$$

Ion production

The ionization coefficients can be represented by the following fits

$$S_{CR}^{He} = 3.15 \cdot 10^{-15} \sqrt{T_e} e^{-19.38/T_e} [m^3 s^{-1}] \quad (7.4)$$

$$S_{CR}^{Ar} = 7.34 \cdot 10^{-15} \sqrt{T_e} e^{-12.06/T_e} [m^3 s^{-1}], \quad (7.5)$$

in which T_e is the electron temperature in eV.

$n_e \text{ m}^{-3}$	a_0	a_1	a_2	a_3	a_4
10^{19}	-16.004	-4.115	-2.043	3.023	-0.851
10^{20}	-11.443	-23.219	23.278	-11.401	2.170
10^{21}	-10.996	-23.431	24.004	-11.891	2.280
10^{22}	-10.096	-23.369	23.992	-11.896	2.282

Table 7.1: Fit coefficients a_i for recombination term α_{CR} for different n_e values

Recombination

The recombination coefficient α_{CR} is implemented using a fourth order polynomial expression:

$$\alpha_{CR} = 10^{F(T_e)} \sum_{l=0}^4 a_l T_e^l, \quad (7.6)$$

using the coefficients given in table 7.1.

7.2 Coefficients for pressure broadening

Line width and shift for pressure broadened lines are given by $2\gamma N$ and βN , respectively. While N is the gas density according to the ideal gas law, the coefficients 2γ and β are given in table 7.2 for different authors. The values for the transitions starting on metastable states (801 and 811 nm) have to be scaled according to the Lindholm-Foley theory with $T^{0.3}$. The value for the line starting from a resonance level (800 nm) has to be scaled with a slightly smaller exponent, because the temperature independent resonant broadening also partakes.

The parameters in the table are given in the original unit measured by the authors and transformed to the consistent unit of pm/cm³.

width	800 nm	801 nm	811 nm	unit	T [K]
Moussounda [Mou87]		6.71 ± 0.26 22.9	7.44 ± 0.45 26.0	10 ⁻⁹ rad/s cm ³ 10 ⁻¹⁹ pm/cm ³	2250
Aeschliman [Aes76]	2.27 ± 0.25 22.7			10 ⁻²⁰ Å/cm ³ 10 ⁻¹⁹ pm/cm ³	300
Copley [Cop76b]	4.1 ± 0.2 26.2	2.9 ± 0.3 18.6		10 ⁻²⁰ cm ⁻¹ /cm ³ 10 ⁻¹⁹ pm/cm ³	1130
Vallee [Val77]		2.8 ± 0.3 18.0	2.9 ± 0.3 19.1	10 ⁻²⁰ cm ⁻¹ /cm ³ 10 ⁻¹⁹ pm/cm ³	3900
Tachibana [Tac82]			1.42 ± 0.14 9.3	10 ⁻²⁰ cm ⁻¹ /cm ³ 10 ⁻¹⁹ pm/cm ³	300
Lee [Lee75]			1.9 ± 0.2 12.5	10 ⁻²⁰ cm ⁻¹ /cm ³ 10 ⁻¹⁹ pm/cm ³	300
shift	800 nm	801 nm	811 nm	unit	T [K]
Moussounda [Mou87]	2.24 ± 0.15 7.5	3.00 ± 0.17 10.2	2.88 ± 0.17 10.1	10 ⁻⁹ rad/s cm ³ 10 ⁻¹⁹ pm/cm ³	2250
Aeschliman [Aes76]	2.37 ± 0.12 2.37	5.11 ± 0.25 5.11	4.73 ± 0.25 4.73	10 ⁻²¹ Å/cm ³ 10 ⁻¹⁹ pm/cm ³	300
Copley [Cop76b]		1.51 ± 0.07 9.7	1.22 ± 0.07 8.0	10 ⁻²⁰ cm ⁻¹ /cm ³ 10 ⁻¹⁹ pm/cm ³	1130
Vallee [Val77]		9.6 ± 0.5 5.5	8.5 ± 0.5 6.3	10 ⁻²¹ cm ⁻¹ /cm ³ 10 ⁻¹⁹ pm/cm ³	3900
Tachibana [Tac82]			4.4 ± 0.4 2.9	10 ⁻²¹ cm ⁻¹ /cm ³ 10 ⁻¹⁹ pm/cm ³	300

Table 7.2: Width and shift coefficient for different Ar transitions.

Bibliography

- [Aes76] D. Aeschliman, R. Hill, and D. Evans, *Collisional broadening and shift of neutral argon spectral lines*, Phys. Rev. A **14**, (1976) 1421 – 1427.
- [Agi] Agilent, *Lab-on-a-chip technology*, <http://www.chem.agilent.com/scripts/generic.asp?lpage=534&indcol=Y&prodcol=Y>.
- [Bad00] E. Badman and R. Cooks, *Miniature mass analyzers*, J. Mass Spectrom. **35**, (2000) 659 – 671.
- [Bal] Balzers, *Manual for Quadrupole mass spectrometer system QMG 422*.
- [Bas01] A. Bass, C. Chevalier, and M. Blades, *A capacitively coupled microplasma (CCmP) formed in a channel in a quartz wafer*, J. Anal. At. Spectrom. **16**, (2001) 919 – 921.
- [Ber76] M. Berthelot, Compt. Rend. Acad. Sce. **82**, (1876) 1360.
- [Bes02] F. Bessoth, O. Naji, J. Eijkel, and A. Manz, *Towards an on-chip gas chromatograph: the development of a gas injector and a dc plasma emission detector*, J. Anal. At. Spectrom. **17**, (2002) 794 – 799.
- [Bil00] A. Bilgic, E. Voges, U. Engel, and J. Broekaert, *A low-power 2.45 GHz microwave induced helium plasma source at atmospheric pressure based on microstrip technology*, J. Anal. At. Spectrom. **15**, (2000) 579 – 580.
- [BR97] H. Becker-Ross and S. Florek, *Echelle spectrometers and charge-coupled devices*, Spectrochimica Acta Part B **52**, (1997) 1367 – 1375.
- [Bre98] C. Brede, S. Pedersen-Bjergaard, E. Lundanes, and T. Greibrokk, *Microplasma Mass Spectrometric Detection in Capillary Gas Chromatography*, Anal. Chem. **70**, (1998) 513 – 518.

- [Bro02] J. Broekaert, *The development of microplasmas for spectrochemical analysis*, Anal. Bioanal. Chem **374**, (2002) 182 – 187.
- [Cal] Caliper, http://www.calipertech.com/products/labchip_systems.shtml.
- [Cop76a] G. Copley, *A comparison of foreign gas broadening and shift of neon and argon emission lines*, J. Quant. Spectrosc. Radiat. Transfer **16**, (1976) 377–384.
- [Cop76b] G. Copley, *A comparison of self broadening and shift of helium, neon and argon emission lines*, J. Quant. Spectrosc. Radiat. Transfer **16**, (1976) 553–558.
- [Cse93] T. Cserfalvi, P. Mezei, and P. Apai, *Emission studies on a glow discharge in atmospheric pressure air using water as a cathode*, J. Phys. D **26**, (1993) 2184 – 2188.
- [Dal77] J. van Dalen, P. de Lezenne Coulander, and L. de Galas, *Optimization of microwave-induced plasma as an element-selective detector for non-metals*, Anal. Chim. Acta **94**, (1977) 1–19.
- [Dav01] W. Davis and R. Marcus, *An atmospheric pressure glow discharge optical emission source for the direct sampling of liquid media*, J. Anal. At. Spectrom. **16**, (2001) 931 – 937.
- [Dra66] G. Drake, *Atomic, Molecular and Optical Physics Handbook*, 698, AID Press, Woodbury, NY (1966).
- [Dua03] Y. Duan, Y. Su, and Z. Jin, *Capillary-discharge-based portable detector for chemical vapor monitoring*, Rev. Sci. Instr. **74**(5), (2003) 2811 – 2816.
- [Eij99] J. Eijkel, H. Stoeri, and A. Manz, *A Molecular Emission Detector on a Chip Employing a Direct Current Microplasma*, Analytical Chemistry **71**(14), (1999) 2600–2606.
- [Eij00] J. Eijkel, H. Stoeri, and A. Manz, *A dc Microplasma on a Chip Employed as an Optical Emission Detector for Gas Chromatography*, Analytical Chemistry **72**(11), (2000) 2547–2552.
- [Eng75] A. von Engel, *Ionized gases*, Oxford University Press (1975).
- [Eng00] U. Engel, A. Bilgic, O. Haase, E. Voges, and J. Broekaert, *A Microwave-Induced Plasma Based on Microstrip Technology and Its Use for the Atomic Emission*

- Spectrometric Determination of Mercury with the Aid of the Cold-Vapor Technique*, Anal. Chem **72**, (2000) 193 – 197.
- [Fra60] G. Francis, *Ionization phenomena in gases*, Butterworths scientific publications (1960).
- [Fra93] J. Franzke, A. Schnell, and K. Niemax, *Spectroscopic properties of commercial laser diodes*, Spectrochimica Acta Rev. **15**(5), (1993) 379–395.
- [Fra03] J. Franzke, K. Kunze, M. Miclea, and K. Niemax, *Microplasmas for analytical spectrometry*, J. Anal. At. Spectrom. **18**, (2003) 802 – 807.
- [Ghe00] N. Gherardi, G. Gouda, E. Gat, A. Ricard, and F. Massines, *Transition from glow silent discharge to micro-discharges in nitrogen gas*, Plasma Sources Sci. Technol. **9**, (2000) 340 – 346.
- [Gri64] H. Griem, *Plasma Spectroscopy*, McGraw-Hill, New York (1964).
- [Gro93] H. Groll and K. Niemax, *Multielement diode laser atomic absorption spectrometry in graphite tube furnaces and analytical flames*, Spectrochimica Acta **48 B**(5), (1993) 633–641.
- [Guc03] R. Guchardi and P. Hauser, *A capacitively coupled microplasma in a fused silica capillary*, J. Anal. At. Spectrom. **18**, (2003) 1056–1059.
- [Guc04a] R. Guchardi and P. Hauser, *Capacitively coupled microplasma for on-column detection of chromatographically separated inorganic gases by optical emission spectrometry*, J. of Chrom. A **1033**, (2004) 333 – 338.
- [Guc04b] R. Guchardi and P. Hauser, *Determination of organic compounds of gas chromatography using a ne capacitively coupled microplasma detector*, The Analyst **129**, (2004) Advance Article.
- [Hoh02] O. Hohn, *Hochdruckmikroentladungen mit hohem Gasfluss, Eine Quelle zur Erzeugung von Ionen und spinpolarisierten metatablienen Atomen.*, Dissertation, Johann Wolfgang Goethe Universität in Frankfurt/Main (2002).
- [Hol51] T. Holstein, *Imprisonment of Resonance Radiation in Gases. II*, Phys. Rev. **83**, (1951) 1159–1168.
- [Hop00] J. Hopwood, *A microfabricated inductively coupled plasma generator*, J. Microelectromechanical Systems **9**, (2000) 309 – 313.

- [Hsu03] D. Hsu and D. Graves, *Microhollow cathode discharge stability with flow and reaction*, J. Phys. D: Appl. Phys. **36**, (2003) 2898 – 2970.
- [Ich03] T. Ichiki, T. Koidesawa, and Y. Horiike, *An atmospheric-pressure microplasma jet source for the optical emission spectroscopic analysis of liquid sample*, Plasma Sources Sci. Technol. **12**, (2003) S16 – S20.
- [Iza02] F. Iza and J. Hopwood, *Influence of operating frequency and coupling coefficient on the efficiency of microfabricated inductively coupled plasma sources*, Plasma Science and Technology **11**, (2002) 229 – 235.
- [Jen02] G. Jenkins and A. Manz, *A miniaturized glow discharge applied for optical emission detection in aqueous analytes*, J. Micromech. Microeng. **12**, (2002) N19 – N22.
- [Jin01] Z. Jin, Y. Su, and Y. Duan, *A Low-Power, Atmospheric Pressure, Pulsed Plasma Source for Molecular Emission Spectrometry*, Anal. Chem. **73**, (2001) 360 – 365.
- [Jon98] J. Jonkers, *Excitation and Transport in small scaled plasmas*, Dissertation, Technical university of Eindhoven (1998).
- [Kam04] G. Kamlage, *private communications* (2004).
- [Koc98] J. Koch, A. Zybin, and K. Niemax, *Element-selective trace detection of toxic species in environmental samples using chromatographic techniques and derivative diode laser absorption spectrometry*, Appl. Phys. B. **67** 475 – 479.
- [Koc02] J. Koch, A. Zybin, and K. Niemax, *Narrow and broad band diode laser absorption spectrometry - concepts, limitations and applications*, Spectrochim. Acta Part B **57**, (2002) 1547 – 1561.
- [Koc04] J. Koch, M. Okruss, J. Franzke, S. Florek, K. Niemax, and H. Becker-Roß, *Element-selective detection of gas chromatographic eluates by near infrared Échelle optical emission spectrometry on microwave-induced plasmas*, Spectrochimica Acta A **59**, (2004) 199 – 207.
- [Kog03] U. Kogelschatz, *Dielectric-barrier Discharges: Their History, Discharge Physics, and Industrial Applications*, Plasma Chemistry and Plasma Processing **23**(1), (2003) 1–46.

- [Kon01] A. Kono, T. Sugiyama, T. Goto, H. Furuhashi, and Y. Uchida, *Production of cw high-density non-equilibrium plasma in the atmosphere using microgap discharge excited by microwave*, Jpn. J. Appl. Phys. **40**, (2001) L238 – L241.
- [Kot03] P. Kothnur and L. Raja, *Two dimensional simulation of the structure of direct-current microdischarges*, in *56th Gaseous Electronics Conference* (2003).
- [Kun01] K. Kunze, *Ein Plasma für die Miniaturisierung von Analysensystemen - Die dielektrisch behinderte Entladung*, Diplomarbeit, University of Dortmund (2001).
- [Kun02] K. Kunze, M. Miclea, G. Musa, J. Franzke, C. Vadla, and K. Niemax, *Diode laser-aided diagnostics of a low-pressure dielectric barrier discharge applied in element-selective detection of molecular species*, Spectrochim. Acta Part B **57**, (2002) 137 – 146.
- [Kun03] K. Kunze, M. Miclea, J. Franzke, and K. Niemax, *The dielectric barrier discharge as a detector for gas chromatography*, Spectrochimica Acta Part B **58**, (2003) 1435 – 1443.
- [Kur96] R. Kurucz, P. Smith, C. Heise, and J. Esmond, *Atomic Spectral Line Database from CD-Rom 23 of R.L. Kurucz*, <http://cfa-www.harvard.edu/amdata/ampdata/kurucz23/sekur.html> (1996).
- [Kur03] P. Kurunzci, *Radiative and Collisional Processes in a High-Pressure Micro-Hollow Cathode Discharge*, Dissertation, Stevens Institute of Technology (2003).
- [Lee75] C. Lee, D. Camm, and G. Copley, *Van der Waals broadening of argon absorption lines*, J. Quant. Spectrosc. Radiat. Transfer **15**, (1975) 211 – 216.
- [Lei88] K. Leiter, P. Scheier, G. Walder, and T. D. Märk, *Determination of absolute partial and total electron impact ionization cross-sections for CF₂Cl₂ from threshold up to 180 eV: an improved experimental method*, Int. J. Mass Spectrom. Ion Proc. **87**, (1988) 209 – 224.
- [Lei00] F. Leipold, R. Stark, A. El-Habachi, and K. Schoenbach, *Electron density measurements in an atmospheric pressure air plasma by means of infrared heterodyne interferometry*, J. Phys. D: Appl. Phys. **33**, (2000) 2268 – 2273.
- [LH68] W. Lochte-Holtgreven, *Plasma Diagnostics*, North-Holland publishing company, Amsterdam (1968).

- [Lig97] V. Liger, A. Zybin, Y. Kuritsyn, and K. Niemax, *Diode-laser atomic-absorption spectrometry by the double-beam-double-modulation technique*, *Spectrochimica Acta Part B* **52**, (1997) 1125–1138.
- [Lon03] R. Longwitz, H. van Lintel, and P. Renaud, *Study of micro-glow discharges as ion sources for ion mobility spectrometry*, *J. Vac. Sci. Technol. B* **21**(4), (2003) 1570 – 1573.
- [Man90] A. Manz, N. Graber, and H. Widmer, *Miniaturized total chemical analysis systems: a novel concept for chemical sensing*, *Sens. Actuators B* **1**, (1990) 244–248.
- [Mar48] H. Margenau, *Theory of high frequency gas discharges. IV. Note on the similarity principle*, *Phys. Rev.* **73**(4), (1948) 326 – 328.
- [Mar00] M. Martin and M. Cheng, *Detection of chromium aerosol using time-resolved laser-induced plasma spectroscopy*, *Appl. Spec.* **54**(9), (2000) 1279 – 1285.
- [Mar01] R. Marcus and W. Davis, *An atmospheric pressure glow discharge optical emission source for the direct sampling of liquid media*, *Anal. Chem.* **73**, (2001) 2903 – 2910.
- [McD64] E. W. McDaniel, *Collison Phenomena in Ionized Gases*, John Wiley & Sons, New York (1964).
- [Mic01] M. Miclea, K. Kunze, G. Musa, J. Franzke, and K. Niemax, *The dielectric barrier discharge - a powerful microchip plasma for diode laser spectrometry*, *Spectrochim. Acta Part B* **56**, (2001) 37–43.
- [Mic02] M. Miclea, K. Kunze, J. Franzke, and K. Niemax, *Plasmas for lab-on-the-chip applications*, *Spectrochim. Acta Part B* **57**, (2002) 1585–1592.
- [Mic04] M. Miclea, K. Kunze, J. Franzke, and K. Niemax, *Microplasma jet mass spectrometry of halogenated organic compounds*, submitted to *J. Anal. At. Spectrom.* (2004).
- [Mij95] Z. Mijatovic, N. Konjevic, M. Ivkovic, and R. Kobilarov, *Influence of ion dynamics on the width and shift of isolated He I lines in plasmas. II*, *Phys. Rev. E* **51**(5), (1995) 4891 – 4896.
- [Mil88] D. R. Miller, *Free jet sources*, chapter 2, 14 – 53, Oxford University Press (1988).

- [Min02] O. Minayeva and J. Hopwood, *Emission spectroscopy using a microfabricated inductively coupled plasma-on-a-chip*, J. Anal. At. Spectrom. **17**, (2002) 1103–1107.
- [MN00] M. Hidalgo-Nunez, P. Cavalli, G. Petrucci, and N. Omenetto, *Analysis of sulfuric acid aerosols by laser-induced breakdown spectroscopy and laser-induced photofragmentation*, Appl. Spec. **54**(12), (2000) 1805 – 1816.
- [Mon] A. Montaser and D. Golightly, *Inductively coupled plasmas in analytical atomic spectrometry*, VCH Publishers **1992**.
- [Mos03] M. Moselhy, I. Petzenhauser, K. Frank, and K. Schoenbach, *Excimer emission from microhollow cathode argon discharges*, J. Phys. D.: Appl. Phys. **36**, (2003) 2922 – 2927.
- [Mou87] P. Moussounda and R. P., *Pressure broadening of argon lines emitted by high-pressure microwave discharge (Surfatron)*, J. Phys. B: At. Mol. Phys. **20**, (1987) 946–961.
- [NISov] NIST, *Chemistry WebBook* (<http://webbook.nist.gov/>).
- [Ole89] J. Olesik, L. Smith, and E. Williamsen, *Signal fluctuations due to individual droplets in inductively coupled plasma atomic emission spectrometry*, Anal. Chem **61**, (1989) 2002 – 2008.
- [Pas89] Paschen, Ann. Phys. Chem. **37**, (1889) 69.
- [PB93] S. Pedersen-Bjergaard and T. Greibrokk, *On-column bromine- and chlorine-selected detection for capillary gas chromatography using a radio frequency plasma*, Anal. Chem. **65**, (1993) 1998 – 2002.
- [PB94] S. Pedersen-Bjergaard and T. Greibrokk, J. Microcolumn. Sep. **6**, (1994) 11.
- [PB96] S. Pedersen-Bjergaard and T. Greibrokk, *Effect of make-up gas in on-column atomic emission spectrometric detection for capillary gas chromatography*, J. Anal. At. Spectrom. **11**, (1996) 117 – 121.
- [Pen01] C. Penache, S. Datta, S. Mukhopadhyay, A. Bräuning-Demian, P. Joshi, O. Hohn, S. Schössler, T. Jahnke, and H. Schmidt-Böcking, *Large area surface modification induced by parallel operated MSE sustained glow discharges*, in *Proceedings of Hakone, Estonia* (2001).

- [Pen02] C. Penache, *Study of High-Pressure Glow Discharges Generated by Micro-Structured Electrode (MSE) Arrays*, Dissertation, Johann Wolfgang Goethe - Universität, Frankfurt (2002).
- [Qui96] B. Quimby, P. Larson, and P. Dryden, *A comparison of the HP G2350A AED vs. HP 5921A AED for average values of MDL and selectivity for selected elements*, Hewlett Packard Application Note 228–363.
- [Rai97] Y. P. Raizer, *Gas discharge physics*, Springer (1997).
- [Rei78] J. Reid, J. Shewchun, B. Garside, and E. Ballik, *High sensitivity pollution detection employing tunable diode lasers*, Appl. Opt. **17**, (1978) 300 – 307.
- [Sch00] K. Schoenbach, A. El-Habachi, M. Moselhy, W. Shi, and R. Stark, *Microhollow cathode discharge excimer lamps*, Physics of Plasmas **7**, (2000) 2186 – 2191.
- [Sch03] S. Schermer, N. Bings, A. Bilgic, R. Stonies, E. Voges, and J. Broekaert, *An improved microstrip plasma for optical emission spectrometry of gaseous species*, Spectrochimica Acta Part B **52**, (2003) 1585 – 1596.
- [Sie57] W. Siemens, *Ueber die elektrostatische Induction und die Verzögerung des Stroms in Flaschendrahten*, Poggendorffs Ann. Phys. Chem **102**, (1857) 66 – 122.
- [Sie98] P. Siebert, G. Petzold, A. Hellenbart, and J. Müller, *Surface microstructure/miniature mass spectrometer: processing and applications*, Appl. Phys. A, **67**, (1998) 155 – 160.
- [Sie03] Siemens, *Archive - Personalities: Werner von Siemens (1816-1892)*, http://w4.siemens.de/archiv/en/persoenlichkeiten/werner_von_siemens.html (2003).
- [Stu64] D. Sturges and H. Oskam, *Studies of the properties of the hollow cathode glow discharge in helium and neon*, J. Appl. Phys. **35**(10), (1964) 2887 – 2894.
- [SW75] N. Small-Waren and C. Lue-Yung, *Lifetime of the metastable 3P_2 and 3P_0 states of rare-gas atoms*, Phys. Rev. A **11**, (1975) 1777–1783.
- [Tac82] K. Tachibana, H. Harima, and Y. Urano, *Measurements of collisional broadening and the shift of argon spectral lines using a tunable diode laser*, J. Phys. B: At. Mol. Phys. **15**, (1982) 3169–3178.

- [Tan03] K. Taniguchi, T. Fukasawa, H. Yoshiki, and Y. Horiike, *Generation of integrated atmospheric-pressure microplasmas*, Jpn. J. Appl. Phys. **42**(10), (2003) 6584 – 6589.
- [Ter79] S. Terry, J. Jerman, and J. Angell, IEEE Trans. on Electron. Dev. **26**, (1979) 1880.
- [Uns68] A. Unsöld, *Physik der Sternatmosphären*, Springer Verlag, Berlin (1968).
- [Vad00] C. Vadla, M. Movre, R. Beuc, J. Franzke, H.-D. Wizemann, and K. Niemax, *Optimization of lead metastable production in a low pressure argon discharge*, Spectrochim. Acta Part B **55**, (2000) 1759–1769.
- [Val77] O. Vallee, P. Ranson, and J. Chapelle, *Measurements of broadening of argon lines and oscillator strengths of resonance lines*, J. Quant. Spectrosc. Radiat. Transfer **18**, (1977) 327 – 347.
- [Wat01] N. Watanabe, W. Buscher, and G. Böhm, *Atmospheric Pressure Barrier Discharge Helium Plasma for Halogen Determination with Optical Emission*, Analytical Science **17**, (2001) i971 – i973.
- [Whi59] A. White, *New hollow cathode glow discharge*, J. Appl. Phys. **30**(5), (1959) 711 – 719.
- [Wil02] C. Wilson and Y. Gianchandani, *Spectral detection of metal contaminants in water using an on-chip microglow discharge*, IEEE Transactions on electron devices **49**(12), (2002) 2317 – 2322.
- [Yin99] Y. Yin, J. Messier, and J. Hopwood, *Miniaturized inductively coupled plasma sources*, IEEE Transactions on Plasma Science **27**, (1999) 1516 – 1524.
- [Yos01] H. Yoshiki and Y. Horiike, *Capacitively coupled microplasma source on a chip at atmospheric pressure*, Jpn. J. Appl. Phys. **40**, (2001) L360–L362.
- [Zyb95] A. Zybin, C. Schnürer-Patschan, and K. Niemax, *Wavelength modulation diode laser atomic absorption spectrometry in modulated low-pressure Helium plasmas for element-selective detection in gas chromatography*, Journal of Analytical atomic Spectrometry **10**, (1995) 563–567.

- [Zyb97] A. Zybin and K. Niemax, *Improvement of the wavelength tunability of etalon-type laser diodes and mode recognition and stabilization in diode laser spectrometers*, Spectrochim. Acta Part B **52**, (1997) 1215 – 1221.

So far, the present work has resulted in several conference contributions and the following publications:

1. K. Kunze *Ein Plasma für die Miniaturisierung von Analysensystemen - Die dielektrisch behinderte Entladung* Diplomarbeit / Universität Dortmund (2001) – [Kun01]
2. M. Miclea, K. Kunze, G. Musa, J. Franzke, K. Niemax. *The dielectric barrier discharge - a powerful microchip plasma for diode laser spectrometry* Spectrochimica Acta, Part B 56 (2001) 37–43 – [Mic01]
3. M. Miclea, K. Kunze, J. Franzke, C. Vadla, K. Niemax. *Spatial and temporal distribution of excited Cl atoms in a linear dielectric barrier discharge* submitted to Romanian Reports in Physics (2001)
4. K. Kunze, M. Miclea, G. Musa, J. Franzke, C. Vadla, K. Niemax. *Diode-laser aided diagnostics of a low-pressure dielectric barrier discharge applied in element selective detection of molecular species* Spectrochimica Acta, Part B 57 (2002) 137–146 – [Kun02]
5. M. Miclea, K. Kunze, J. Franzke, K. Niemax *Plasmas for lab-on-the-chip applications* Spectrochimica Acta, Part B 57 (2002) 1585–1592 – [Mic02]
6. J. Franzke, K. Kunze, M. Miclea, K. Niemax *Technologie von Plasmabildschirmen und CD-Spielern: Optimiert für den Einsatz in analytischen Systemen* Nachrichten aus der Chemie 50 (2002) 1247–1249
7. J. Franzke, K. Kunze, M. Miclea, K. Niemax *Microplasmas for analytical spectrometry* J. Anal. At. Spectrom. 18 (2003) 802–807 – [Fra03]
8. K. Kunze, M. Miclea, J. Franzke, K. Niemax *The dielectric barrier discharge as a detector for gas chromatography* Spectrochimica Acta, Part B 58 (2003) 1435–1443 – [Kun03]
9. K. Kunze, A. Zybin, J. Koch, J. Franzke, M. Miclea, K. Niemax *Element selective detection of molecular species applying chromatographic techniques and diode laser atomic absorption spectrometry* in print in Spectrochimica Acta, Part A (2004)
10. M. Miclea, K. Kunze, J. Franzke, K. Niemax *Microplasma jet mass spectrometry of halogenated organic compounds* accepted for publication in J. Anal. At. Spectrom. (2004)

Acknowledgments

Last but not least I'd like to thank all people who made this thesis possible. The present work was performed at the former *Institute of Spectrochemistry and Applied Spectroscopy* (now *Institute for Analytical Sciences*) in Dortmund and was partially funded by the Deutsche Forschungsgemeinschaft.

To my supervisor, Prof. Dr. Niemax, I am thankful for many suggestions and fruitful discussions, especially during the writing of my thesis.

My very special thanks are addressed to Prof. Dr. Bayer for spontaneously accepting to review my work.

I'm much obliged to Dr. Miclea. Without her help, mental and scientific support this thesis wouldn't have been possible. Thanks for the last 4.5 years. Let's hope we will meet again in the future doing some strange experiments.

Many thanks are directed to PD Dr. Franzke for his continuous support and friendliness during my time at ISAS. His suggestions after proofreading my thesis were very helpful.

The preliminary measurements of the MHCD-MS coupling were done at IKF in Frankfurt. Sincere thanks to Dipl.-Phys. S. Schössler. Without his help the coupling wouldn't have worked. Furthermore, I'd like to thank Prof. Dr. Musa and Prof. Dr. Schmidt-Böcking for the provision of the dielectric barrier plates and the first MHCD structures, respectively.

I'd like to thank Dr. Vadla for fruitful discussions, experimental help and the support by the evaluation of line profiles.

The echelle spectrometer was provided by the colleagues of our partner institute in Berlin. Many thanks to Dr. Becker-Roß, Dr. Florek, Dr. Heitmann and M. Okruss. They also construct a high-resolution spectrometer; unfortunately, these measurements couldn't be

incorporated anymore in the thesis. Nevertheless, thanks for the great time at ISAS Berlin.

Without the help of the electrical and mechanical workshop, who developed and built some devices, the work wouldn't have been possible, thank you.

I gratefully acknowledge the help of Dr. Victor Bocos for preparation and calibration of the permeation sources.

Many thanks to all members of the former group 313 and the current group miniaturization at ISAS for a lot of discussions, fun etc. Through their mentoring, I have learned most of the laboratory techniques essential for my present and future scientific endeavors. With the help of their example and patient guidance, I have grown personally in such a way that I will have graduated from ISAS with far more than a PhD. Special thanks go to M. Eickmeyer for the literature review each morning and the many cheerful discussions. For continuous technical help I'd like to thank N. Ahlmann. I'm grateful to O. Vogt for constant discussions and motivation during our collective writing time.

Special thanks are directed to all the persons who proofread my thesis; apart from the people mentioned above, I'd like to thank G. Jenkins, Dr. Margetic, B. Freitag, T. Spernat and W. Wegner.

I'm indebted to my parents for constantly pointing out that scientists are only paid for playing and for giving me the great opportunity to do so.

Curriculum vitae

Personal data

name Kerstin Helge Kunze

date/place of birth 27.07.1976 / Hagen

Education

2001 to 2004 PhD, Institute for Analytical Sciences, University of Dortmund

2003 Participant of the “International school of quantum electronics” (38th Course, Theoretical-practical course on spectroscopic techniques for materials, environment and cultural heritage), Erice/Italy

2001 Participant of the 260th Hereaus-Seminar, “Course on low temperature plasma physics 6”, Bad Honnef/Germany

2001 Diploma thesis: “A discharge for the miniaturization of analytical systems - The dielectric barrier discharge” (performed at the Institute for Spectrochemistry and Applied Spectroscopy, Dortmund)

1999 to 2000 courses of “economics for scientists”, University of Hagen

1995 to 2001 Department of physics, University of Dortmund